UNIVERSITY OF OKLAHOMA

GRADUATE COLLEGE

# INVESTIGATION OF FLOW THROUGH COMPLICATED MICROFLUIDIC DEVICES AND OVER MICROPATTERNED SURFACES USING COMPUTATIONAL FLUID DYNAMICS

A DISSERTATION

SUBMITTED TO THE GRADUATE FACULTY

in partial fulfillment of the requirements for the

Degree of

DOCTOR OF PHILOSOPHY

By

MARGARET L. HECK
Norman, Oklahoma
2015

INVESTIGATION OF FLOW THROUGH COMPLICATED MICROFLUIDIC DEVICES AND OVER MICROPATTERNED SURFACES USING COMPUTATIONAL FLUID DYNAMICS

A DISSERTATION APPROVED FOR THE
SCHOOL OF CHEMICAL, BIOLOGICAL AND MATERIALS ENGINEERING

BY

_____
Dr. Dimitrios V. Papavassiliou, Chair

_____
Dr. Prakash Vedula

_____
Dr. Lance Lobban

_____
Dr. Edgar O'Rear

_____
Dr. David Schmidtke

## Acknowledgements

Because I studied at the undergraduate and graduate levels at the University of Oklahoma, I had the unique honor of being “raised” by my professors.

Each of my committee members has had a pivotal influence on my engineering perspective and has contributed to my academic success to an extent that cannot be adequately expressed in words.

Without the teaching and guidance of Drs. Papavassiliou, Lobban, O’Rear, Schmidtke, and Vedula, I would not have been able to complete the research outlined in this dissertation. I thank these professors, as well as all of those at the University of Oklahoma from whom I have learned so much, for showing me how to think like a true engineer.

The person to whom almost all credit for my current and future success should be given, however, is Dr. Papavassiliou. The eight years we worked together have taught me far more than I ever expected and have opened many invaluable doors of opportunity for me. Dr. Papavassiliou’s kindness and patience, as well as his expertise and wisdom, throughout this journey has had a profound impact on me. I cannot express my gratitude for all he has taught and shown me.

I will always be honored to be associated with such an inspiring and intelligent group of mentors. Thank you all for your trust and belief in me.

# Table of Contents

# List of Tables

## Chapter 1: Introduction and Background



## Chapter 2: Superhydrophobic Micro-Roughness Models



## Chapter 3: Non-Newtonian Flow Models over Mixed Boundaries



## Chapter 5: Flow and Damage Models in a Centrifugal Pump

# List of Figures

## Chapter 1: Introduction and Background



## Chapter 2: Superhydrophobic Micro-Roughness Models

**Chapter 3: Non-Newtonian Flow Models over Mixed Boundaries**

## Chapter 4: *A Priori* Models for Effective Slip



## Chapter 5: Flow and Damage Models in a Centrifugal Pump

## Abstract

Computational fluid dynamics is used to study two distinct areas of engineering interest: microfluidic systems involving superhydrophobic surfaces and blood pumps. Superhydrophobic surfaces, which can induce slip at fluid-solid interfaces, are modeled using mixed free-shear and no-slip boundary conditions. Despite remarkable effort to include the effects of surface topology and various flow and physical properties in models describing fluid slip over these surfaces, the mathematical description of flow over mixed slip boundaries is still incomplete. Critical configurations of roughness necessary to achieve drag reduction in micro-channels are established. The effects of roughness shape and size on drag for both Newtonian and non-Newtonian fluid flow are also considered in depth. Based on these findings, similarity theory is used to develop a model to describe drag reduction as a function of channel geometry. The principles used in the development of these models are then applied to the more complicated system of a centrifugal blood pump. The effects of the non-Newtonian rheological behavior, hematocrit, temperature, and turbulence on pump performance and subsequent blood damage is quantified over a wide range of operating conditions.

# Chapter 1: Introduction and Background

The invention of the modern computer has transformed the entire discipline of engineering. In particular, fluid dynamics, which often involves the study of flow described by large systems of partial differential equations, has benefited greatly from the technological developments of the last century. Mathematical problems that would have once taken scientists months or even years to answer may now be solved in a matter of minutes, thanks to these remarkable advances in computing science. As the processing power of computers increases exponentially and the cost associated with computational resources continues to decrease, a new area of engineering called computational fluid dynamics (CFD) has emerged to supplement and complement the developments of theoretical analysis and experimentation (Tu, Heng Yeoh, and Liu, 2012).

## 1.1. Scope of Study

1) To facilitate the advancement of CFD in the study of transport phenomena, numerical simulations are used in this study to characterize flow in micro-channels with superhydrophobic walls in plane-Couette and pressure-driven flow.
2) To demonstrate the power of CFD in the development of new mathematical relationships to describe flow, the numerical predictions obtained are used to develop models to estimate slip velocity and drag reduction *a priori*.

3) To advance the use of CFD in the development and optimization of biomedical devices, flow through a centrifugal blood pump is modeled and presented for future validation with experimental results.

## 1.2. Computational Fluid Dynamics

CFD takes advantage of the fact that any physical system is governed by mass conservation, energy conservation, and Newton's second law. Rather than solving these equations analytically, however, this computational approach replaces the partial differential equations with numbers and then advances the values throughout space and time (Anderson et al., 2009). While computational fluid dynamics does not provide a closed form, analytical solution to engineering problems, the numerical description of systems can provide remarkable insight into the fundamentals of fluid dynamics applications and are analogous to laboratory experiments (Anderson et al., 2009). Furthermore, numerical simulation are an efficient, effective, and powerful tool for providing solutions to physical phenomena that cannot be solved analytically.

### *1.2.1. Basic Equations of Motion*

The foundation of fluid mechanics is based on a collection of equations known as the conservation laws. Navier (1822) originally discovered the equations of fluid mechanics using a significant amount of physical intuition and with relatively little attention to mathematical proof (Darrigol, 2002). Over the next few decades, Cauchy, Poisson, and Saint-Venant proposed new derivations of the equations using various methods and approaches (Darrigol, 2002; Galdi,

2011). The equations were not entirely justified, however, until Stokes reinterpreted them using a continuum mechanics approach (Darrigol, 2002; Galdi, 2011). These fundamental physical equations, collectively known as the Navier-Stokes equations, mathematically describe viscous flow and are applicable at the molecular, microscopic, and macroscopic levels (Cebeci, 2005; Galdi, 2011; Theodore, 2011).

Viscous Stresses

Viscous stresses are due to friction between a fluid and solid surface and are defined using the viscous stress tensor ($\bar{\bar{\tau}}$):

$$\bar{\bar{\tau}} = \frac{1}{\rho}\left(\frac{2}{3}\mu - \kappa\right)\left(\vec{\nabla}\cdot\vec{U}\right)\delta - \nu\left[\vec{\nabla}\,\vec{U} + \left(\vec{\nabla}\,\vec{U}\right)^{T}\right] \qquad \textbf{(1.2-1)}$$

where $\rho$ is the fluid density, $\mu$ is the fluid dynamic viscosity, $\kappa$ is the dilatational viscosity, $\nu$ is the fluid dynamic viscosity, $\delta$ is the Kronecker delta, and $\vec{U}$ is the flow velocity vector (Blazek, 2001; Bird, Stewart, and Lightfoot, 2002).

Conservation Laws

Although the concept of the conservation of mass can be traced back to Bernoulli, the equation was first expressed (in limited form) as a partial differential equation by a d'Alembert in 1747 (Craik, 2013; Groth, 2015). A few years later, Euler derived and expressed the conservation of mass as (Blazek, 2001; Darrigol, 2002; Craik, 2013; Groth, 2015):

$$\frac{\partial\rho}{\partial t} + \vec{\nabla}\cdot\left(\rho\vec{U}\right) = 0 \qquad \textbf{(1.2-2)}$$

where $t$ is time.

**Equation 1.2-2**, or the continuity equation, expressed in integral form:

$$\frac{\partial}{\partial t}\int \rho \, dV + \oint \rho(\vec{U} \cdot \vec{n}) \, dA = 0 \qquad \textbf{(1.2-3)}$$

where $\vec{n}$ is the unit normal vector, $V$ is the control volume, and $A$ is the surface area of the control element.

Euler then went on to develop the equations of motion using Newton's second law (Darrigol, 2002; Galdi, 2011):

$$\vec{F} = m\vec{a} \qquad \textbf{(1.2-4)}$$

where $\vec{F}$ is the net force acting on an element, $m$ is the mass of the element, and $\vec{a}$ is the acceleration of the element.

By equating the forces acting on a square element of fluid, Euler developed an equation for the conservation of momentum (Blazek, 2001; Darrigol, 2002):

$$\frac{\partial(\rho\vec{U})}{\partial t} + \vec{\nabla} \cdot (\rho\vec{U}\,\vec{U} + p\delta - \bar{\bar{\tau}}) = \rho\vec{f} \qquad \textbf{(1.2-5)}$$

where $\vec{f}$ is acceleration due to body forces and $p$ is the isotropic pressure.

The integral form of the conservation of momentum is:

$$\frac{\partial}{\partial t}\int \rho\vec{U} dV = -\oint (\rho\vec{U}\vec{U} + p\delta - \bar{\bar{\tau}}) \cdot \vec{n} \; dA + \int \rho\vec{F} dV \qquad \textbf{(1.2-6)}$$

An additional law for the conservation of energy also exists. but, as thermal effects are not considered in this study, only **Equations 1.2-1** and **1.2-4** are considered further.

Navier-Stokes Equations

The Navier-Stokes equations may be obtained by substituting **Equation 1.2-1** into **Equations 1.2-2** and **1.2-5** to yield (Sayma, 2009):

$$\frac{D\vec{U}}{Dt} = \nu\vec{\nabla}^2\vec{U} - \frac{1}{\rho}\vec{\nabla}p \qquad \textbf{(1.2-7)}$$

### *1.2.2. Spatial Discretization of Governing Equations*

Although the CFD software (ANSYS® Fluent®) used in this study employs a finite-volume method, a brief discussion of two other common approaches (the finite difference and finite element methods) for discretizing the flow domain is given below. In theory, all computational methods should result in the same final solutions, although there may be discrepancies between approaches for complicated problems (Chung, 2010).

In addition to the computational methods discussed below, there are several numerical schemes available with which the spatial discretization can be performed. For viscous fluxes, a central scheme is typically used to average conservative variables and evaluate the flux at a control volume. Another option, however, are upwind schemes, which are more advanced because they consider the physics of the governing equations. In general, central schemes require less effort than upwind schemes, although the latter are more accurate for capturing discontinuities and, in many cases, can require less grid points than central schemes (Blazek, 2000).

#### Finite Difference Method

In the finite difference method, one discrete unknown variable is assigned to each discretization point in the flow domain. Using Taylor series expansions, the equations associated with each variable are then expressed as forward difference, backward difference, or central difference equations such that the

local truncation error is minimized at each point (Eymard, Gallouet, and Herbin, 200; Veldman, 2012; Chung, 2010).

In some cases, the finite difference method is simple and easy to implement and can obtain high-order approximations. This approach can present challenges, however, if there are discontinuities in the equations to be solved (Eymard, Gallouet, and Herbin, 2006). The method also requires a structured grid (discussed below) and cannot be applied to curvilinear coordinates, which can greatly restrict the systems it is capable of modeling (Blazek, 2006). Due to these limitations, the finite difference method is no longer widely used.

## Finite Element Method

The finite element method utilizes piecewise polynomial interpolation to develop a set of algebraic equations that must be simultaneously solved. Weighted residuals are also used to measure the errors associated with these approximations. Although the finite element method may be used on complex geometries, it requires greater computational resources and processing power than other methods and is therefore not used extensively in most fluid dynamics applications (Tu, Yeoh, and Liu, 2013).

## Finite Volume Method

When using the finite volume method, a control volume is created around each discretized cell in the simulated geometry, within which all fluxes are balanced using the integral forms of the conservation laws (Eymard, Gallouet, and Herbin, 2006; Anderson et al., 2009). A cell-centered scheme, in which the control volumes are identical to the grid cells in the geometry, or a cell-vertex

scheme, in which the control volume is either a union of all cells that share a particular grid point or is centered around a grid point, are two of the most common approaches to defining the shape and position of the control volume (Blazek, 2006).

The finite volume method is capable of numerically solving elliptic, parabolic, and hyperbolic conservation laws and can be used on arbitrary geometries involving structured or unstructured meshes. This discretization method ensures that the discretization is locally and globally conservative and is thus one of the more robust options for modeling fluid dynamics applications (Eymard, Gallouet, and Herbin, 2006). As stated previously, the finite volume method is utilized by the CFD software package ANSYS® Fluent® and is used in the studies outlined herein.

## Grid Generation

Many methods are available to numerically solve the Navier-Stokes equations. Meshes may be either structured, in which the cells are regularly distributed or unstructured, in which the cells are distributed according to areas of interest in the flow and, thus, may assume a number of different geometrical shapes (Tu, Yeoh, and Liu, 2013).

A structured mesh (**Figure 1.2-1**) uses a set of indices ($\mathbf{i}, \mathbf{j}, \mathbf{k}$) that are equal to spatial dimensions such that adjacent element indices differ by a value of one. As a consequence, each element corresponds to a unique index set. Structured meshes offer the advantage of easier data management and programming (Tu, Heng Yeoh, and Liu, 2012). In complex geometries, however,

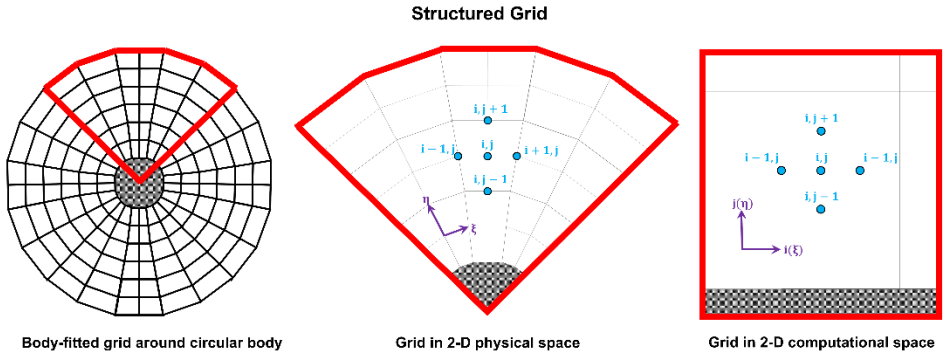


**Figure 1.2-1: Schematic of a structured body-fitted grid around a circular body and its corresponding 2-dimensional representation in physical and computational spaces .**

structured meshes may become extremely skewed, which can lead to unphysical and inaccurate solutions and can also cause increased computational time (Tu, Heng Yeoh, and Liu, 2012; Pletcher, Tannehil, and Anderson, 2013).

An unstructured mesh (**Figure 1.2-2**), on the other hand, uses cell-to-cell pointers. Thus, there is no direct relationship between the spatial dimension and the location of a cell. In general, unstructured meshes do not have regular arrangements of cells or lines that correspond to curvilinear coordinates (Tu, Heng Yeoh, and Liu, 2012; Pletcher, Tannehil, and Anderson, 2013). Thanks to the flexibility and simplicity of this approach, unstructured grids are used by most commercial CFD codes (including ANSYS® Fluent®).

Solutions obtained using computational fluid dynamics must be independent of the grid or mesh used in the numerical calculations. To ensure such independence is obtained, an independence analysis must be conducted using various grids of increasing node density. Grid independence is obtained when predictions for the flow variables of interest (e.g. velocities, pressures, wall stresses) no longer change when the number of nodes in the mesh is increased.

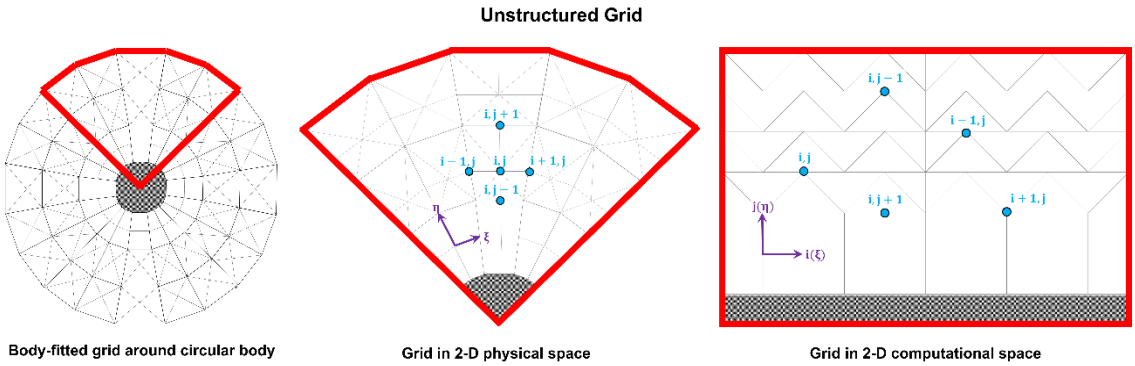


**Figure 1.2-2: Schematic of an unstructured body-fitted grid around a circular body and its corresponding 2-dimensional representations in physical and computational spaces.**

It is important to note that the node density necessary for grid independence will depend on the system and type of flow. A graphical example of grid independence analyses for laminar and turbulent channel flow are shown in **Figures 1.2-3** and **1.2-4**, respectively.

### *1.2.3. Temporal Discretization of Governing Equations*

Since many types of flow problems are unsteady, the solution at a point with the flow domain will vary with time. Time-stepping schemes may be explicit or implicit. With an explicit scheme, only one unknown term appears in each equation to be solved at every time step (Blazek, 2001; Sayma, 2009; Pletcher, Tannehill, and Anderson, 2013). With an implicit scheme, however, a system of algebraic equations must be solved simultaneously at each new time step (Pletcher, Tannehill, and Anderson, 2013).

The choice of an explicit or implicit time-stepping method is generally based on the stability of the solution. Several techniques have been proposed for determining stability, such as the discrete perturbation stability analysis or the von Neumann stability analysis or (Hoffmann and Chiang, 2000; Pletcher,

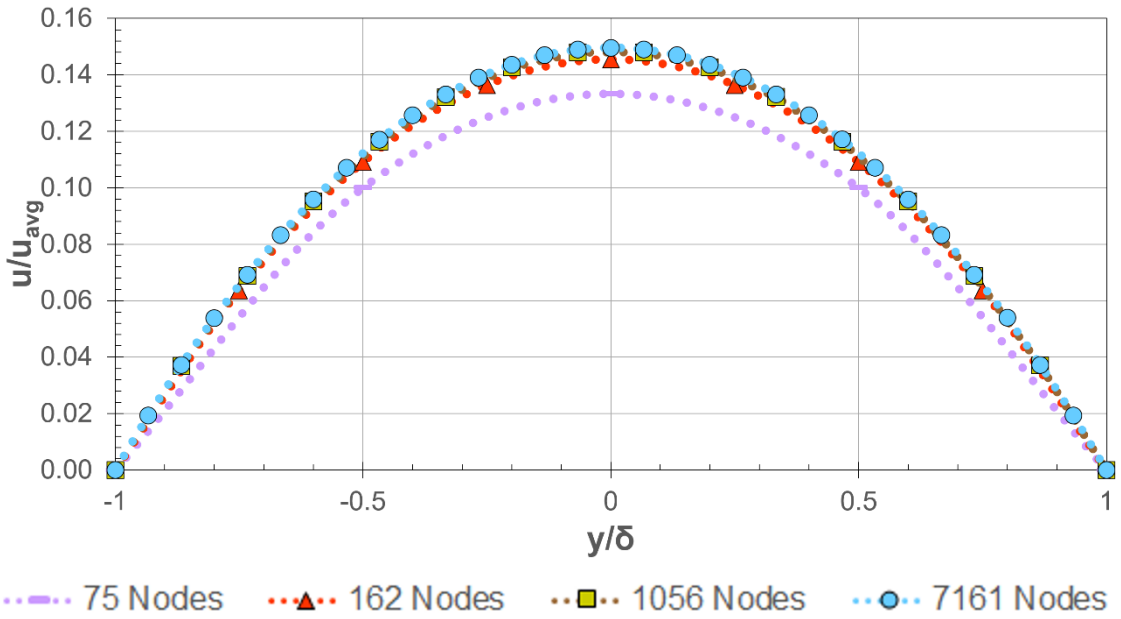


**Figure 1.2-3: Differences in numerical laminar (Re≈350) velocity profile predictions due to node number for flow of water in a 5 μm x 6 μm x 2.5 μm micro-duct.**

Tannehill, and Anderson, 2013). In the discrete perturbation stability analysis, a disturbance is introduced to the system. The numerical method is considered unstable if the disturbance grows with the solution and stable if the disturbance dies out (Hoffmann and Chiang, 2000). In a von Neumann stability analysis, the solution to a linear finite difference equation is expanded using a Fourier series. The amplification factor is then monitored for decay or growth, which indicates stability (Hoffmann and Chiang, 2000).

A convenient criterion for determining the appropriate time-stepping scheme is based on the Courant-Friedrichs-Lewy (CFL) condition. According to the CFL condition for the one-dimensional linear convection equation, the time step ($\mathbf{\Delta t}$) is found according to:

$$\Delta t = \sigma \frac{\Delta x}{|\Lambda_c|} \qquad \textbf{(1.2-8)}$$

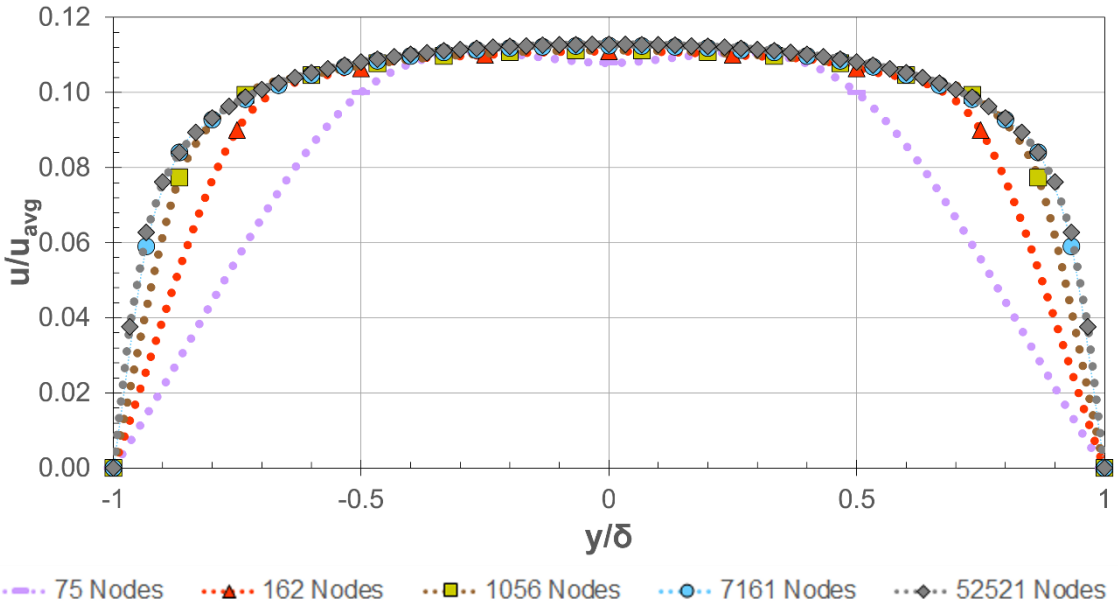


**Figure 1.2-4: Differences in numerical turbulent (Re≈3,500) velocity profile predictions due to node number for flow of water in a 5 μm x 6 μm x 2.5 μm micro-duct using the standard k-ε model for turbulence.**

where $\Delta x$ is the cell size, $\Lambda_c$ is the maximum eigenvalue of the convective flux Jacobian, and $\sigma$ is a positive coefficient called the CFL number (Blazek, 2001). In general, explicit time-stepping is best for applications in which the CFL number is on the order of unity. On the other hand, implicit time-stepping is a more appropriate choice when the CFL number is much larger than one (Blazek, 2001).

### *1.2.4. Numerical Solution Processing*

CFD can provide remarkably accurate and useful insight into complex and elaborate systems. It should be noted, however, that results obtained using computational fluid dynamics are only as accurate as the physical models used to describe the system and are subject to both truncation and round-off errors (Anderson et al., 2009). Numerical simulation analysis is an involved process

that consists of three stages, each of which is crucial if an accurate solution is to be obtained.

In the first stage of analysis, commonly referred to as the pre-processing stage, the geometry of the region of flow, known as the computational domain, is defined and created. Once the geometry is created, a mesh is generated by dividing the domain geometry into a finite number of smaller subdomains.

The accuracy of solutions obtained using CFD is greatly influenced by the number of nodes in the grid, as well as the quality of and type of mesh. Computational cost and calculation turnover are also highly sensitive to these properties and will generally increase with increasing cell size and complexity. Thus, a trade-off exists between numerical accuracy and computational efficiency. The final steps in the pre-processing stage are the selection of the physics and fluid properties associated with the system to be modeled, followed by the specification of boundary conditions that realistically represent the physical system (Tu, Yeoh, and Liu, 2013).

In the next stage of the analysis, a solver is chosen, the solution is initialized, and a discretization scheme is selected. The solver is then allowed to begin calculating the solution. During this stage, convergence is monitored by tracking the advancement of the residuals of the calculations of the equations being solved through each iteration step. A solution may be considered converged once these residuals fall below some pre-determined criteria (Tu, Yeoh, and Liu, 2013).

Once a solution has been obtained, the results are processed in the stage of CFD analysis known as the post-process stage. Many commercial CFD programs offer visualization tools to assist in analyzing the relevant physical characteristics of the flow (Tu, Yeoh, and Liu, 2013).

## 1.3. Turbulent Flow

Turbulent flows are the most common flows that occur in nature and engineering applications (Tennekes and Lumley, 1972). The primary objective in the study of turbulent flows is to obtain a tractable theory or model that can be applied to practical applications. While an exact definition for turbulent flow cannot be given without significantly restricting the defined system, turbulence is a continuum phenomenon which occurs at high Reynolds numbers and is rotational, three-dimensional, and irregular, with diffusive and dissipative characteristics (Tennekes and Lumley, 1972). Numerous techniques have been employed to understand systems involving this type of flow, yet, due in large part to the closure problem, turbulence still remains “one of the great unsolved problems of classical physics” (Tennekes and Lumley, 1972).

### *1.3.1. Reynolds Equations*

#### Reynolds Decomposition

When involving constant property Newtonian fluids, turbulent flow is governed by the Navier-Stokes equations, as given in **Equation 1.2-7**. In laminar flow, these equations can be used to directly calculate the velocity at a specific point in space and time. In turbulent flow, however, the velocity field is random and is consequently inherently unpredictable (Pope, 2000). Thus, statistical quantities, such as means and correlations, must be employed to describe the turbulent velocity fields. The Reynolds decomposition may be used to describe the velocity ($\vec{\mathbf{U}}$) as a composition of a mean component ($\langle\vec{\mathbf{U}}\rangle$) and a fluctuating component ($\vec{\mathbf{u}}$), according to (Pope, 2000)**:**

$$\vec{\mathbf{U}} = \langle \vec{\mathbf{U}} \rangle + \vec{\mathbf{u}} \qquad \textbf{(1.3-2)}$$

The equation for the evolution of the mean velocity field may be derived from the Navier-Stokes equations (**Equation 1.2-7**) to yield the Reynolds equations:

$$\frac{\bar{\mathbf{D}}\langle \vec{\mathbf{U}} \rangle}{\bar{\mathbf{D}}\mathbf{t}} = \boldsymbol{\nu}\vec{\boldsymbol{\nabla}}^{\mathbf{2}}\langle \vec{\mathbf{U}} \rangle - \frac{\mathbf{1}}{\boldsymbol{\rho}}\vec{\boldsymbol{\nabla}}\langle \mathbf{p} \rangle - \vec{\boldsymbol{\nabla}}\langle \vec{\mathbf{u}}\vec{\mathbf{u}} \rangle \qquad \textbf{(1.3-3)}$$

where the brackets denote the mean value of the variable inside, $\boldsymbol{\nu}$ is the fluid kinematic viscosity, $\boldsymbol{\rho}$ is the fluid density, $\langle \mathbf{p} \rangle$ is the mean pressure, and $\langle \vec{\mathbf{u}}\vec{\mathbf{u}} \rangle$ is the velocity covariance, also known as the Reynolds stresses.

The Reynolds stresses are used to describe momentum transfer due to the fluctuating velocity field in turbulent flows and play an important role in the equations for the mean velocity field of turbulent flow (Pope, 2000).

Closure Problem

In general, for a three-dimensional turbulent flow, there are four independent equations governing the system: three components of the Reynolds equations and either the mean continuity equation or the Poisson equation. The closure problem in turbulence arises from the fact that these four equations contain more than four unknowns: the four quantities associated with $\langle \mathbf{U} \rangle$ and $\langle \mathbf{p} \rangle$, as well as the Reynolds stresses. Consequently, the Reynolds equations are unclosed and cannot be solved in the absence of separate information (Pope, 2000; Pletcher, Tannehill, and Anderson, 2013). Two of the most popular ways to relate the Reynolds stresses to the mean velocity gradients are the turbulent-viscosity hypothesis and the gradient-diffusion hypothesis (Pope, 2000).

The turbulent-viscosity hypothesis is defined as:

$$\langle \vec{\mathbf{u}}\vec{\mathbf{u}} \rangle = \frac{2}{3}\mathbf{k}\boldsymbol{\delta} - \boldsymbol{\nu}_{\mathbf{T}}\left[\vec{\boldsymbol{\nabla}}\langle \vec{\mathbf{U}} \rangle + \left(\vec{\boldsymbol{\nabla}}\langle \vec{\mathbf{U}} \rangle\right)^{\mathbf{T}}\right] \quad \textbf{(1.3-4)}$$

where $\boldsymbol{\delta}$ is the Kronecker delta, $\boldsymbol{\nu}_{\mathbf{T}}$ is the turbulent kinematic viscosity, and $\mathbf{k}$ is the turbulent kinetic energy.

The gradient-diffusion hypothesis is given by:

$$\langle \vec{\mathbf{u}}\boldsymbol{\phi} \rangle = -\boldsymbol{\Gamma}_{\mathbf{T}}\vec{\boldsymbol{\nabla}}\langle \boldsymbol{\phi} \rangle \quad \textbf{(1.3-5)}$$

where $\langle \vec{\mathbf{u}}\boldsymbol{\phi} \rangle$ is the scalar flux, $\boldsymbol{\Gamma}_{\mathbf{T}}$ is the turbulent diffusivity, and $\langle \boldsymbol{\phi} \rangle$ is the mean of a conserved passive scalar field.

The Boussinesq hypothesis offers the advantage of a low computational cost associated with the calculation of the turbulent viscosity, but the hypothesis assumes the turbulent viscosity is an isotropic scalar quantity, which is not always valid. This model is generally accurate, however, for many technical flows, boundary layers, mixing layers, and jets (Pope, 2000). In the gradient-diffusion hypothesis, the scalar flux is described as scaling with the mean scalar gradient field, which is not true. Due to this inconsistency, the hypothesis is usually only used in simple two-dimensional flows (Pope, 2000).

### *1.3.2. Viscous Scales*

When considering wall-bounded turbulent flows (such as those considered in this study), the characteristic velocity and length scales may be described using dimensionless variables called viscous scales (Pope, 2000).

The friction velocity ($\mathbf{u}_{\boldsymbol{\tau}}$) is given as:

$$\mathbf{u_\tau} \equiv \sqrt{\frac{\boldsymbol{\tau_w}}{\boldsymbol{\rho}}} \tag{1.3-6}$$

where $\boldsymbol{\tau_w}$ is the wall shear stress.

Using the friction velocity, the viscous velocity ($\mathbf{u^+}$) may be defined as:

$$\mathbf{u^+} \equiv \frac{\langle \vec{\mathbf{U}} \rangle}{\mathbf{u_\tau}} \tag{1.3-7}$$

Similarly, the viscous length scale ($\mathbf{l^*}$) is:

$$\mathbf{l^*} \equiv \frac{\boldsymbol{\nu}}{\mathbf{u_\tau}} \tag{1.3-8}$$

The friction Reynolds number ($\mathbf{Re_\tau}$) would then be:

$$\mathbf{Re_\tau} \equiv \frac{\mathbf{u_\tau l}}{\boldsymbol{\nu}} = \frac{\mathbf{l}}{\mathbf{l^*}} \tag{1.3-9}$$

where $\mathbf{l}$ is the characteristic length scale of the system.

Finally, the viscous length ($\mathbf{y^+}$) is:

$$\mathbf{y^+} \equiv \frac{\mathbf{y}}{\mathbf{l^*}} = \frac{\mathbf{u_\tau y}}{\boldsymbol{\nu}} \tag{1.3-10}$$

where $\mathbf{y}$ is the distance from the wall.

**Equation 1.3-10** is particularly useful for defining near-wall regions, for which mean velocity profiles and certain flow properties can be predicted, according to:

$$\frac{\mathbf{d}\langle \vec{\mathbf{U}} \rangle}{\mathbf{dy}} = \frac{\mathbf{u_\tau}}{\mathbf{y}} \mathbf{f}\left(\mathbf{y^+}, \frac{\mathbf{y}}{\mathbf{l}}\right) \tag{1.3-11}$$

where $\mathbf{f}$ is a universal dimensionless function.

The area closest to the wall is known as the inner layer ($\mathbf{y/l < 0.1}$) and is made up of two regions called the viscous sublayer ($\mathbf{y^+ < 5}$) and the buffer layer. In the inner layer, the mean velocity profile is described by:

$$\frac{\mathbf{d\langle \vec{U} \rangle}}{\mathbf{dy}} = \frac{\mathbf{u_\tau}}{\mathbf{y}} \mathbf{f_I}(\mathbf{y^+}) \tag{1.3-12}$$

where

$$\mathbf{f_I}(\mathbf{y^+}) = \lim_{\mathbf{y/l \to 0}} \mathbf{f}\left(\mathbf{y^+}, \frac{\mathbf{y}}{\mathbf{l}}\right) \tag{1.3-13}$$

The friction velocity in the viscous sublayer follows the relationship:

$$\mathbf{u^+ = y^+} \tag{1.3-14}$$

In the buffer layer ($\mathbf{5 < y^+ < 30}$), the flow will transition from viscous-dominated to turbulence-dominated before entering the outer layer.

The next region ($\mathbf{y^+ > 30}$) is the log-law region, which has a mean velocity described by:

$$\mathbf{u^+} = \frac{\mathbf{1}}{\boldsymbol{\kappa}} \mathbf{ln}(\mathbf{y^+}) + \mathbf{B} \tag{1.3-15}$$

where $\boldsymbol{\kappa} = \mathbf{0.41}$ is the von Kármán constant and $\mathbf{B} = \mathbf{5.2}$ is a constant.

In the outer layer ($\mathbf{y^+ > 50}$), the effects of viscosity on the mean velocity become negligible and the mean velocity profile is described by:

$$\frac{\mathbf{d\langle \vec{U} \rangle}}{\mathbf{dy}} = \frac{\mathbf{u_\tau}}{\mathbf{y}} \mathbf{f_0}\left(\frac{\mathbf{y}}{\mathbf{l}}\right) \tag{1.3-16}$$

where

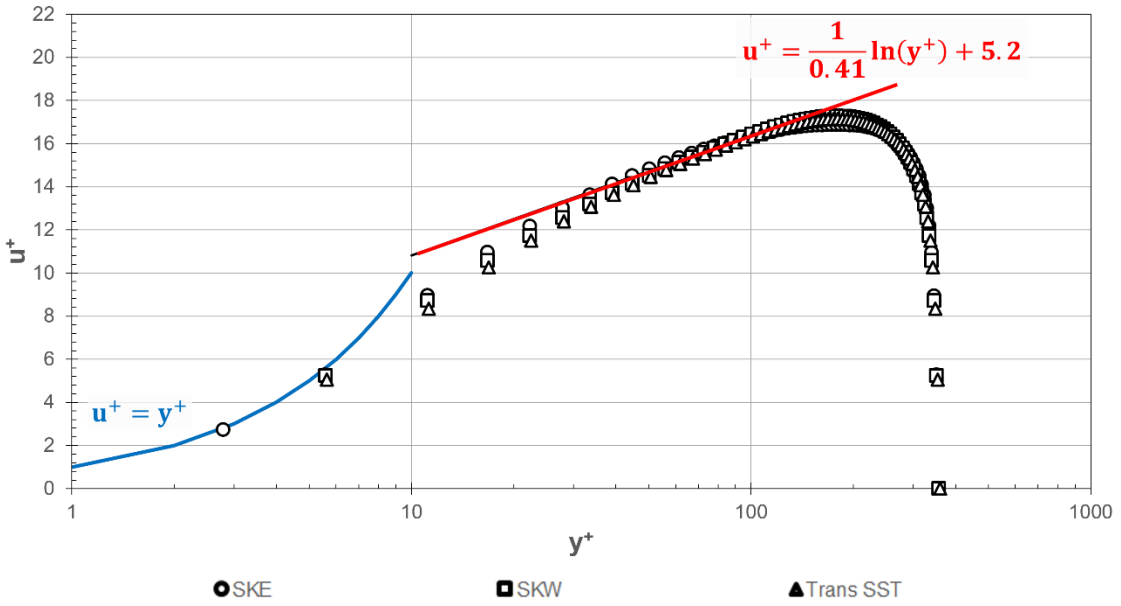


**Figure 1.3-1: Numerical velocity profiles in viscous wall ($y^+<5$) and log-law ($y^+>30$) regions for turbulent flow of water between two infinite parallel plates separated at a distance of 360 μm for $Re_\tau = 180$. DNS data obtained from Martell, Perot, and Rothstein (2009).**

$$\mathbf{f_0}\left(\frac{\mathbf{y}}{\mathbf{l}}\right) = \lim_{\mathbf{y^+}\to\infty} \mathbf{f}\left(\mathbf{y^+}, \frac{\mathbf{y}}{\mathbf{l}}\right) \tag{1.3-17}$$

At large Reynolds numbers ($\mathbf{Re} > \mathbf{20,000}$), an overlap region will exist between the inner and outer layers. In this region, $\mathbf{f_I}(\mathbf{y^+})$ and $\mathbf{f_0}\left(\frac{\mathbf{y}}{\mathbf{l}}\right)$ are both equal and constant (Pope, 2000).

**Figure 1.3-1** illustrates the relationships given in **Equations 1.3-14** and **1.3-15** using velocity estimates obtained from several popular turbulent flow models (see **Section 1.3.3.**). All models are able to accurate capture the predicted flow profiles in the viscous sublayer and log-law regions.

### *1.3.3. Models for Turbulence*

Turbulent flow presents many modeling challenges to the development of an analytical theory or numerical model. For instance, the pressure-gradient is non-linear and non-local, while the velocity field is three-dimensional, time-dependent, and random. Turbulent structures can also include an array of time- and length-scales and are influenced by the geometry of the system and boundaries (Pope, 2000).

Because of the closure problem associated with turbulent flow calculations, an assumption must be made about the apparent turbulent stress quantities before numerical solutions may be obtained. Numerous models for closing the Reynolds equations have been developed, all of which have unique advantages and limitations. In general, these models can be classified as algebraic, one-equation, multiple-equation, second-order closures, and large-eddy simulation (Blazek, 2001).

<u>Algebraic Models</u>

Most algebraic models for turbulence utilize a mixing length ($\mathbf{l_m}$) to estimate the turbulent viscosity. In such models, the mixing length is dependent on the velocity gradients in the system, according to: (Pope, 2000; Pletcher, Tannehill, and Anderson, 2013):

$$\boldsymbol{\nu_T = l_m^2 \left| \frac{\partial \langle \vec{U} \rangle}{\partial y} \right|} \qquad \textbf{(1.3-18)}$$

The mixing-length model is typically applicable to all turbulent flows and, though incomplete, is perhaps the simplest solution to the closure problem.

Because the mixing length must be specified, however, this task can prove to be quite involved for complex flow. (Pope, 2000; Pletcher, Tannehill, and Anderson, 2013).

One-Equation Models

Numerous models have been developed to offer closure to the turbulence kinetic energy equation (Wilcox, 1994). Among the most popular one-equation models is the Spalart-Allmaras model, which offers model equations for the eddy viscosity.

To account for the non-zero value of the turbulent velocity scale when the velocity gradient is zero, both Kolmogorov and Prandtl developed a model for the turbulent viscosity based on the turbulent kinetic energy (Pope, 2000):

$$\boldsymbol{\nu_T = 0.55 k^{\frac{1}{2}} l_m} \tag{1.3-19}$$

The turbulent kinetic energy may then be described by the model transport equation:

$$\boldsymbol{\frac{\bar{D}k}{\bar{D}t} = \vec{\nabla} \cdot \left( \frac{\nu_T}{\sigma_k} \vec{\nabla} k \right) + \mathcal{P} - \varepsilon} \tag{1.3-20}$$

where $\boldsymbol{\sigma_k = 1.0}$. In these models, the production of turbulent kinetic energy ($\boldsymbol{\mathcal{P}}$) and the dissipation of turbulent kinetic energy ($\boldsymbol{\varepsilon}$) are given as (Pope, 2000):

$$\boldsymbol{\mathcal{P} = -\langle \vec{u}\vec{u} \rangle \nabla \langle \vec{U} \rangle} \tag{1.3-21}$$

$$\boldsymbol{\varepsilon = \frac{C_D k^{\frac{3}{2}}}{l_m}} \tag{1.3-22}$$

where $\boldsymbol{C_D}$ is a model constant.

A one-equation model has been shown to be more accurate than a mixing-length model, but is nonetheless still limited by the necessity of specifying the mixing length scale (Pope, 2000). Since they do not account for the effects of transport on the turbulence length scale, more rigorous and universal two-equation models are commonly used (Wilcox, 1994).

Two-Equation Models

Two-equation models can be used to predict properties of turbulent flow without prior knowledge of the turbulence structure and, as a consequence, are the turbulence models best suited to study many types of flows (Wilcox 1994). Two of the most popular Reynolds-Averaged Navier-Stokes (RANS) models are the k-epsilon (**k-ε**) and the k-omega (**k-ω**) models for turbulence. These two-equation models are used to solve for the turbulent kinetic energy, along with an additional transport variable (Pope, 2000). In the **k-ε** model, a model transport equation for the dissipation of turbulent kinetic energy is defined as:

$$\frac{\bar{\mathbf{D}}\boldsymbol{\varepsilon}}{\bar{\mathbf{D}}\mathbf{t}} = \vec{\boldsymbol{\nabla}} \cdot \left(\frac{\boldsymbol{\nu_T}}{\boldsymbol{\sigma_\varepsilon}} \vec{\boldsymbol{\nabla}}\boldsymbol{\varepsilon}\right) + \mathbf{C_{\varepsilon 1}} \frac{\boldsymbol{\mathcal{P}}\varepsilon}{\mathbf{k}} - \mathbf{C}_{\varepsilon 2} \frac{\varepsilon^2}{\mathbf{k}} \qquad \textbf{(1.3-11)}$$

where the constants are $\boldsymbol{\sigma_\varepsilon} = \mathbf{1.3}$, $\mathbf{C_{\varepsilon 1}} = \mathbf{1.44}$, and $\mathbf{C}_{\varepsilon 2} = \mathbf{1.92}$ (Pope, 2000). All other terms are defined previously.

An exact equation for the turbulent dissipation rate in the dissipative range can also be derived. However, **ε** is best considered in the energy-containing range of the energy cascade, thus making the exact equation impractical for use in a turbulence model (Pope, 2000). As a consequence, it is generally more useful to use the empirical relationship given in **Equation 1.3-11** for the standard model equation for **ε**. The **k- ε** model is generally accurate for simple flows but

can provide qualitatively incorrect flow patterns for complex flows due to the turbulent-viscosity hypothesis and the empirical nature of **Equation 1.3-11** (Pope, 2000).

In the **k- ω** model, a model transport equation for the specific dissipation rate is introduced according to (Pope, 2000):

$$\frac{\bar{\mathbf{D}}\boldsymbol{\omega}}{\bar{\mathbf{D}}\mathbf{t}} = \vec{\boldsymbol{\nabla}} \cdot \left(\frac{\boldsymbol{\nu_T}}{\boldsymbol{\sigma_\omega}} \vec{\boldsymbol{\nabla}}\boldsymbol{\omega}\right) + \mathbf{C_{\omega 1}} \frac{\boldsymbol{\mathcal{P}\omega}}{\mathbf{k}} - \mathbf{C_{\omega 2}} \frac{\boldsymbol{\omega}^2}{\mathbf{k}} \qquad \textbf{(1.3-12)}$$

Where, for homogeneous turbulence, the constants are $\boldsymbol{\sigma_\omega = 1.3}$, $\mathbf{C_{\omega 1}} = \mathbf{C_{\varepsilon 1} - 1}$, $\mathbf{C_{\omega 2} = C_{\varepsilon 2} - 1}$.

The **k- ω** model is the most accurate two equation model for viscous near-wall regions of boundary layer flows and for accounting for the effects of stream-wise pressure gradients but is sensitive to the boundary condition for $\boldsymbol{\omega}$, which can pose a problem for non-turbulent free-stream boundaries (Pope, 2000).

### *1.3.4. Alternative Computational Methods*

#### Direct Numerical Simulations

Direct numerical simulations (DNS) are used to solve for the turbulent velocity field by solving the Navier-Stokes momentum equations without the use of any turbulence model. As a consequence, all spatial scales, ranging from the smallest Kolmogorov scales to the largest integral scales, must be resolved in the computational mesh. To sufficiently resolve the dissipative scales, the grid spacing ($\boldsymbol{\Delta x}$) should be on the order of (Pope, 2000):

$$\boldsymbol{\Delta x} = \frac{\boldsymbol{\pi}}{\mathbf{1.5}} \boldsymbol{\eta} \qquad \textbf{(1.3-13)}$$

Where $\boldsymbol{\eta}$ is the Kolmogorov length scale.

For a three-dimensional system, the spatial-resolution requirement given in **Equation 1.3-13** requires the total number of grid nodes ($\mathbf{N}$) to be (Pope, 2000):

$$\mathbf{N^3 \sim 4.4 Re^{9/4}} \qquad \textbf{(1.3-14)}$$

where $\mathbf{Re}$ is the Reynolds number.

If the solution is to be advanced in time as well as space, the time step ($\mathbf{\Delta t}$) may only be a small fraction of the grid spacing. A useful measure to ensure the accuracy and stability of the solution is given by the Courant number ($\mathbf{C}$) (Pope, 2000):

$$\mathbf{C = \frac{k^{1/2} \Delta t}{\Delta x} = \frac{1}{20}} \qquad \textbf{(1.3-15)}$$

Because the computational cost associated with DNS increases significantly with increasing Reynolds number, this approach is generally only suitable for flows with low Reynolds numbers. Since all scales of motion are resolved, however, DNS provides the most accurate realizations of flow and are the simplest numerical method for simulating turbulent flows (Modi, 1999).

The friction velocity obtained using DNS is compared with those from the standard **k-ε** (**SKE**) and the standard **k-ω (SKW)** models for turbulence (discussed previously), as well as another popular model called the Transition Shear Stress Transport (**Trans SST**) model in **Figure 1.3-2**. The SKE, SKW, and Trans SST models predict friction velocities with maximum errors of 8%, 6%, and 7%, when compared to DNS solutions. **Figure 1.3-3** compares the Reynolds

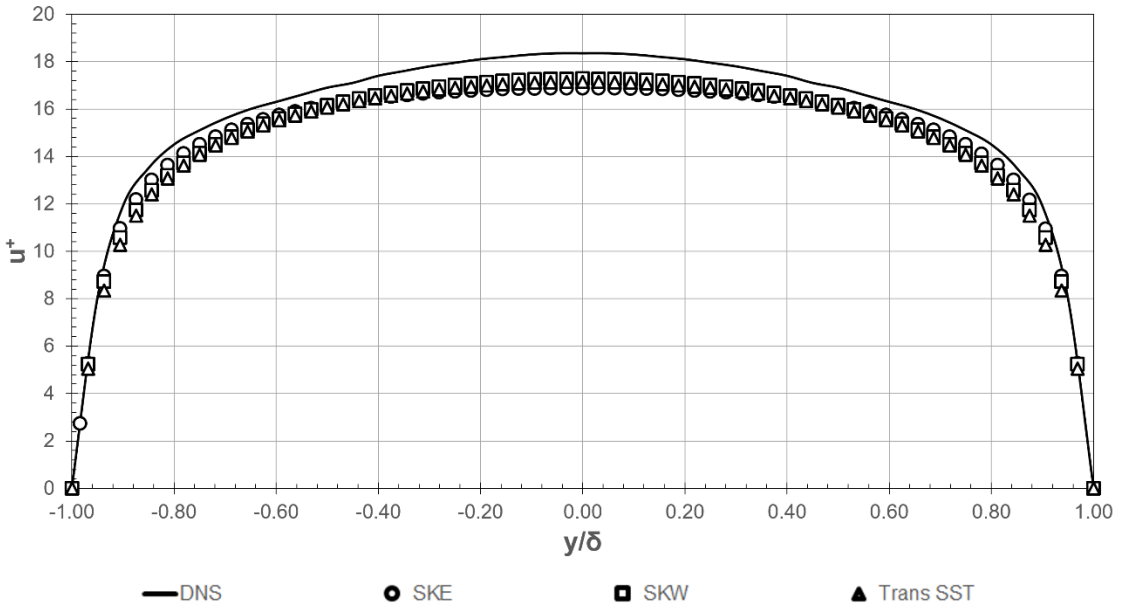


**Figure 1.3-2: Numerical mean velocity profiles in turbulent flow between two infinite parallel plates separated at a distance of 360 μm for $Re_\tau$ = 180. DNS data obtained from Martell, Perot, and Rothstein (2009).**

stress profiles from DNS and the **SKE**, **SKW**, and **Trans SST** models. The maximum error associated with all numerical models is less than 1%.

Large Eddy Simulations

Large eddy simulations (LES) are another method used in computational fluid dynamics to model turbulence. These simulations are closely related to direct numerical simulation, in which all of the scales of motion of turbulence are computed. While direct numerical simulations usually require a large number of grid points and can result in substantial expenses, large eddy simulations explicitly represent only the largest scales of motion, while treating smaller scales using an approximate parameterization or model (Ferziger, 1996; Fröhlich and Rodi, 2002). This approach to modeling flows in Fluent® allows for coarser grids and larger time steps than direct numerical simulations (ANSYS® Fluent®, 2006). Nevertheless, LES tends to require finer meshes than those used in more

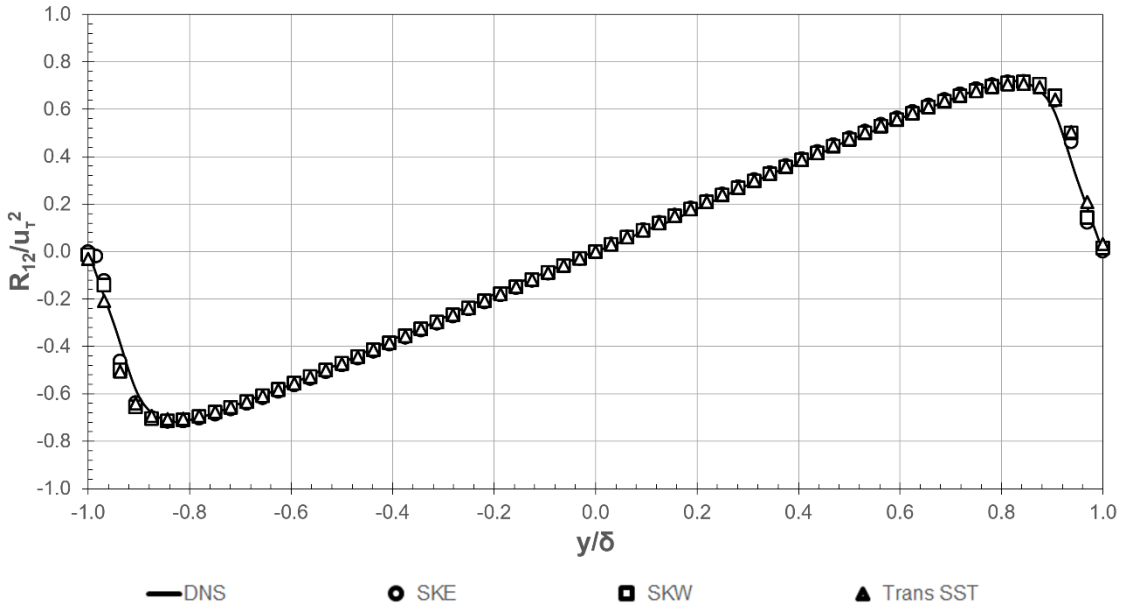


**Figure 1.3-3: Numerical Reynolds stresses in in turbulent flow between two infinite parallel plates separated at a distance of 360 μm for $Re_\tau$ = 180. DNS data obtained from Martell, Perot, and Rothstein (2009).**

generalized turbulence models and must be run for a sufficiently long period of time to obtain stable statistics. Therefore, it is advantageous, when practical, to use other models for turbulence, such as the Reynolds-Averaged Navier Stokes models discussed in **Chapter 1.2.3**, to model flow in simple geometries (Pope, 2000).

## 1.4. Superhydrophobic Surfaces

### *1.4.1. Introduction and Background*

Examples of the importance of roughness elements in superhydrophobic surfaces (SHSs) can be seen frequently in nature, such as in the case of the self-cleaning lotus leaf and the water strider (Barthlott and Neinhuis, 1997; Gao and Jiang, 2004; Voronov et al., 2008). It has further been shown by Bhushan and Jung (2006) that a thin wax film and roughness elements are responsible for the superhydrophobicity of many types of leaves, including the lotus. Similarly, the SH nature of the legs of the water strider can be shown to be due to the micro- and nano-structures that cover the legs of the insect (Gao and Jiang, 2004). Quéré and Reyssat (2008) later concluded that all SH materials found in nature are coated with some form of a waxy substance. In cases where nano-scale secondary roughness covers parts of the surface, SH effects are augmented, since gas can be trapped within the nanoscale while the space between the microscale roughness is wetted by the fluid—this is the case in the ‘‘rose-petal effect’’ (Bhushan and Nosonovsky, 2010).

The behavior of SHSs was first observed over 2,000 years ago, when the leaves of some plants were seen to possess a self-cleaning characteristic that enabled the fauna to survive in dirty environments (Guo, Liu, and Su, 2011). The most popular example of such plants is the lotus leaf, on which water may be seen to form distinct droplets or beads that naturally roll off the leaf surface, while also removing dirt particles and other debris[8]. Despite this observation, however, the true mechanism of the lotus leaf’s self-cleaning ability could not be examined

further until the invention of the scanning electron microscope in the 1960s (Guo, Liu, and Su, 2011). After the development of the microscope, the surface of the lotus leaf was discovered to consist of microstructures in the shape of conical posts of 3-10 μm in size, on which were nanometer-sized roughness between 70-100 nm in size. Since the first observation of the behavior of water droplets on the lotus leaf, many other plants, insects, and even animals, such as rice leaves, water striders, and fast-swimming sharks, have been found to exhibit similar self-cleaning and water-repellency characteristics. These natural SHSs have inspired the development of artificial surfaces that utilize micro- and nanostructures to create anti-icing, self-cleaning, and corrosion-resistant surfaces for use in a variety of commercial and industrial applications, including biomedicine, separation processes, and fluid transport (Guo, Liu, and Su, 2011; Voronov and Papavassiliou, 2008).

### *1.4.2. Surface Wettability*

The hydrophobic or hydrophilic character of a surface is largely dependent on the surface's degree of wetting, or wettability, which is determined based on whether a liquid will spread over the surface. The wettability of a surface is influenced by the chemical composition of the surface, the presence of roughness elements, and the surface energy. If a surface is hydrophilic, or "water-loving," the interactions between the surface and the water will dominate over the cohesive forces of the bulk fluid, and the water will spread over the surface. On the other hand, if a surface is hydrophobic, or "water-fearing," the surface will

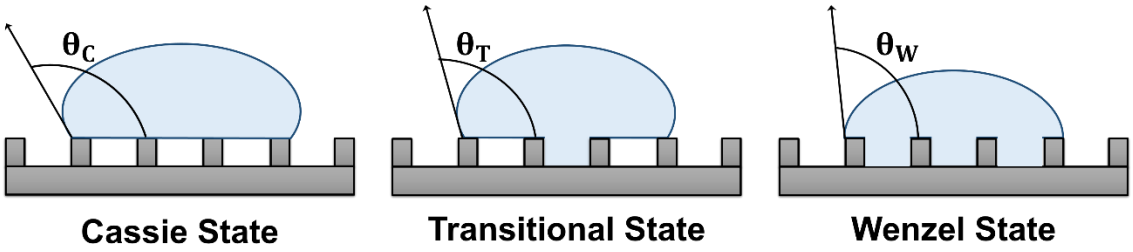


**Figure 1.4-1: Schematic of Cassie, transitional, and Wenzel wetting states, where $\theta_C$ is the Cassie state contact angle, $\theta_T$ is the transition state contact angle,and $\theta_W$ is the Wenzel state contact angle.**

actually repel the water molecules and the cohesive forces of the bulk fluid will dominate, resulting in the formation of water droplets on the surface.

The wettability of a surface may be best defined in terms of the measured contact angle ($\boldsymbol{\theta}$) between a drop of fluid and the surface, as shown in **Figure 1.4-1**. For a three-phase system consisting of water, air, and solid surface, the contact angle may be related to the solid-vapor ($\boldsymbol{\gamma_{SV}}$), solid-liquid ($\boldsymbol{\gamma_{LS}}$), and the liquid-vapor ($\boldsymbol{\gamma_{LV}}$) interfacial tensions, by the modified Young's equation (Rothstein, 2009):

$$\boldsymbol{\theta = \cos^{-1}\left(\frac{\gamma_{SV} - \gamma_{LS}}{\gamma_{LV}}\right)} \qquad \textbf{(1.4-1)}$$

A fluid is said to exhibit wetting behavior solid is $0 \leq \theta \leq 90°$. If the contact angle between the fluid and solid is $\boldsymbol{90° < \theta \leq 180°}$**,** then the fluid is said to exhibit non-wetting behavior (Voronov and Papavassiliou, 2008). if the measured contact angle between a drop of the fluid and a solid is $\boldsymbol{0 \leq \theta \leq 90°}$**.** If the contact angle between the fluid and solid is $\boldsymbol{90° < \theta \leq 180°}$**,** then the fluid is said to exhibit non-wetting behavior (Voronov and Papavassiliou, 2008).

In the presence of roughness elements, two distinct states of wetting, known as the Wenzel state and the Cassie state (**Figure 4-1**) may exist. In the

Wenzel state, water penetrates between the roughness elements (Rothstein, 2009). In the Cassie state, water droplets are suspended on top of the roughness elements, resulting in an air-water interface that is supported by the roughness (Dorrer and Rühe, 2007; Rothstein, 2009). If a maximum static pressure ($\mathbf{\Delta p_{max}}$) that can be supported by the air-water interface is exceeded, as described in **Equation 1.4-2** by the Young equation the system will revert to the Wenzel state (Dorrer and Rühe, 2007; Rothstein, 2009).

$$\mathbf{\Delta p_{max} = p_{water} - p_{air} = -\frac{2\gamma \cos \theta_A}{w}} \qquad \textbf{(1.4-2)}$$

where $\mathbf{p_{water}}$ and $\mathbf{p_{air}}$ are the pressure of the water and air, respectively, $\boldsymbol{\gamma}$ is the surface tension between the water and air, $\boldsymbol{\theta_A}$ is the advancing contact angle of the droplet, and $\mathbf{w}$ is the spacing between the roughness elements.

If the air-water surface tension is taken to be $\boldsymbol{\gamma = 0.0728\ kg/s^2}$ at 20˚C, and the distance between the posts is taken to be $\mathbf{w = 1\ \mu m}$, then the pressure difference needed to generate a change in θ by 1 degree from the flat meniscus case ($\boldsymbol{\theta = 90°}$) would be $\boldsymbol{\Delta p \approx 5{,}082\ kg/s^2}$.

*1.4.3. Surface Applications and Fabrication*

Future applications of SHSs will exploit the drag reducing, anti-adhesion, and self-cleaning characteristics of these surfaces. For instance, these surfaces may be used in anti-icing coatings for powerlines; in transparent and anti-reflective coatings, such as those used in eye glasses; in electronics and circuits to prevent water-corrosion; in separation processes, such as the removal of oil from water; and in fluidic drag reduction in both micro- and large scale systems (Voronov and Papavassiliou, 2008; Rothstein, 2009; Guo, Liu, and Su, 2011).

Numerous techniques for the fabrication of SHSs have been developed in recent years, such as wet chemical reaction, hydrothermal reaction, chemical vapor deposition, and plasma etching (Guo, Liu, and Su, 2011). **Table 1.4-1** summarizes the most recent methods and the substrates used in the creation of SHSs.

**Table 1.4-1: Surface fabrication methods and substrates.**

| Method | Substrates |
|---|---|
| Wet Chemical Reaction | Silicon wafer; copper; zinc; titanium; aluminum; steel |
| Hydrothermal Reaction | Silicon wafer; titanium; zinc |
| Electrochemical Deposition | Silicon wafer; copper; steel |
| Self-Assembly | Glass; silicon wafer; cotton |
| Layer-by-Layer | Glass; silicon wafer |
| Plasma Etching | Glass; silicon wafer; carbon nanotubes; polymer |
| Chemical Vapor Deposition | Carbon nanotubes; cotton |
| Sol-Gel | Cotton; silicon wafer |
| Polymerization Reaction | Cotton; silicon wafer; polymer; carbon nanotubes |

## 1.5. Nomenclature

Roman and Mixed Characters

| | |
|---|---|
| $\vec{\mathbf{a}}$ | Acceleration of element |
| $\mathbf{A}$ | Surface area |
| $\mathbf{C}$ | Courant number |
| $\mathbf{C_D}$ | Kinetic energy model constant |
| $\mathbf{C_{\varepsilon 1}}, \mathbf{C_{\varepsilon 2}}$ | Dissipation of turbulent kinetic energy constant ($C_{\varepsilon 1} = 1.44, C_{\varepsilon 2} = 1.92$) |
| $\mathbf{C_{\omega 1}}, \mathbf{C_{\omega 2}}$ | Specific dissipation rate constant ($C_{\omega 1} = C_{\varepsilon 1} - 1$, $C_{\omega 2} = C_{\varepsilon 2} - 1$) |
| $\mathbf{f}$ | Universal dimensionless function |
| $\vec{\mathbf{f}}$ | Acceleration due to body forces |
| $\vec{\mathbf{F}}$ | Net force acting on element |
| $\mathbf{k}$ | Turbulent kinetic energy |
| $\mathbf{l}$ | Characteristic length scale |
| $\mathbf{l}^*$ | Viscous length scale |
| $\mathbf{l_m}$ | Mixing length |
| $\mathbf{m}$ | Mass of element |
| $\vec{\mathbf{n}}$ | Unit normal vector |
| $\mathbf{N}$ | Number of grid nodes |
| $\mathbf{p}$ | Isotropic pressure |
| $\mathbf{p_{air}}$ | Air pressure |
| $\mathbf{p_{water}}$ | Water pressure |
| $\langle \mathbf{p} \rangle$ | Mean pressure |
| $\mathcal{P}$ | Rate of production of turbulent kinetic energy |
| $\mathbf{Re}$ | Reynolds number |

| | |
|---|---|
| $\mathbf{Re_\tau}$ | Friction Reynolds number |
| $\mathbf{t}$ | Time |
| $\mathbf{u^+}$ | Viscous velocity |
| $\mathbf{u_\tau}$ | Friction velocity |
| $\vec{\mathbf{u}}$ | Fluctuating velocity vector |
| $\langle\vec{\mathbf{u}}\vec{\mathbf{u}}\rangle$ | Velocity covariance (Reynolds stresses) |
| $\langle\vec{\mathbf{u}}\boldsymbol{\phi}\rangle$ | Scalar flux |
| $\vec{\mathbf{U}}$ | Flow velocity vector |
| $\langle\vec{\mathbf{U}}\rangle$ | Mean flow velocity vector |
| $\mathbf{V}$ | Control volume |
| $\mathbf{w}$ | Spacing between roughness elements |
| $\mathbf{y}$ | Distance from wall |
| $\mathbf{y^+}$ | Viscous length |

Greek Characters

| | |
|---|---|
| $\boldsymbol{\gamma}$ | Air-water surface tension |
| $\boldsymbol{\gamma_{LS}}$ | Liquid-solid interfacial tension |
| $\boldsymbol{\gamma_{LV}}$ | Liquid-vapor interfacial tension |
| $\boldsymbol{\gamma_{SV}}$ | Solid-vapor interfacial tension |
| $\boldsymbol{\Gamma_T}$ | Turbulent diffusivity |
| $\boldsymbol{\delta}$ | Kronecker delta |
| $\boldsymbol{\Delta p}$ | Pressure difference |
| $\boldsymbol{\Delta p_{max}}$ | Maximum pressure difference |
| $\boldsymbol{\Delta t}$ | Time step |
| $\boldsymbol{\Delta x}$ | Grid spacing |

| | |
|---|---|
| $\boldsymbol{\varepsilon}$ | Dissipation of turbulent kinetic energy |
| $\boldsymbol{\eta}$ | Kolmogorov length |
| $\boldsymbol{\theta}$ | Contact angle |
| $\boldsymbol{\theta_A}$ | Advancing contact angle |
| $\boldsymbol{\theta_C}$ | Cassie state contact angle |
| $\boldsymbol{\theta_T}$ | Transition state contact angle |
| $\boldsymbol{\theta_W}$ | Wenzel state contact angle |
| $\boldsymbol{\kappa}$ | Dilatational viscosity |
| $\boldsymbol{\Lambda_c}$ | Maximum eigenvalue of convective flux Jacobian |
| $\boldsymbol{\nu}$ | Fluid kinematic viscosity |
| $\boldsymbol{\nu_T}$ | Turbulent kinematic viscosity |
| $\boldsymbol{\rho}$ | Fluid density |
| $\boldsymbol{\sigma}$ | Courant-Friedrichs-Lewy number |
| $\boldsymbol{\sigma_\varepsilon}$ | Dissipation of turbulent kinetic energy constant ($\sigma_\varepsilon = 1.3$) |
| $\boldsymbol{\sigma_\omega}$ | Specific dissipation rate constant ($\sigma_\omega = 1.3$) |
| $\boldsymbol{\tau_w}$ | Wall shear stress |
| $\bar{\bar{\boldsymbol{\tau}}}$ | Viscous stress tensor |
| $\langle\boldsymbol{\phi}\rangle$ | Mean conserved passive scalar field |
| $\boldsymbol{\omega}$ | Specific dissipation rate |

## 1.6. References


ANSYS® Fluent® 12.5.1 Standard k-omega Model (2006).

ANSYS® Fluent® 12.9: Large eddy simulation (LES) model theory (2006).

Balasubramanian, Ashwin K., Adam C. Miller, and Othon K. Rediniotis. "Microstructured hydrophobic skin for hydrodynamic drag reduction." *AIAA journal* 42, no. 2 (2004): 411-414.

Bhushan, Bharat, and Yong Chae Jung. "Micro-and nanoscale characterization of hydrophobic and hydrophilic leaf surfaces." *Nanotechnology* 17, no. 11 (2006): 2758-2772.

Bhushan, Bharat, and Michael Nosonovsky. "The rose petal effect and the modes of superhydrophobicity." *Philosophical Transactions of the Royal Society of London A: Mathematical, Physical and Engineering Sciences* 368, no. 1929 (2010): 4713-4728.

Bird, R. Byron, Warren E. Stewart, and Edwin N. Lightfoot. *Transport Phenomena.* New York: John Wiley & Sons, 2002.

Blazek, Jiri. *Computational Fluid Dynamics: Principles and Applications*. Elsevier, 2001.

Cebeci, Tuncer. *Computational fluid dynamics for engineers: from panel to navier-stokes methods with computer programs*. Springer Science & Business Media, 2005.

Chung, T. J. *Computational fluid dynamics*. Cambridge university press, 2010.

Craik, Alex DD. "“Continuity and change”: representing mass conservation in fluid mechanics." *Archive for history of exact sciences* 67, no. 1 (2013): 43-80.

Daniello, Robert J., Nicholas E. Waterhouse, and Jonathan P. Rothstein. "Drag reduction in turbulent flows over superhydrophobic surfaces." *Physics of Fluids (1994-present)* 21, no. 8 (2009): 085103.

Darrigol, Olivier. "Between hydrodynamics and elasticity theory: The first five births of the Navier-Stokes equation." *Archive for history of exact sciences*56, no. 2 (2002): 95-150.

Dorrer, Christian, and Jürgen Rühe. "Condensation and wetting transitions on microstructured ultrahydrophobic surfaces." *Langmuir* 23, no. 7 (2007): 3820-3824.

Eymard, Robert, Thierry Gallouët, and Raphaèle Herbin. "Finite volume methods." *Handbook of Numerical Analysis* 7 (2000): 713-1018.

Fukagata, Koji, Nobuhide Kasagi, and Petros Koumoutsakos. "A theoretical prediction of friction drag reduction in turbulent flow by superhydrophobic surfaces." *Physics of Fluids (1994-present)* 18, no. 5 (2006): 051703.

Galdi, Giovanni P. *An Introduction to the Mathematical Theory of the Navier-Stokes Equations: Steady-State Problems*. Springer Science & Business Media, 2011.

Gatski, Thomas B., M. Yousuff Hussaini, and John L. Lumley. *Simulation and Modeling of Turbulent Flows*. Oxford University Press, 1996.

Groth, Clinton P.T., “Conservation equations for turbulent flows” (presentation, AER1310: Turbulence Modelling course, University of Toronto Institute for Aerospace Studies, 2015).

Guo, Zhiguang, Weimin Liu, and Bao-Lian Su. "Superhydrophobic surfaces: from natural to biomimetic to functional." *Journal of colloid and interface science*353, no. 2 (2011): 335-355.

Hoffmann, Klaus A., and Steve T. Chiang. "Computational fluid dynamics, Vol. 1." *Wichita, KS: Engineering Education System* (2000).

Hyväluoma, Jari, and Jens Harting. "Slip flow over structured surfaces with entrapped microbubbles." *Physical review letters* 100, no. 24 (2008): 246001.

Launder, Brian Edward, and Neil D. Sandham. *Closure Strategies for Turbulent and Transitional Flows*. Cambridge University Press, 2002.

Martell, Michael B., J. Blair Perot, and Jonathan P. Rothstein. "Direct numerical simulations of turbulent flows over superhydrophobic surfaces."*Journal of Fluid Mechanics* 620 (2009): 31-41.

Modi, Anirudh. "Direct numerical simulation of turbulent flows." *Available on Internet (www.anirudh.net/courses/ae525/paper.ps)* (1998).

Pletcher, Richard H., John C. Tannehill, and Dale Anderson. *Computational fluid mechanics and heat transfer*. CRC Press, 2012.

Pope, Stephen B. *Turbulent flows*. Cambridge University Press, 2000.

Rothstein, Jonathan P. "Slip on superhydrophobic surfaces." *Annual Review of Fluid Mechanics* 42 (2010): 89-109.

Roura, P., and J. Fort. "Comment on “Effects of the surface roughness on Sliding Angles of Water Droplets on Superhydrophobic Surfaces”." *Langmuir*18, no. 2 (2002): 566-569.

Tennekes, Hendrik, and John Leask Lumley. *A first course in turbulence*. MIT press, 1972.

Theodore, Louis. *Heat transfer applications for the practicing engineer*. Vol. 7. John Wiley & Sons, 2011.

Tu, Jiyuan, Guan Heng Yeoh, and Chaoqun Liu. Computational fluid dynamics: a practical approach. Butterworth-Heinemann, 2012.

Veldman, A. E. P. "Computational fluid dynamics." *Lecture Notes, University of Groningen, The Netherlands* (2001).

Voronov, Roman S., Dimitrios V. Papavassiliou, and Lloyd L. Lee. "Review of fluid slip over superhydrophobic surfaces and its dependence on the contact angle." *Industrial & Engineering Chemistry Research* 47, no. 8 (2008): 2455-2477.

Wendt, John, ed. *Computational fluid dynamics: an introduction*. Springer Science & Business Media, 2009.

Wilcox, D. C. "Turbulence modeling for CFD, 2nd ed. La Canada, California: DCW Industries." *Inc. VITA* (1994).

# Chapter 2: Superhydrophobic Micro-Roughness Models

Contents of this chapter have been reproduced from:

Heck, M.L. and Papavassiliou, D.V. “Effects of Hydrophobicity-Inducing Roughness on Micro-Flows.” *Chem. Eng. Commun.*, 200 (2013): 919-934

## 2.1. Introduction

SHSs have attracted increasing attention in the past decade for their potential for use in microfluidic devices and micro-electromechanical systems, as well as in applications involving self-cleaning and anticorrosive surfaces and coatings (Dorrer and Rühe, 2006; Eijkel, 2007; Whitesides and Stroock, 2001; Yang and Fang, 2005). A significant finding from recent studies of SHSs is that they can be used to passively induce hydrodynamic drag for both laminar and turbulent flows (Balasubramanian et al., 2004; Daniello et al., 2009; Lauga and Stone, 2003; Lauga et al, 2007; Muralidhar et al., 2011; Rothstein, 2010; Spencer et al., 2009; Tretheway and Meinhart, 2002; Voronov et al., 2007, 2008; Watanabe et al., 1999; Wilson, 2009), because a fluid can slip over the surface rather than stick to it. The resulting drag-reducing behavior has been confirmed at different extents in both large-scale conduits and in microfluidic channels (Gogte et al., 2005; Joseph et al., 2006; Lauga and Stone, 2003; Lauga et al., 2007; Ou et al., 2004). This finding is quite important for microfluidics applications, since a major challenge inherent in the growing area of micro-flow devices is the increase in pressure drop with decreasing microchannel dimensions (Cheng et al., 2009).

In this study, fluid dynamics simulations are used to identify the micro-roughness conditions, in conjunction with the wetting pattern, necessary to observe drag reduction, instead of drag increase, in different micro-channel geometries. The models of micro-channels used herein were specifically designed to observe changes in the flow around the roughness elements, as well as the pressure drop along the length of the micro-channel.

In order to identify conditions under which drag reduction may occur in micro-flows over hydrophobicity-inducing roughness elements, the results are obtained with a computational methodology similar to that of Hu et al. (2003) and are compared to results for surfaces that do not exhibit hydrophobic behavior. The geometry of the micro-channel, surface coverage of the micro-roughness elements, and wetting pattern of the fluid are then modified to reveal characteristic values related to the geometry that may result in drag reduction. Finally, a set of criteria for the prediction of the behavior of fluids in these systems that could be employed in the design and optimization of such surfaces is proposed.

## 2.2. Methodology

A periodically repeating microchannel of constant length, width, and height is simulated in this study (see **Figure 2-1**). The pressure drop ($\Delta \mathbf{p}/\Delta \mathbf{x}$) between the channel inlet and outlet for fully developed flow in a microchannel can be described analytically according to:

$$\frac{\Delta \mathbf{p}}{\Delta \mathbf{x}} = \frac{\mathbf{12}\boldsymbol{\mu}^{\mathbf{2}}\mathbf{Re}}{\boldsymbol{\rho}\mathbf{H}^{\mathbf{3}}} \qquad \textbf{(2-1)}$$

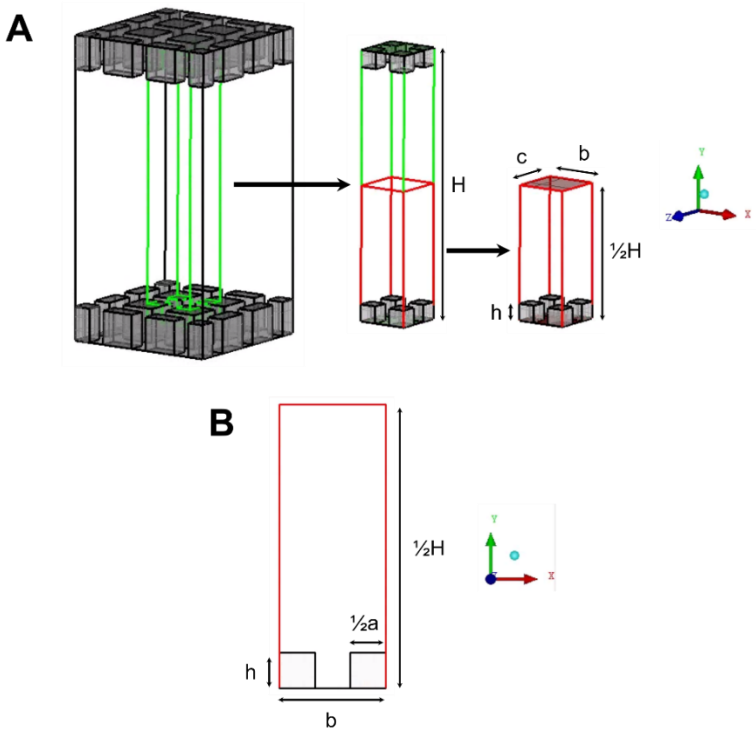


**Figure 2-1: Actual and simulated geometry for microchannel with roughness.**

(***A) Three-dimensional view of the microchannel depicting the minimum box size in the middle and the simulated minimum computational box on the right side; (B) Two-dimensional view at z = 0. The flow is periodic in the x-direction with periodic length of b and symmetry applied in the – direction with length c. Symmetry is also applied at y = ½H.***

where $\boldsymbol{\rho}$ is the fluid density, $\boldsymbol{\mu}$ is the fluid viscosity, $\mathbf{H}$ is the channel height and the Reynolds number ($\mathbf{Re}$) is defined as:

$$\mathbf{Re} = \frac{\boldsymbol{\rho}\bar{\mathbf{U}}\mathbf{H}}{\boldsymbol{\mu}} \qquad \textbf{(2-2)}$$

where $\bar{\mathbf{U}}$ is the average velocity of the fluid at the minimum cross section of the microchannel.

The fluid flow is fully developed and is considered to be laminar since all Reynolds numbers examined are between $\mathbf{0.001} \leq \mathbf{Re} \leq \mathbf{10}$.

The pressure drop can be non-dimensionalized using the following equations (Hu et al., 2003):

$$\mathbf{\Delta P = \frac{H \Delta p}{\mu u_0}} \qquad \textbf{(2-3)}$$

and

$$\mathbf{\Delta X = \frac{\Delta x}{H}} \qquad \textbf{(2-4)}$$

The dimensionless pressure gradient ($\mathbf{\Delta P / \Delta X}$) for a smooth microchannel would then be:

$$\mathbf{\frac{\Delta P}{\Delta X} = 12} \qquad \textbf{(2-5)}$$

All meshes are initially created using GAMBIT® (version 2.3.16). The roughness height ($\mathbf{h}$) is set to be 0, 0.1, 0.5, 1, and 2 μm. The channel height ($\mathbf{H}$) is held constant at 5 μm. The distances between the center points of the roughness elements, denoted as $\mathbf{b}$ and $\mathbf{c}$ in the $x-$ and $z-$ directions, respectively, also remain constant at 2 μm (see **Figure 5-1**). The width of the roughness ($\mathbf{a}$) is held constant at 1 μm. The fluid flowing through the microchannel was water with density $\boldsymbol{\rho = 1000\ kg/m \cdot s}$ and viscosity $\boldsymbol{\mu = 0.001003\ kg/m \cdot s}$.

ANSYS® Fluent® (version 12.0.16), a flow modeling simulation software, is used to simulate the flow of water over the roughness elements of interest in the microchannel. Fluent® is a finite volume-based computational fluid dynamics software, which allows for the discretization of the domain and the integration of governing equations around individual computational cells. This scheme results in the generation of linear algebraic equations for the unknown dependent

variables and ensures continuity of the velocity and pressure (Davies et al., 2006). The justification for using Fluent® rather than another software is:

(1) The finite volume scheme is locally and globally conservative.

(2) Fluent® is relatively easy to use and rather widely available for others wanting to duplicate or expand this work.

(3) Finite volume methods were used by Hu et al. (2003). Thus, the investigation of drag reduction in rough micro-channels conducted in this study is done with the same numerical scheme that resulted in drag increase in that prior study.

In an effort to efficiently model the system of interest, the microchannel is modeled in such a way as to take advantage of symmetry and periodicity in order to minimize the simulated part of the channel. Since the geometry of the microchannel is symmetrical, only the bottom half of the microchannel was modeled in all simulations. A periodic boundary condition is specified at both the mass flow inlet and outlet, which physically corresponds to fully developed flow in an infinitely long channel.

A first-order upwind discretization scheme is used at the initial stage of the simulation before switching to a second-order scheme in the final stages of the simulations. The convergence criteria for the residuals of the continuity equation and all momentum equations were set to $1 \times 10^{-6}$.

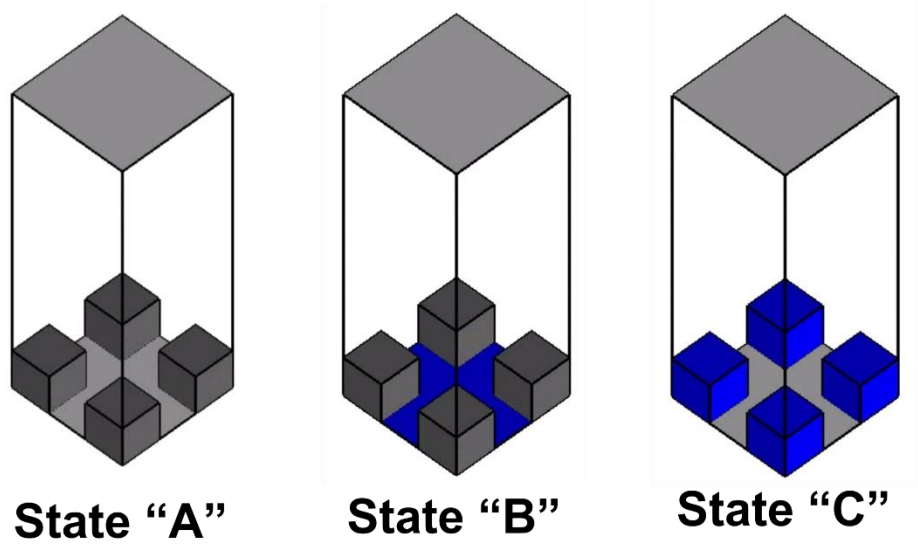


**Figure 2-2: Boundary conditions for no-slip/free-shear configurations in symmetric microchannels.**

***Gray coloring indicates areas with no-slip boundary conditions; blue coloring indicates areas with free-shear boundary conditions.***

The size of the computational domain in all cases is $2\ \mu m \times 2.5\ \mu m \times 2\ \mu m$ in the $x-$, $y-$, and $z-$ directions, respectively. **Figure 2-2** is a schematic of the modeled geometry. Several simulations are run in order to determine grid independence using hexahedral computational cells. Grid independence is obtained for computational cells with edges of 0.025 µm. Therefore, the procedure followed is to create the grid in Fluent, Inc.® GAMBIT™ with an interval size of 0.05 µm and then refine the grid in Fluent® up to a $y-$value equal to twice the roughness height for all values of $x$ and $z$, generating computational cells with edges equal to 0.025 µm. Refinement of the grid in regions near the roughness elements is acceptable because the areas of interest for this particular study are very close to the roughness elements in the micro-channels. For cases with $h = 0.1, 0.5,$ and $1\ \mu m$, the computational domain is refined in Fluent® in the regions

of $\mathbf{0 \leq x \leq 2\ \mu m,\ 0 \leq y \leq 2h}$, and $\mathbf{0 \leq z \leq 2\ \mu m}$. For the geometry with $\mathbf{h = 2\ \mu m}$, an interval size of 0.025 μm is used everywhere in the computational domain. For all cases considered, the roughness height, width, and depth are all divisible by the interval size.

The boundary conditions on the surfaces of the geometries depicted in **Figure 2-2** are modified according to the system that is modeled in each simulation, (i.e., depending on whether a wetted or a non-wetted state is simulated). When the fluid wets the space between the posts, the system may be classified as in the Wenzel state (Wenzel, 1936; Carbone and Mangialardi, 2005). Alternatively, when air is trapped between the posts such that the fluid does not fully wet the volume space between the roughness, the system may be classified as in the Cassie state (Cassie and Baxter, 1944).

In this study, the meniscus that forms between the surface roughness elements in the Cassie state is modeled as a flat free-shear boundary. This can be seen to be valid using the Young-Laplace equation (Ou and Rothstein, 2005; Truesdell et al., 2006; Joseph et al., 2006):

$$\Delta \mathbf{p} = \mathbf{4}\,{}^{\boldsymbol{\gamma}}\!/_{\mathbf{w}}\,\mathbf{cos}(\boldsymbol{\pi} - \boldsymbol{\theta}) \qquad \textbf{(2-5)}$$

where $\Delta\mathbf{p}$ is the hydrostatic pressure, $\boldsymbol{\gamma}$ is the surface tension, $\mathbf{w}$ is the distance between the micro-posts, and $\boldsymbol{\theta}$ is the contact angle. A hydrostatic pressure of a column of water with height 51.8 cm (much higher than $\mathrm{H} = 5\ \mu\mathrm{m}$) would be necessary for the curvature of the meniscus to change by 1°. The flat surface approximation is therefore valid for air-water systems and for the size of the

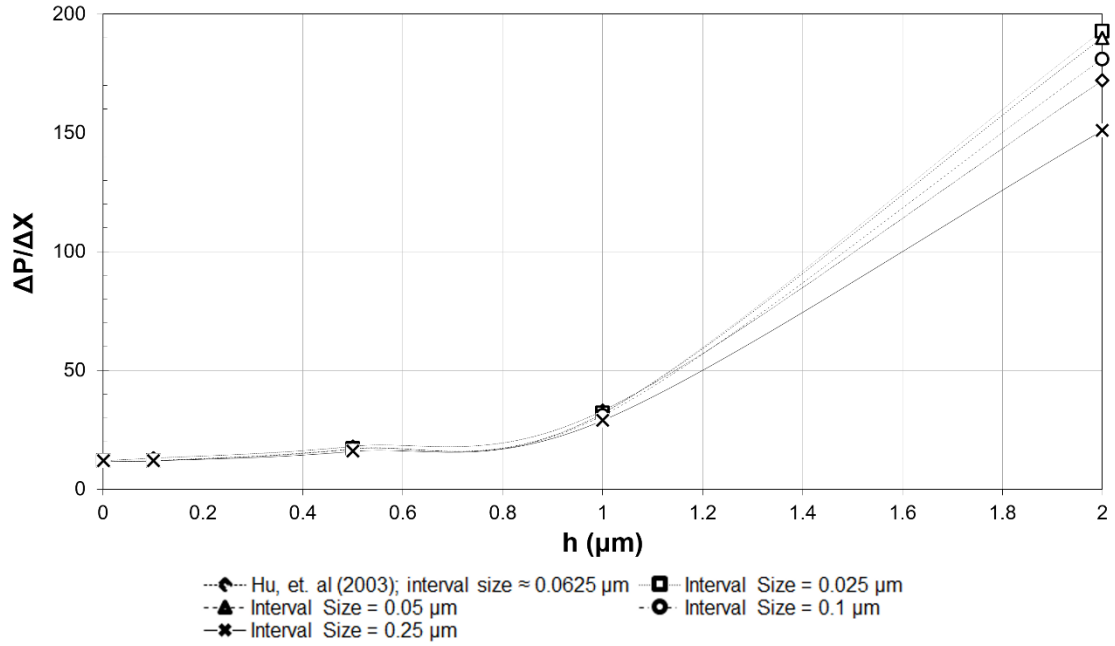


**Figure 2-3: Dependence of pressure gradient on roughness height for flow through a microchannel with dimensions a = 1.0 μm, b = c = 2.0 μm, and H = 5.0 μm.**

spacing between posts considered herein, as summarized in **Table 2-1** (Ou and Rothstein, 2005; Truesdell et al., 2006; Joseph et al., 2006).

Solutions obtained from the simulations of this study are compared in **Figure 2-3** with results from the prior study of Hu et al. (2003) for the same conditions ($\mathbf{0.001 \leq Re \leq 10}$). The results of this study are in qualitative and quantitative agreement with these prior results. Differences seen in the case of the highest posts between our results and the values obtained by Hu et al. (2003) are attributed to differences in grid resolution – this study utilizes a grid that is five times as fine. The pressure drop is noted to be a function of the geometry of the system. Thus, as the roughness height increases, the pressure drop and flow velocities also increase when $\mathbf{a}$, $\mathbf{b}$, $\mathbf{c}$, and $\mathbf{H}$ are held constant.

**Table 2-2: Boundary conditions specified in Gambit.**

| Plane/Surface Coordinates (in μm) | Boundary Condition |
|---|---|
| Plane thru x = 0; 0 ≤ y ≤ 2.5; 0 ≤ z ≤ 2 | Mass flow inlet |
| Plane thru y = 0; 0 ≤ x ≤ 2; 0 ≤ z ≤ 2 | Wall |
| Plane thru z = 0; 0 ≤ x ≤ 2; 0 ≤ y ≤ 2.5 | Symmetry |
| Plane thru x = 2; 0 ≤ y ≤ 2.5; 0 ≤ z ≤ 2 | Mass flow outlet |
| Plane thru y = 2.5; 0 ≤ x ≤ 2; 0 ≤ z ≤ 2 | Symmetry |
| Plane thru z = 2; 0 ≤ x ≤ 2; 0 ≤ y ≤ 2.5 | Symmetry |
| Roughness: tops, bottoms, & sides | Wall or Free Shear |

## 2.4. Results and Discussion

The data seen in **Figure 2-3** indicate that a function of h, H, a, and b exists to describe the dependence of pressure drop and velocity on the geometry of the system. In order to attain this relationship for the case of surfaces that behave as SHSs (i.e., cases that exhibit the Cassie or Wenzel wetting state), the boundary conditions at the fluid-solid interface are modified from the no-slip boundary condition. The wall boundary conditions were set as free of shear either on the walls of the cavities in the microchannel or on the floor of the microchannel.

Three states are depicted in **Figure 2-3**:

(1) **State A** represents a state of no-slip on all surfaces within the microchannel.

(2) **State B** represents a model with free shear on the surface of the microchannel between the micro-posts, but not on the roughness elements.

(3) **State C** represents a model with free shear on the sides of the roughness, as well as on the top of the roughness elements.

**State A** is a model of a Wenzel state, where the fluid wets the space between the micro-posts, corresponding to the geometry and boundary conditions simulated by Hu and colleagues (2003).

**State B** corresponds to cases with free shear at the floor of the channel due to chemistry effects or due to the presence of nanoscale roughness, as is

the case in the ‘‘rose-petal effect’’ (Bushan and Nosonovsky, 2010). This case may then be compared to the Cassie state, in which the water does not penetrate the space between the roughness (i.e. $\mathbf{h = 0}$), which is the state most often associated with superhydrophobic surfaces. The consideration of partial penetration of water into the space between roughness elements is important as it serves to indicate the maximum depth to which the water may penetrate before drag reduction is no longer observed.

**State C** is a modified model of a Wenzel state with posts that are hydrophobic due to chemistry, rather than due to the presence of trapped air.

### *2.4.1. Effect on Flow*

The differences in the flow fields resulting from each different micro-channel configuration are visualized using the flow path lines depicted in **Figures 2-4, 2-5,** and **2-6** for **States A**, **B**, and **C**, respectively. Locations at the middle of the micro-posts on the $\mathrm{x-y}$ plane and three different locations (at a quarter of micro-post height, at half the micro-post height, and at the top of the micro-posts) on the $\mathrm{x-z}$ plane are chosen to provide the characteristic features of the flow. The mass flow rate is equal to $\dot{\mathbf{m}} = \mathbf{1 \times 10^{-8}\ kg/s}$ and the Reynolds number is equal to $\mathbf{Re = 10}$ in all three cases. The case with a no-slip boundary condition applied at all fluid-solid interfaces indicates the typical profile for a lid-driven cavity flow in the $\mathrm{x-y}$ plane (**Figure 2-4A**). There is a circulation pattern with a single focal point, and the flow paths are affected up to about one micro-post height above the cavity. On the $\mathrm{x-z}$ plane, the fluid expands towards the open space

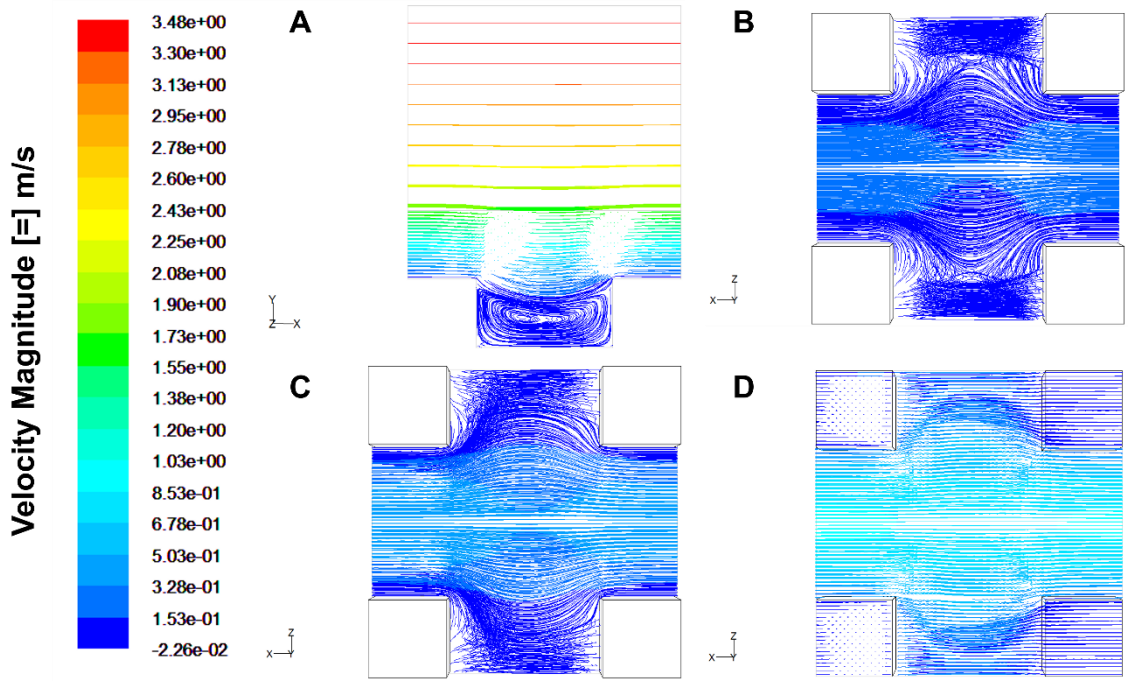


**Figure 2-4: Pathlines for the simulation of flow through a State A configuration with h = 0.5, a = 1.0 μm, b = c = 2.0 μm, and H = 5.0 μm.**

***(A) Pathlines on the z = 0 plane, i.e. at the half-point of the posts; (B) Pathlines at the y = 0.125 μm plane, i.e. at ¼ the height of the microposts; (C) Pathlines at the y = 0.25 μm plane, i.e. at ½ the height of the microposts; (D) Pathlines at the y = 0.5 μm plane, i.e. at the top of the microposts. The flow is in the x-direction and the color code is based on x-velocity in m/s.***

between the posts in the $z-$ direction as it passes the posts, as seen in **Figure 2-4B** through **Figure 2-4D.**

For **State B**, where there is free shear at the bottom of the space between the micro-posts, there is increased circulation appearing in the $x-y$ plane. Since there is slip at the bottom wall, the fluid can have a velocity on that surface (**Figure 2-5A**). On the $x-z$ plane, the path lines are, by and large, similar in shape to those for **State A** (**Figures 2-5B** through **Figure 2-5D**). It appears that the presence of the free shear boundary at the bottom of the microchannel does not change the flow at a distance larger than $\mathbf{y = 1/4\ h}$ from the bottom wall. The

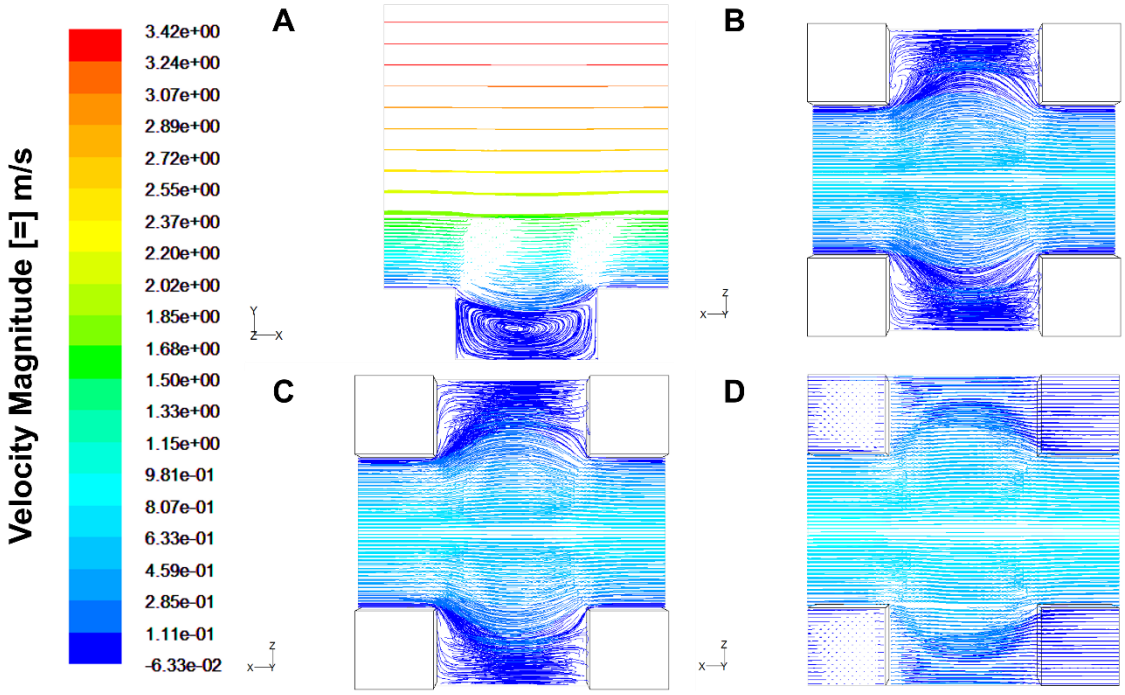


**Figure 2-5: Pathlines for the simulation of flow through a State B configuration with h = 0.5, a = 1.0 μm, b = c = 2.0 μm, and H = 5.0 μm.**

***(A) Pathlines on the z = 0 plane, i.e. at the half-point of the posts; (B) Pathlines at the y = 0.125 μm plane, i.e. at ¼ the height of the microposts; (C) Pathlines at the y = 0.25 μm plane, i.e. at ½ the height of the microposts; (D) Pathlines at the y = 0.5 μm plane, i.e. at the top of the microposts. The flow is in the x-direction.***

velocity in the $x-$direction for **State B** at $\mathbf{y = 1/4\,h}$ is slightly higher than that for **State A**.

For **State C**, the circulation pattern depicts two focal points in the $x-y$ plane, since the fluid can slip right after it flows above the micro-posts and drop into the cavity space, and then slip on its way towards the top of the next micro-post, as seen in **Figure 2-6A**. On the $x-z$ plane, the path lines are dramatically different than in **States A** and **B**. At $\mathbf{y = 1/4\,h}$, we can see a stagnation point at about half the distance between the posts (at point $\mathbf{x = 1/2\,b}$, $\mathbf{z = 1/4\,a}$, in **Figure 2-6B**). At the top of the micro-posts, the fluid barely expands in the $z-$

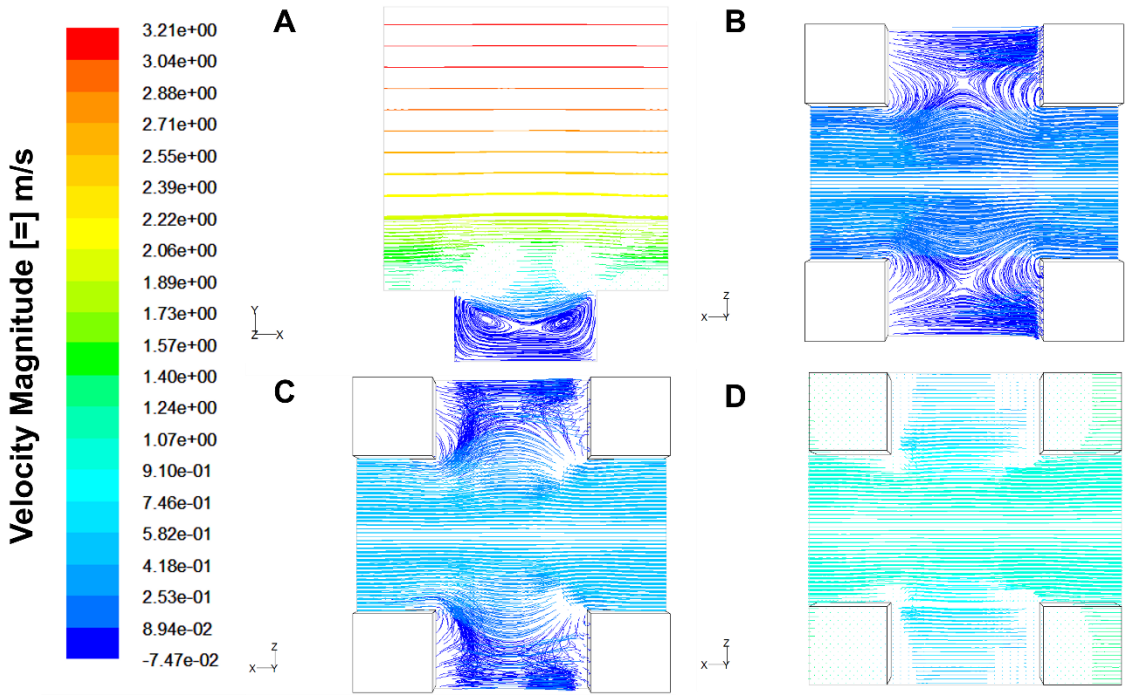


**Figure 2-6: Pathlines for the simulation of flow through a State C configuration with h = 0.5, a = 1.0 μm, b = c = 2.0 μm, and H = 5.0 μm.** ***(A) Pathlines on the z = 0 plane, i.e. at the half-point of the posts; (B) Pathlines at the y = 0.125 μm plane, i.e. at ¼ the height of the microposts; (C) Pathlines at the y = 0.25 μm plane, i.e. at ½ the height of the microposts; (D) Pathlines at the y = 0.5 μm plane, i.e. at the top of the microposts. The flow is in the x-direction.***

direction (**Figure 2-6D**) and looks as though it moves above the micro-posts without being affected by their presence.

*2.4.2. Effect on Pressure Drop*

Based on **Equation 2-5,** $\mathbf{1 - {}^{1}/_{12}\,(\Delta P/\Delta X) = 1}$ for a micro-channel with flat walls. The value of $\mathbf{1 - {}^{1}/_{12}\,(\Delta P/\Delta X)}$, which is the quantity appearing as the ordinate on **Figure 2-7**, is positive when a rough microchannel exhibits drag reduction relative to the flat wall case, and negative when a micro-channel exhibits drag increase relative to the flat wall case. The results of the simulations are graphically depicted in **Figure 2-7**. The presence of roughness, as expected,

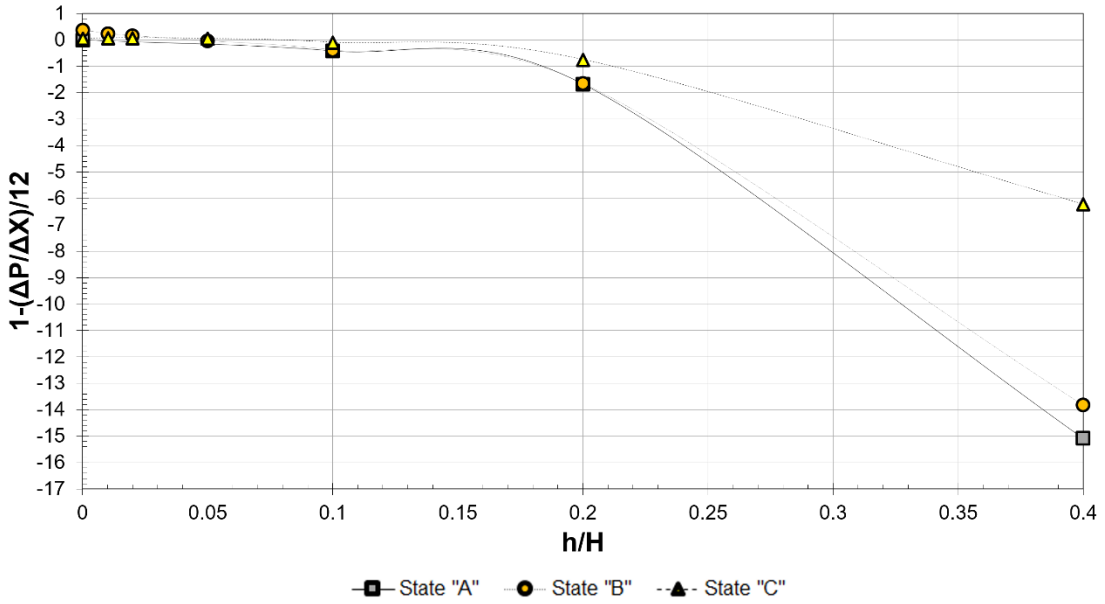


**Figure 2-7: Variance in pressure gradient with configuration (macro-view) for microchannels with dimensions a = 1.0 μm, b = c = 2.0 μm, and H = 5.0 μm.**

always increases drag for the no-slip microchannel (**State A**). The pressure drops for **States B** and **C**, however, are less than that for **State A**. Furthermore, when the $\mathbf{h/H < 0.045}$ for **State B** and $\mathbf{h/H < 0.080}$ for **State C** (**Figure 2-8**), the presence of roughness with free-shear boundary conditions may even result in drag reduction.

For **State B**, which is the case that models micro-roughness elements that have air trapped between them, the case of $\mathbf{h = 0}$ is a pure Cassie state, where the fluid does not wet the space between the posts at all and air is trapped between the posts creating a flat area with free shear. This would be a typical SHS, such as the lotus leaf. The cases of $\mathbf{h/H > 0}$ are models of systems in which the liquid partially wets the space between the posts (such as occurs in a transition from the Wenzel to Cassie state or vice versa; see **Figure 1.4-1**). Closer examination of this state could indicate that a critical value of the

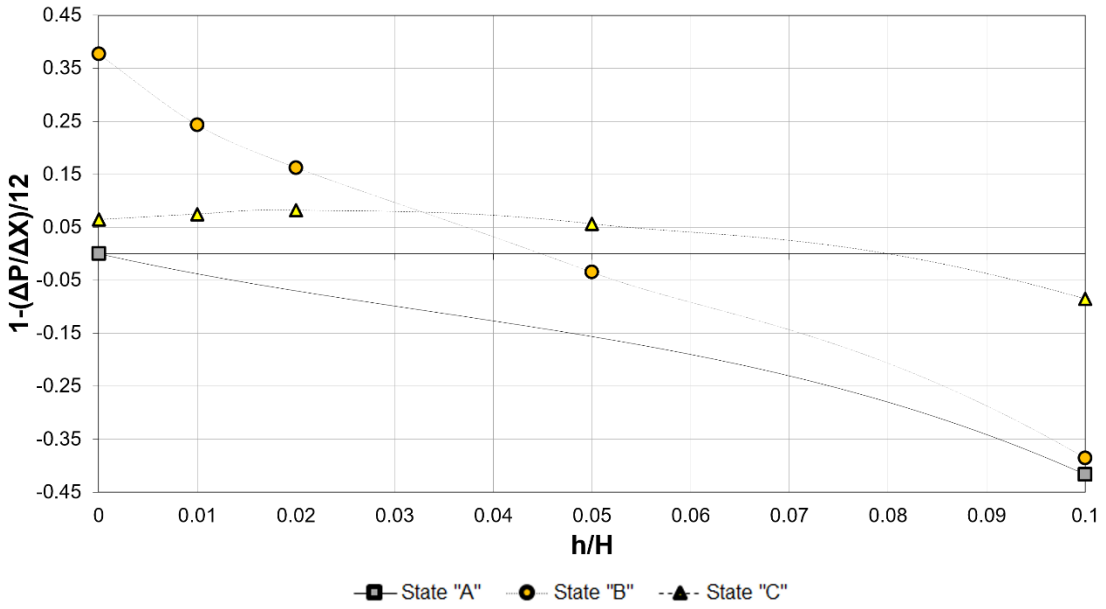


**Figure 2-8: Variance in pressure gradient with configuration (micro-view) for microchannels with dimensions a = 1.0 μm, b = c = 2.0 μm, and H = 5.0 μm.**

geometric characteristics of the micro-surface exists such that drag reduction relative to the base case (defined as the case of a microchannel with flat walls with no-slip boundary condition – **State A**) can be expected.

The geometric characteristics include the roughness to channel height ratio ($\mathbf{h/H}$), the width of the roughness ($\mathbf{a}$), and the roughness spacing ($\mathbf{b}$). After investigating several dimensionless combinations of the previously mentioned characteristics, two possibilities were identified as having a consistent, quantifiable trend or converging value between the dimensionless pressure drop and the characteristic value.

The first possibility is the ratio of the no-slip area to the total area over which the fluid flows ($\mathbf{A_{NS}/A_T}$), defined as:

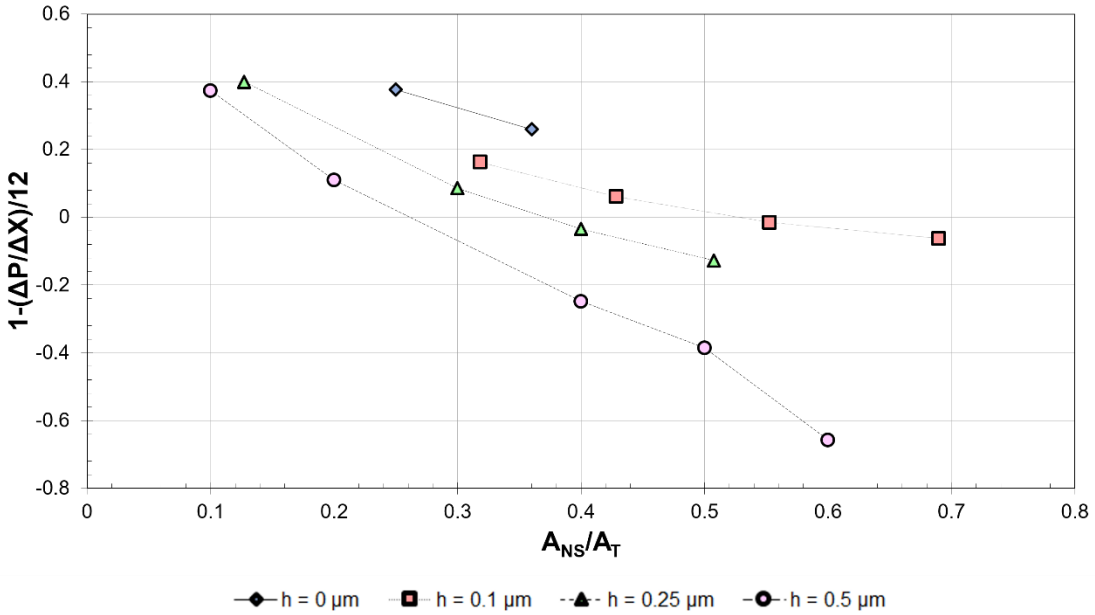


**Figure 2-9: Variance in pressure gradients with no-slip surface area for geometries with no-slip boundary conditions on the posts and free-shear boundary conditions in between the posts (State B).**

$$\frac{\mathbf{A_{NS}}}{\mathbf{A_T}} = \frac{\mathbf{a^2 + 4ah}}{\mathbf{b^2 + 4ah}} \qquad \textbf{(2-7)}$$

As presented in **Figure 2-9**, an approximately linear trend in which the pressure drop reduction increases with a decrease in the ratio of no-slip area to total area is observed. Furthermore, the slope of the line relating the reduction in pressure drop to the ratio of no-slip area to total area appears to increase with increasing roughness height, which indicates that a small change in this ratio of areas could result in a more dramatic change in pressure drop for taller roughness elements than for shorter ones.

The second possibility is the dimensionless hydraulic diameter ($\mathbf{D_h}$), as defined at the minimum cross section of the micro-channel:

$$\mathbf{D_h} = \frac{\mathbf{2}}{\mathbf{H}}\left(\frac{\mathbf{Hb - 2ah}}{\mathbf{a + 2h}}\right) \qquad \textbf{(2-9)}$$

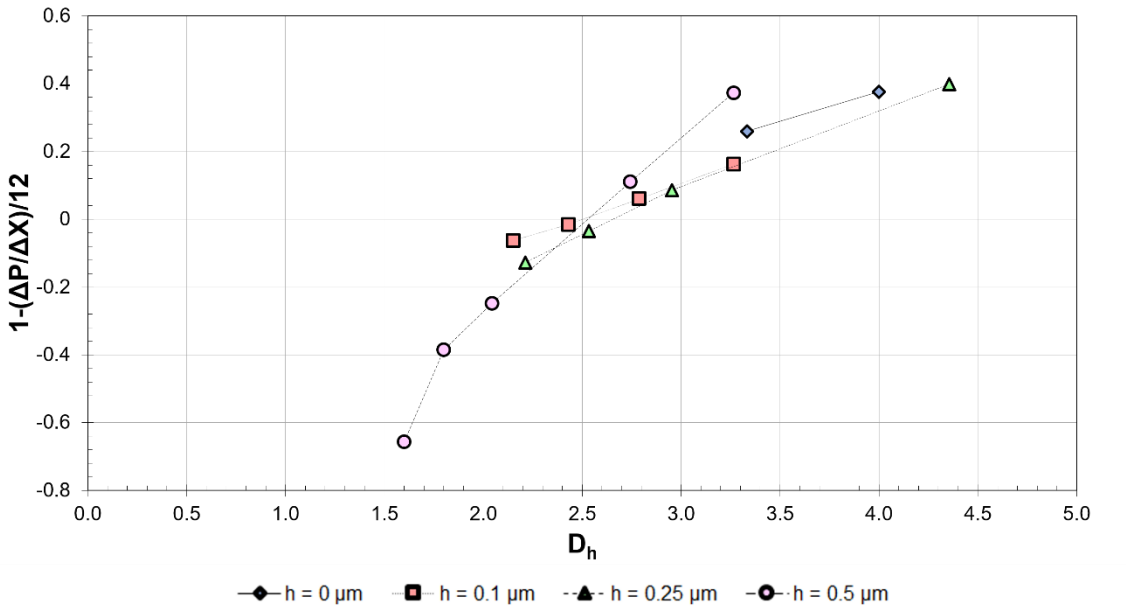


**Figure 2-10: Variance in pressure gradients with hydraulic diameter for geometries with no-slip boundary conditions on the posts and free-shear boundary conditions in between the posts (State B).**

In **Figure 2-10** the pressure drop as a function of $D_h$ using values of h and a, as described in **Table 2-2** for $\mathbf{Re = 10}$ and mass flow rate $\dot{\mathbf{m}} = \mathbf{1 \times 10^{-8}}\ \mathbf{kg/s}$ is presented. In these simulations, the space between the micro-posts is taken to be free of shear, while all other surfaces were taken to be no-slip. For all cases in which the roughness height is greater than 0, a pressure drop reduction is observed for values of the dimensionless hydraulic diameter larger than approximately 2.50. For cases in which there are roughness elements ($\mathbf{h > 0}$), this value of the dimensionless hydraulic diameter could prove to be a useful criterion for predicting the onset of drag reduction.

## 2.5. Summary and Conclusions

In this study, simulations are used to investigate drag reduction in micro-channels with surfaces that replicate SHSs. Consistent with previous studies and

intuition, when the fluid does not slip around or over the roughness elements, there is an increase in the pressure drop needed for the same amount of fluid to go through the micro-channel compared to the case of a channel with flat surfaces. When there is slip on the surface of the micro-posts or on the space between them, however, the pressure drop is smaller than the pressure drop for the case of a micro-channel with flat walls (Davies et al., 2006; Cheng et al., 2009; Rothstein, 2010).

When the pressure drop is plotted versus the dimensionless hydraulic diameter for **State B**, in which the water does not penetrate ($\mathbf{h = 0}$) or partially penetrates ($\mathbf{h > 0}$) the space between the roughness elements of a micro-channel with free shear surfaces between the micro-roughness, it is found that there may be a critical value above which drag reduction may be achieved for $\mathbf{Re = 10}$ and a mass flow rate $\mathbf{\dot{m} = 1 \times 10^{-8}\ kg/s}$ for the dimensions listed in **Table 2-2**. These results indicate that modifications of the surface of microdevices, which are enabled with advances in lithography and microfabrication, can lead to drag reduction for fluid flow and, in general, to ways of controlling fluid flow behavior.

**Table 2-3: Values of *h* and *a* used in simulations to vary $A_{NS}/A_T$ and $D_H$..**

| h (μm) | a (μm) |
|---|---|
| 0 | 1 |
| | 1.2 |
| 0.1 | 1.2 |
| | 1.4 |
| | 1.6 |
| 0.25 | 0.4 |
| | 0.8 |
| | 1 |
| | 1.2 |
| 0.5 | 0.2 |
| | 0.4 |
| | 0.8 |
| | 1 |
| | 1.2 |

## *2.6. Nomenclature*

### Roman Characters

| | |
|---|---|
| $\mathbf{a}$ | Width of the base of a square roughness element |
| $\mathbf{A_{NS}}$ | No-slip area of the bottom wall of the micro-channel |
| $\mathbf{A_T}$ | Total surface area of the bottom wall of the micro-channel |
| $\mathbf{b}$ | Distance between the centers of the roughness elements in the x-direction |
| $\mathbf{c}$ | Distance between the centers of the roughness elements in the z-direction |
| $\mathbf{D_h}$ | Hydraulic diameter of the micro-channel |
| $\mathbf{h}$ | Roughness element height |
| $\mathbf{H}$ | Channel height |
| $\dot{\mathbf{m}}$ | Mass flow rate |
| $\mathbf{Re}$ | Reynolds number |
| $\bar{\mathbf{U}}$ | Average velocity at the minimum cross section of the micro-channel |

### Greek Characters

| | |
|---|---|
| $\boldsymbol{\gamma}$ | Surface tension |
| $\boldsymbol{\Delta p}$ | Pressure change |
| $\boldsymbol{\Delta P}$ | Dimensionless pressure change |
| $\boldsymbol{\Delta x}$ | Distance between micro-channel inlet and outlet in the x-direction |
| $\boldsymbol{\Delta X}$ | Dimensionless distance between microchannel inlet and outlet in the *x*-direction |
| $\boldsymbol{\mu}$ | Fluid kinematic viscosity |
| $\boldsymbol{\rho}$ | Fluid density |

## *2.7. References*


Balasubramanian, Ashwin K., Adam C. Miller, and Othon K. Rediniotis. "Microstructured hydrophobic skin for hydrodynamic drag reduction." *AIAA journal* 42, no. 2 (2004): 411-414.

Barthlott, Wilhelm, and Christoph Neinhuis. "Purity of the sacred lotus, or escape from contamination in biological surfaces." *Planta* 202, no. 1 (1997): 1-8.

Bhushan, Bharat, and Michael Nosonovsky. "The rose petal effect and the modes of superhydrophobicity." *Philosophical Transactions of the Royal Society of London A: Mathematical, Physical and Engineering Sciences* 368, no. 1929 (2010): 4713-4728.

Bhushan, Bharat, and Yong Chae Jung. "Micro-and nanoscale characterization of hydrophobic and hydrophilic leaf surfaces." *Nanotechnology* 17, no. 11 (2006): 2758.

Carbone, G., and L. Mangialardi. "Hydrophobic properties of a wavy rough substrate." *The European Physical Journal E* 16, no. 1 (2005): 67-76.

Cassie, A. B. D., and S. Baxter. "Wettability of porous surfaces." *Transactions of the Faraday Society* 40 (1944): 546-551.

Cheng, Y. P., C. J. Teo, and B. C. Khoo. "Microchannel flows with superhydrophobic surfaces: Effects of Reynolds number and pattern width to channel height ratio." *Physics of Fluids (1994-present)* 21, no. 12 (2009): 122004.

Daniello, Robert J., Nicholas E. Waterhouse, and Jonathan P. Rothstein. "Drag reduction in turbulent flows over superhydrophobic surfaces." *Physics of Fluids (1994-present)* 21, no. 8 (2009): 085103.

Davies, J., D. Maynes, B. W. Webb, and B. Woolford. "Laminar flow in a microchannel with superhydrophobic walls exhibiting transverse ribs." *Physics of Fluids (1994-present)* 18, no. 8 (2006): 087110.

Dorrer, Christian, and Jürgen Rühe. "Advancing and receding motion of droplets on ultrahydrophobic post surfaces." *Langmuir* 22, no. 18 (2006): 7652-7657.

Eijkel, Jan. "Liquid slip in micro-and nanofluidics: recent research and its possible implications." *Lab on a Chip* 7, no. 3 (2007): 299-301.

Feng, Lin, Shuhong Li, Yingshun Li, Huanjun Li, Lingjuan Zhang, Jin Zhai, Yanlin Song, Biqian Liu, Lei Jiang, and Daoben Zhu. "Super-hydrophobic surfaces: from natural to artificial." *Advanced materials* 14, no. 24 (2002): 1857-1860.

Gamrat, Gabriel, Michel Favre-Marinet, S. Le Person, Roland Baviere, and Frédéric Ayela. "An experimental study and modelling of roughness effects on laminar flow in microchannels." *Journal of Fluid Mechanics* 594 (2008): 399-423.

Gao, Xuefeng, and Lei Jiang. "Biophysics: water-repellent legs of water striders." *Nature* 432, no. 7013 (2004): 36-36.

Gloss, Daniel, and Heinz Herwig. "Microchannel roughness effects: a close-up view." *Heat Transfer Engineering* 30, no. 1-2 (2009): 62-69.

Gogte, Salil, Peter Vorobieff, Richard Truesdell, Andrea Mammoli, Frank van Swol, Pratik Shah, and C. Jeffrey Brinker. "Effective slip on textured superhydrophobic surfaces." *Physics of fluids* 17, no. 5 (2005): 51701-51701.

Guo, Zhiguang, Weimin Liu, and Bao-Lian Su. "Superhydrophobic surfaces: from natural to biomimetic to functional." *Journal of colloid and interface science*353, no. 2 (2011): 335-355.

Heck, Margaret L., and Dimitrios V. Papavassiliou. "Effects of hydrophobicity-inducing roughness on micro-flows." *Chemical Engineering Communications* 200, no. 7 (2013): 919-934.

Hu, Yandong, Carsten Werner, and Dongqing Li. "Influence of three-dimensional roughness on pressure-driven flow through microchannels."*Journal of Fluids Engineering* 125, no. 5 (2003): 871-879.

Hyväluoma, Jari, and Jens Harting. "Slip flow over structured surfaces with entrapped microbubbles." *Physical review letters* 100, no. 24 (2008): 246001.

Joseph, Pierre, Cecile Cottin-Bizonne, J-M. Benoit, Christophe Ybert, Catherine Journet, Patrick Tabeling, and Lyderic Bocquet. "Slippage of water past superhydrophobic carbon nanotube forests in microchannels." *Physical review letters* 97, no. 15 (2006): 156104.

Kandlikar, Satish G. "Exploring Roughness Effect on Laminar Internal Flow–Are We Ready for Change?." *Nanoscale and Microscale Thermophysical Engineering* 12, no. 1 (2008): 61-82.

Lauga, Eric, and Howard A. Stone. "Effective slip in pressure-driven Stokes flow." *Journal of Fluid Mechanics* 489 (2003): 55-77.

Lauga, Eric, Michael Brenner, and Howard Stone. "Microfluidics: the no-slip boundary condition." In *Springer handbook of experimental fluid mechanics*, pp. 1219-1240. Springer Berlin Heidelberg, 2007.

Li, Xue-Mei, David Reinhoudt, and Mercedes Crego-Calama. "What do we need for a superhydrophobic surface? A review on the recent progress in the preparation of superhydrophobic surfaces." *Chemical Society Reviews* 36, no. 8 (2007): 1350-1368.

Majumder, Mainak, Nitin Chopra, Rodney Andrews, and Bruce J. Hinds. "Nanoscale hydrodynamics: enhanced flow in carbon nanotubes." *Nature* 438, no. 7064 (2005): 44-44.

Maynes, D., K. Jeffs, B. Woolford, and B. W. Webb. "Laminar flow in a microchannel with hydrophobic surface patterned microribs oriented parallel to the flow direction." *Physics of Fluids (1994-present)* 19, no. 9 (2007): 093603.

Miwa, Masashi, Akira Nakajima, Akira Fujishima, Kazuhito Hashimoto, and Toshiya Watanabe. "Effects of the surface roughness on sliding angles of water droplets on superhydrophobic surfaces." *Langmuir* 16, no. 13 (2000): 5754-5760.

Muralidhar, Pranesh, Nangelie Ferrer, Robert Daniello, and Jonathan P. Rothstein. "Influence of slip on the flow past superhydrophobic circular cylinders." *Journal of Fluid Mechanics* 680 (2011): 459-476.

Neinhuis, C., and W. Barthlott. "Characterization and distribution of water-repellent, self-cleaning plant surfaces." *Annals of Botany* 79, no. 6 (1997): 667-677.

Patankar, Neelesh A. "Vapor stabilizing substrates for superhydrophobicity and superslip." *Langmuir* 26, no. 11 (2010): 8783-8786.

Ou, Jia, Blair Perot, and Jonathan P. Rothstein. "Laminar drag reduction in microchannels using ultrahydrophobic surfaces." *Physics of Fluids (1994-present)* 16, no. 12 (2004): 4635-4643.

Ou, Jia, and Jonathan P. Rothstein. "Direct velocity measurements of the flow past drag-reducing ultrahydrophobic surfaces." *Physics of Fluids (1994-present)*17, no. 10 (2005): 103606.

Quéré, David, and Mathilde Reyssat. "Non-adhesive lotus and other hydrophobic materials." *Philosophical Transactions of the Royal Society of London A: Mathematical, Physical and Engineering Sciences* 366, no. 1870 (2008): 1539-1556.

Rothstein, Jonathan P. "Slip on superhydrophobic surfaces." *Annual Review of Fluid Mechanics* 42 (2010): 89-109.

Roura, P., and J. Fort. "Comment on “Effects of the surface roughness on Sliding Angles of Water Droplets on Superhydrophobic Surfaces”." *Langmuir* 18, no. 2 (2002): 566-569.

Sbragaglia, Mauro, and Andrea Prosperetti. "A note on the effective slip properties for microchannel flows with ultrahydrophobic surfaces." *Physics of Fluids (1994-present)* 19, no. 4 (2007): 043603.

Spencer, Nicholas B., Lloyd L. Lee, Ramkumar N. Parthasarathy, and Dimitrios V. Papavassiliou. "Turbulence structure for plane Poiseuille–Couette flow and implications for drag reduction over surfaces with slip." *The Canadian Journal of Chemical Engineering* 87, no. 1 (2009): 38-46.

# Chapter 3: Non-Newtonian Flow Models over Mixed Boundaries

## 3.1. Introduction

The wettability of surfaces is an important issue in many areas of engineering, including microfluidics and lubrication applications (Quéré, 2008). Superhydrophobic surfaces (SHSs) can significantly amplify hydrodynamic slip in both turbulent and laminar flows (Rothstein 2009; Belyaev and Viogradova 2010; Busse et al. 2013), enabling the motion of fluids in small, confined systems.

SHSs may have a particularly relevant impact in micro- and nano-systems, which have advanced significantly in recent years due to the increasingly apparent advantages of miniaturization and the development of novel microfabrication technologies (Shirtcliffe, Toon, and Roach, 2013). The low volume of fluid required for microfluidic systems has made these devices particularly useful for blood analysis, as well as other biological applications involving blood, proteins, antibodies, RNA, and DNA (Shirtcliffe and Roach, 2013). Systems involving non-Newtonian fluids, such as blood, polymer solutions, and suspensions, pose unique transport challenges that require efficient and effective solutions. In the case of non-Newtonian fluids, the viscosity of the fluid is often dependent on shear rate. The most common classes of non-Newtonian fluids are shear-thinning or pseudoplastic fluids, which exhibit a decrease in viscosity with increased shear stress, and shear-thickening or dilatant fluids, which exhibit an increase in viscosity with increased shear stress. **Figure 3-1** is an illustration of the general viscosity behavior of non-Newtonian and Newtonian fluids over a range of shear. It should be noted a surface that

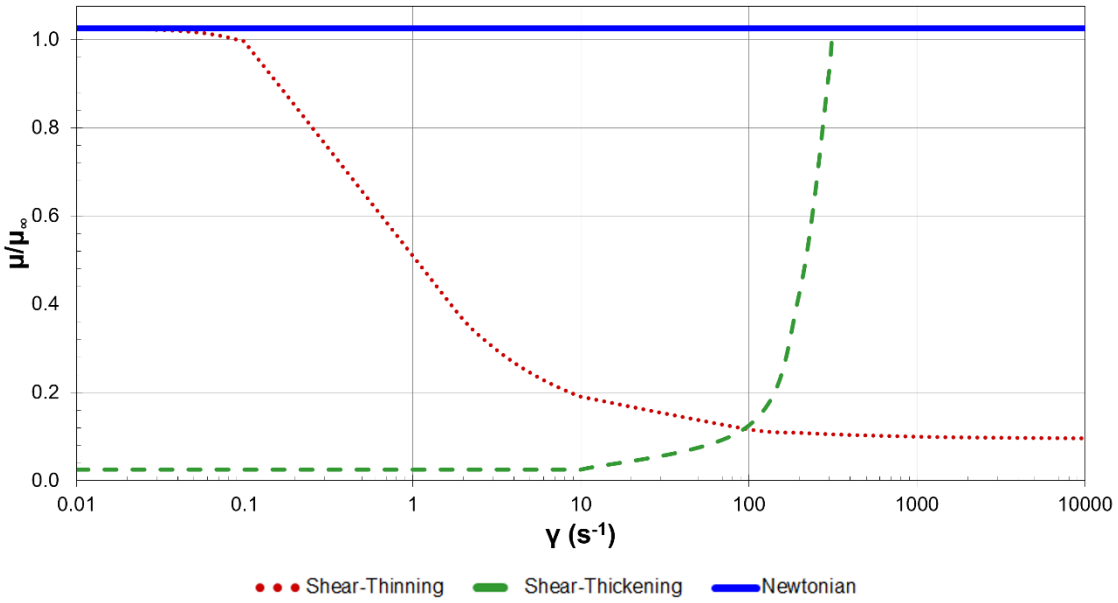


**Figure 3-1: Dependence of viscosity on shear rate for Newtonian and non-Newtonian fluids with constant densities.**

repels fluids other than water is more accurately called a solvophobic surface. The terms solvophobic and superhydrophobic are interchangeable in this study, however, irrespective of the type of fluid.

Microfluidic applications often face a problem with surface fouling, especially when such systems involve solutions with enzymes or proteins, as is often the case in medical and biological studies. While various strategies may be used to reduce adsorption of unwanted species on a surface, SHSs offer a unique solution by both reducing surface contamination and inducing self-cleaning properties of the surface (Shirtcliffe and Roach, 2013). Other confined systems, including porous materials and lubricating films, could also benefit significantly from the drag reduction and anti-fouling properties associated with the use of SHSs (Lee, Charrault, and Neto, 2014).

With these quite extraordinary properties in mind, this study aims to provide insight into the design of SHSs for use in microfluidic systems. The cases examined herein are flows over surfaces in the Cassie state, which are expected to behave as superhydrophobic surfaces in the sense that they would allow fluid to slip over them, even though the actual calculation of the contact angle of the fluids on these surfaces is not within the scope of this work. A description of current progress concerning SHSs is also presented and new details related to the effects of several flow and fluid properties on the effective slip over these surfaces are provided**.**

## 3.2. Background

As the potential for use of SHSs for drag reduction becomes more evident, the need for a predictive method for slip becomes more pressing. Several theoretical and numerical approaches have been used to describe the effective slip for various types of flow over SHSs (Lauga and Stone, 2003; Priezjev and Troian, 2006; Voronov, Papavassiliou, and Lee, 2008; Lee and Choi., 2008; Bazant and Vinogradova, 2009; Davis and Lauga, 2009; Feuillebois, Bazant, and Vinogradova, 2009; Belyaev and Vinogradova, 2010; Davis and Lauga, 2010; Ng and Wang, 2010; Busse et al., 2013). Among the most commonly adapted models are the generic scaling laws developed by Ybert et al. (2007), in which the effective slip length is related to characteristics of the SHS, including roughness length scale, depth, and solid fraction.

Numerous factors may influence the onset and magnitude of slip, including the type of fluid, the physical and chemical properties of the surface, the flow

regime, the geometry of the flow system, and ambient conditions, among many others (Sochi, 2011). Consequently, a rigorous analytical method to predict the occurrence and magnitude of slip has not yet been developed (Voronov, Papavassiliou, and Lee, 2008). It has even been suggested, based on molecular dynamics simulations, that slip can occur even in cases of flow over hydrophilic surfaces under certain conditions (Ho et al., 2011).

Most analytical and numerical studies exploring flow over SHSs have largely focused on Couette flow systems involving water. Although several groups have theorized that the effective slip length should be dependent on pressure gradients and fluid viscosity, relatively few have attempted to explore the quantitative differences that arise as a result of such dependencies (Watanabe, Udagawa, and Udagawa, 1999; Lauga and Stone, 2003; Ou, Perot, and Rothstein, 2004). An understanding of the effects of these factors on the effective slip over SHSs would greatly assist in the development of such surfaces for practical applications. The purpose of this study is to explore the dependence of slip on viscosity, pressure drop, and shear and to compare the observed effects in the context of generic scaling laws commonly used to describe flow over these surfaces.

Philip (1972) originally proposed the relationship shown below to describe the normalized effective slip for flow over a single ridge oriented parallel to the direction of flow:

$$\frac{\ell_{slip}}{L} = \frac{1}{\pi} \ln\left\{\sec\left[\frac{\pi}{2}(1 - \phi_{solid})\right]\right\} \quad \textbf{(3-1)}$$

where $\boldsymbol{\ell_{slip}}$ is the effective slip length, $\mathbf{L}$ is the distance between the center of the roughness elements in the span-wise direction, and $\boldsymbol{\phi_{solid}}$ is the solid/wetted fraction of the surface (i.e., the fraction of the surface that is wetted by the fluid and where the no-slip boundary condition is applicable).

Later, Ybert et al. (2007) proposed the relationship shown an empirical relationship for the normalized effective slip length:

$$\frac{\boldsymbol{\ell_{slip}}}{\mathbf{L}} = \frac{\mathbf{A}}{\sqrt{\boldsymbol{\phi_{solid}}}} - \mathbf{B} \qquad \textbf{(3-2)}$$

where $\mathbf{A}$ and $\mathbf{B}$ are numerical constants that depend on the geometry of the roughness elements (Ybert et al., 2007).

**Equation 3-2** can be used to find the constants $\mathbf{A}$ and $\mathbf{B}$ for flow over ridges oriented parallel to the flow and prior publications have presented estimates for the constants for flow over square and over circular posts (Ybert et al., 2007; Davis and Lauga, 2010; Ng and Wang, 2010).

For ridges aligned perpendicular to the direction of flow, the slip is described according to **Equation 3-3**, and would result in a smaller effective slip length than that for parallel ridges (Lauga and Stone, 2003; Belyaev and Vinogradova, 2010; Vinogradova and Belyaev, 2011; Asmolov and Vinogradova, 2012),

$$\frac{\boldsymbol{\ell_{slip}}}{\mathbf{L}} = \frac{\mathbf{1}}{\mathbf{2\pi}} \ln\left\{\sec\left[\frac{\boldsymbol{\pi}}{\mathbf{2}}(\mathbf{1} - \boldsymbol{\phi_{solid}})\right]\right\} \qquad \textbf{(3-3)}$$

The circular posts are close representations of the roughness elements of the lotus leaf, which has conical-shaped roughness elements. The ridges considered in this study are aligned parallel to the direction of flow. As was

previously noted, the slip for ridges aligned perpendicular to the flow would actually result in the lowest slip length, according to **Equation 3-3**. Since this is a well-established relationship (and results in poor drag reduction compared to other geometries), perpendicular ridges are not considered further in this study.

An effective fluid slip over a SHS leads to drag reduction in the flow, which is often defined based on the shear stresses or friction coefficients at the walls, as follows:

$$\mathbf{R_D = 1 - \frac{\tau_{w,SHS}}{\tau_{w,NS}} = \frac{f_{NS} - f_{SHS}}{f_{NS}}} \qquad \textbf{(3-4)}$$

where $\boldsymbol{\tau_{w,NS}}$ is the wall shear stress for the no-slip surface, $\boldsymbol{\tau_{w,SHS}}$ is the wall shear stress for the SHS, $\mathbf{f_{NS}}$ is the friction coefficient for flow over a no-slip surface, and $\mathbf{f_{SHS}}$ is the friction coefficient for flow over a superhydrophobic surface (Fukagata et al. 2006).

The following equation may be used to find the average velocity ($\boldsymbol{\bar{U}_{NS}}$) for Poiseuille flow in a channel with no-slip walls:

$$\mathbf{\bar{U}_{NS} = -\frac{1}{12\mu}\left(\frac{\partial p}{\partial x}\right)H^2} \qquad \textbf{(3-5)}$$

where $\boldsymbol{\mu}$ is the viscosity of the fluid, $\boldsymbol{\partial p/\partial x}$ is the stream-wise pressure gradient, and $\mathbf{H}$ is the channel height.

Newton's law of viscosity may be used to find the wall shear stress (Bird et al. 2005), in order to determine the terms appearing in **Equation 3-4**. For a Couette flow in a system with no slip walls, the average velocity may be found as (Bird et al. 2005):

$$\bar{U}_{NS} = \frac{1}{2} U_0 \tag{3-6}$$

where $U_0$ is the shearing wall velocity.

Similiarly, the average velocity for a Couette-Poiseuille flow would be (Bird et al. 2005):

$$\bar{U}_{NS} = -\frac{1}{12\mu}\left(\frac{\partial p}{\partial x}\right) H^2 + \frac{1}{2} U_0 \tag{3-7}$$

### 3.3. Surface Model

A micro-channel with dimensions of $10\ \mu m \times 190\ \mu m \times 10\ \mu m$ in the $x-$, $y-$, and $z-$ directions, respectively, is modeled as periodic in the span- and stream-wise directions. A channel height of 190 μm is a practical choice, since the effects of the SHS on the velocity profile are negligible at approximately 180 μm above the surface for the range of shear rates considered in this study. The dimensions associated with a micro-channel also facilitates full resolution of the computational domain around the edges of the microscopic roughness elements and utilizes geometries/meshes that have been validated in previous independent studies.

In three of the five cases explored in this study, the system of interest involves plane Couette flow with the top wall of the channel moving at a constant shearing velocity. These systems are defined as:

(1) **Case A** is a Newtonian fluid with a viscosity of $\mu = 9.95 \times 10^{-4}\ kg/m \cdot s$ and a density of $\rho = 1000\ kg/m^3$.

(2) **Case B** is A shear thinning (pseudo-plastic) fluid with a viscosity described by a Carreau generalized Newtonian viscosity model, described by **Equation 3-8**, and a density of $\boldsymbol{\rho = 1050\ kg/m^3}$..

(3) **Case C** is a shear thickening (dilatant) fluid with a power law generalized Newtonian viscosity model, given in **Equation 3-9,** and a density of $\boldsymbol{\rho = 1050\ kg/m^3}$**..**

In the remaining two cases, the systems are described as:

(4) **Case D** is a Poiseuille-Couette flow system with a top wall moving at velocity ($\mathbf{U_0}$), a prescribed mass flow rate ($\dot{\mathbf{m}}$), and a stream-wise pressure gradient ($\boldsymbol{\partial p/\partial x}$).

(5) **Case E** is a Poiseuille flow system with a prescribed mass flow rate ($\dot{\mathbf{m}}$) and a streamwise pressure gradient ($\boldsymbol{\partial p/\partial x}$).

The viscosity of the fluid following the Carreau model (**Case B**) is described by:

$$\frac{\mu - \mu_\infty}{\mu_0 - \mu_\infty} = [1 + (\lambda\dot{\gamma})^2]^{(n-1)/2} \qquad \textbf{(3-8)}$$

where $\boldsymbol{\mu}$ is the apparent viscosity and material constants $\boldsymbol{\mu_0 = 0.0639\ kg/m \cdot s}$, $\boldsymbol{\mu_\infty = 0.00445\ kg/m \cdot s}$, $\boldsymbol{\lambda = 3.31\ s}$, and $\boldsymbol{n = 0.35}$ (Johnston et al., 2004).

The viscosity of the shear thickening fluid (**Case C**) is given as:

$$\mu = k\dot{\gamma}^{n-1} \qquad \textbf{(3-9)}$$

with material constants $\mathbf{k = 0.001\ kg \cdot s^{n-2}/m}$ and $\mathbf{n = 3.0}$. **Equation 3-9** has a corresponding minimum viscosity limit of $\boldsymbol{\mu_{min} = 0.1\ kg/m \cdot s}$ and a maximum viscosity limit $\boldsymbol{\mu_{max} = 100\ kg/m \cdot s}$.

While the material constants for the shear-thinning and shear-thickening fluids are based on experimental data for blood and printer ink, as obtained by Tanner (2000) and Brown and Jaeger (2009), respectively, the behavior associated with these constants is not intended to represent or model specific fluids. Rather, the fluid properties are chosen to represent the desired fluid response to variations in shear rate, and are used for illustrative purposes to explore the effect of fluid properties on flow characteristics over mixed slip surfaces. The software package used in this study (ANSYS® Fluent®) offers several viscosity models for shear-thinning and shear-thickening fluids. The choice of the Carreau and power law models to describe the viscosity of the fluids is primarily based on both convenience and computational efficiency.

**Figure 3-2** illustrates the qualitative velocity profiles expected for flow in each of these cases. In all systems, the top wall of the channel is a regular, no-slip boundary condition wall.

A number of different surface topologies are considered for **Cases A**, **B**, and **D**. and more than 100 simulations are used to characterize the different cases described in **Table 3-1**. The bottom surfaces of the channels are modeled as regions of no-slip boundaries in the shapes of ridges, circular posts, and square posts, or circles corresponding to the surfaces shown in **Figure 3-2**. For

**Table 3-1: Summary of cases considered and parameters varied.**

| System | Fluid Model | Surface Topology | Solid Fraction $\phi_{solid}$ | Shearing Wall Velocity $U_0$ [=] $\frac{m}{s}$ | Pressure Gradient $\left\|\frac{\partial p}{\partial x}\right\|$ [=] $\frac{Pa}{m}$ |
|---|---|---|---|---|---|
| **Case A** and **Case B** | Newtonian (**Case A**) Shear-Thinning (**Case B**) | Circles | 0.16 | 0.0019<br>0.038<br>0.38<br>3.8 | |
| | | Ridges, Circles, Squares | 0.16, 0.25, 0.50 | 0.019<br>0.19<br>1.9 | |
| **Case C** | Shear-Thickening | Circles | 0.16 | 0.0019<br>0.038<br>0.38 | |
| | | | 0.16, 0.25, 0.50 | 0.019<br>0.19<br>1.9 | |
| **Case D** | Newtonian | Ridges, Circles, Squares | 0.16, 0.25, 0.50 | 0.019 | ~300 |
| **Case E** | Newtonain | Circles | 0.16, 0.25, 0.50 | 0 | ~3500<br>~35000<br>~350000 |

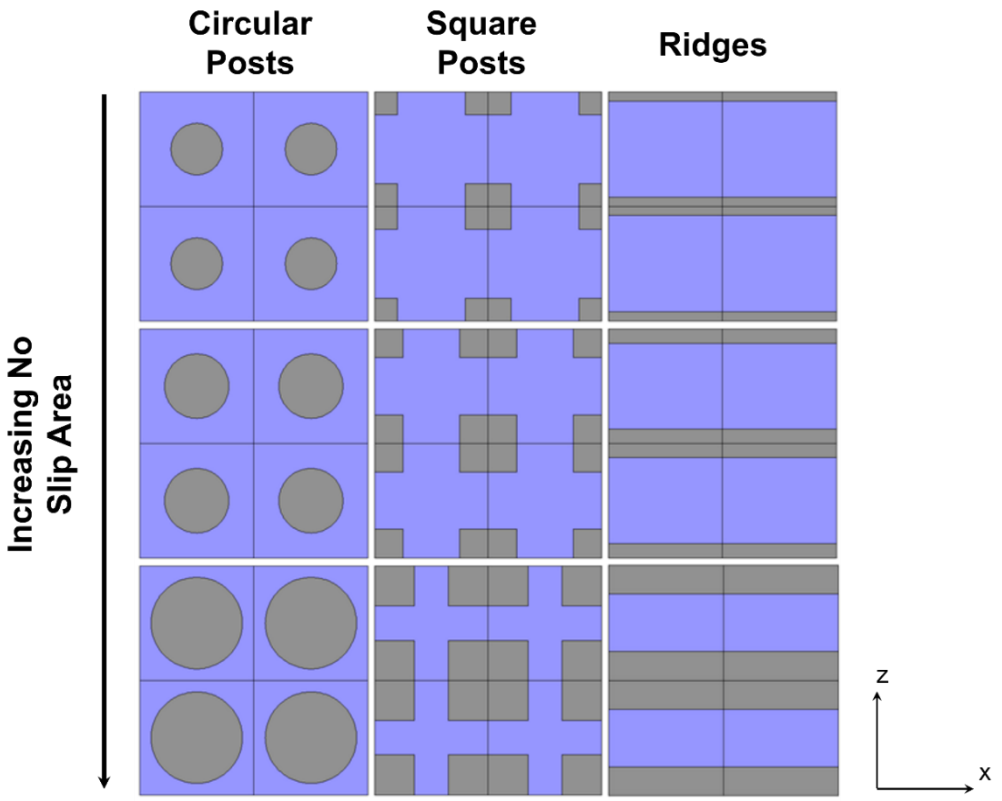


**Figure 3-2: No-slip/free-shear surface model configurations.**
***Gray coloring indicates areas with no-slip boundary conditions; blue coloring indicates areas with free-shear boundary conditions.***

**Cases C** and **E**, as well as select cases of **A** and **B**, only the surface with circular posts is considered.

One approach to the design of superhydrophobic surfaces is to use dimensions commonly found in nature, such as those of the lotus leaf. The diameter or width of the roughness on the lotus leaf may be seen to be on the order of 10 μm, with a similar magnitude of spacing between neighboring roughness elements (Voronov, Papavassiliou, and Lee, 2008). In keeping with these dimensions, the fractions of the area that are occupied by the roughness elements (i.e., the fractions where no-slip boundary conditions apply) considered in this study are 16%, 25%, and 50% of the total SHS area.

### 3.4. Methodology

All meshes are created using the ANSYS® ICEM CFD™ (version 14.0) meshing software. The grid is generated using three-dimensional blocking with node spacings no greater than 0.125 μm in the $x-$ and $z-$ directions. The error in velocity solutions obtained using this spacing, which results in meshes with approximately 350,000 nodes, is less than 4% when compared with those obtained using a mesh of nearly 500,000 nodes.

ANSYS® Fluent® (version 14.0), a flow modeling simulation software, is used to simulate the flow of the fluid over the roughness elements of interest in the microchannel. Fluent® is a finite volume-based computational fluid dynamics software, which allows for the discretization of the domain and the integration of governing equations around individual computational cells. This scheme results in the generation of linear algebraic equations for the unknown dependent variables and ensures continuity of the velocity and pressure (Davies et al. 2006).

A second order-upwind discretization scheme is used. Residuals for the continuity and momentum equations are required to be reduced by at least three orders of magnitude, while the value for the velocity magnitude on the wall modeled with the free shear boundary condition is monitored for convergence of within 1%. In general, convergence criteria of $1x10^{-7}$ for the continuity and momentum residuals are determined to be sufficient to reach a converged value for the slip velocity.

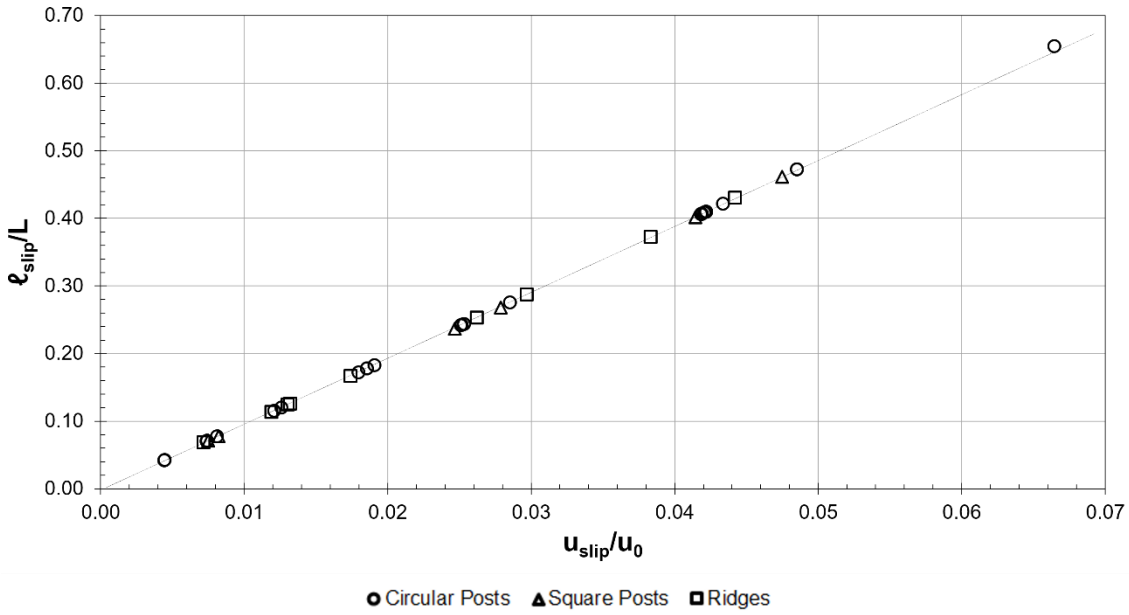


**Figure 3-3: Relationship between slip length and slip velocity for Newtonian flow over surfaces with 0.16% ≤ $\phi_{solid}$ ≤ 50%.**

### 3.5. Results and Discussion

The maximum difference between numerical results and analytical predictions is within 4%. Thus, the simulation methodology outlined in this study may be assumed to be valid and the results obtained should be accurate, especially close to the walls, where the differences between theoretical and computational results is a fraction of 1%.

**Figure 3-3** illustrates the relationship between the normalized effective slip length ($\boldsymbol{\ell_{slip}/L}$) and the normalized slip velocity $\left(\mathbf{U_{slip}/U_0}\right)$ for Newtonian and non-Newtonian flow over no-slip boundaries in the shapes of ridges, circular posts, and square posts at various shear rates. The data is observed to follow a line, the slope of which may be determined according to:

$$\frac{\boldsymbol{\ell_{slip}}}{\mathbf{L}} = \frac{\mathbf{H}}{\mathbf{L}}\left(\frac{\mathbf{U_{slip}}}{\mathbf{U_0 - U_{slip}}}\right) \qquad \textbf{(3-10)}$$

where $\mathbf{U_{slip}}$ is the slip velocity.

Thus, when the ratio of the slip velocity to the shearing velocity is much smaller than one, as in this study, the slope of the line observed in **Figure 3-4** is approximately equal to the channel height divided by the distance between the centers of the roughness elements. This relationship is useful for validation of the numerical results obtained for Couette flow and can also have a predictive value for design purposes, when either the slip velocity or the slip length can be estimated.

### *3.5.1. Effect of Roughness Shape*

Prior researchers have used both analytical methods and numerical regression to obtain estimates for the coefficients $\mathbf{A}$ and $\mathbf{B}$ appearing in **Equation 3-2** for several types of surface geometries (Ybert et al., 2007; Davis and Lauga, 2010; Ng and Wang, 2010). **Table 3-2** summarizes the results obtained from simulations for **Case A** and compares the values with those found by other groups for similar (though not necessarily identical) conditions. As is illustrated in **Figure 3-4**, the values for $\mathbf{A}$ and found in this study are within approximately 10% of published values.

**Figure 3-5** compares the dependence of the slip length on the solid fractions for **Case A** with a shearing wall velocity equal to $\mathbf{u_0 = 0.019\ m/s}$ with similar geometry-based models proposed by other groups. As the area of free shear is increased, however, the normalized effective slip length appears to become more sensitive to the geometry of the roughness on the surface, resulting in as much as a 13% difference.

**Table 3-2: Comparison of scaling law constants with previous models.**

| System | Surface Topology | Ybert (2007) Scaling Law Constants $\frac{\ell_{slip}}{L} = \frac{A}{\sqrt{\Phi_{solid}}} - B$ | |
|---|---|---|---|
| | | **A** | **B** |
| **Case A** $U_0 = 0.019\ m/s$ | Ridges ($R^2 = 0.997$) | 0.24 | 0.22 |
| | Circular posts ($R^2 = 1.00$) | 0.31 | 0.37 |
| | Square posts ($R^2 = 1.00$) | 0.30 | 0.36 |
| **Philip (1972)** | Ridges | 0.31 | 0.32 |
| **Davis and Lauga (2010)** | Circular posts | 0.33 | 0.42 |
| **Ybert et al. (2007)** | Square posts | 0.33 | 0.44 |

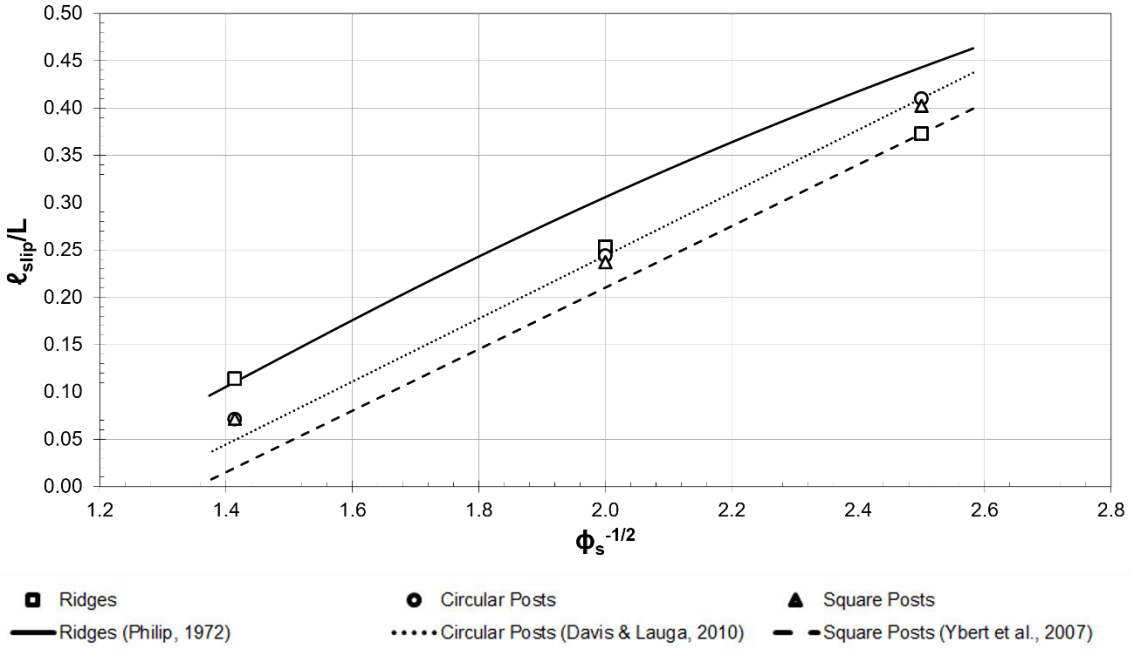


**Figure 3-4: Comparison of slips lengths obtained using numerical procedures and previously proposed models or Newtonian fluid= with constant densities in laminar flow ($U_0 = 0.019$ m/s).**

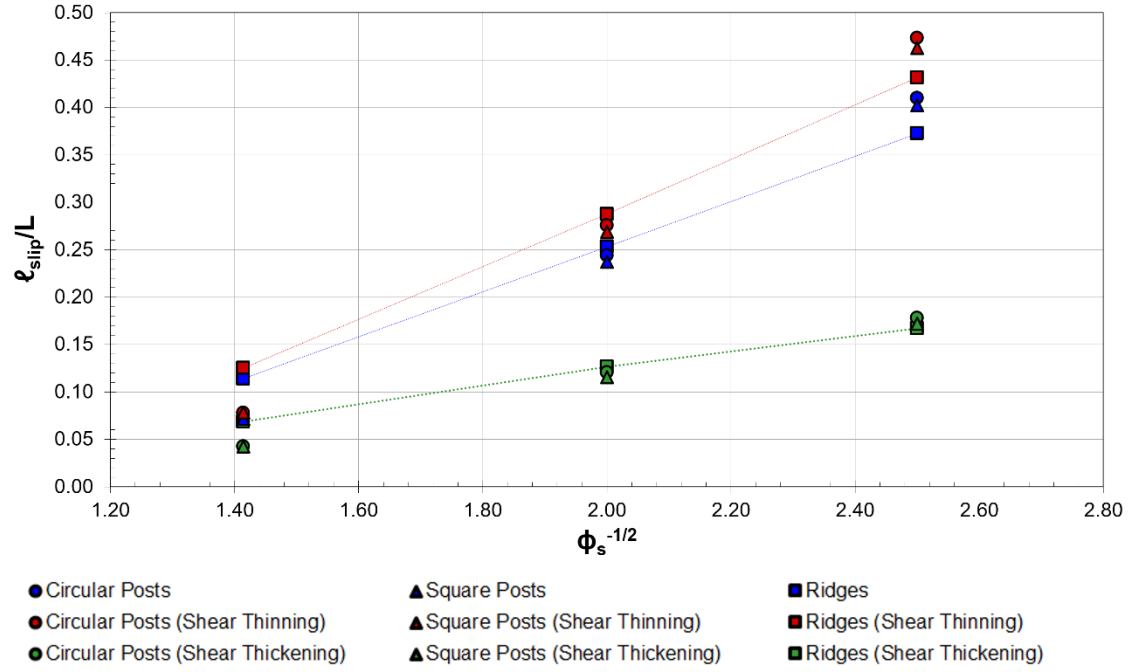


**Figure 3-5: Effect of roughness surface coverage on slip length for Newtonian, shear-thinning, and shear-thickening fluids with constant densities in laminar flow ($U_0 = 0.019$ m/s).**

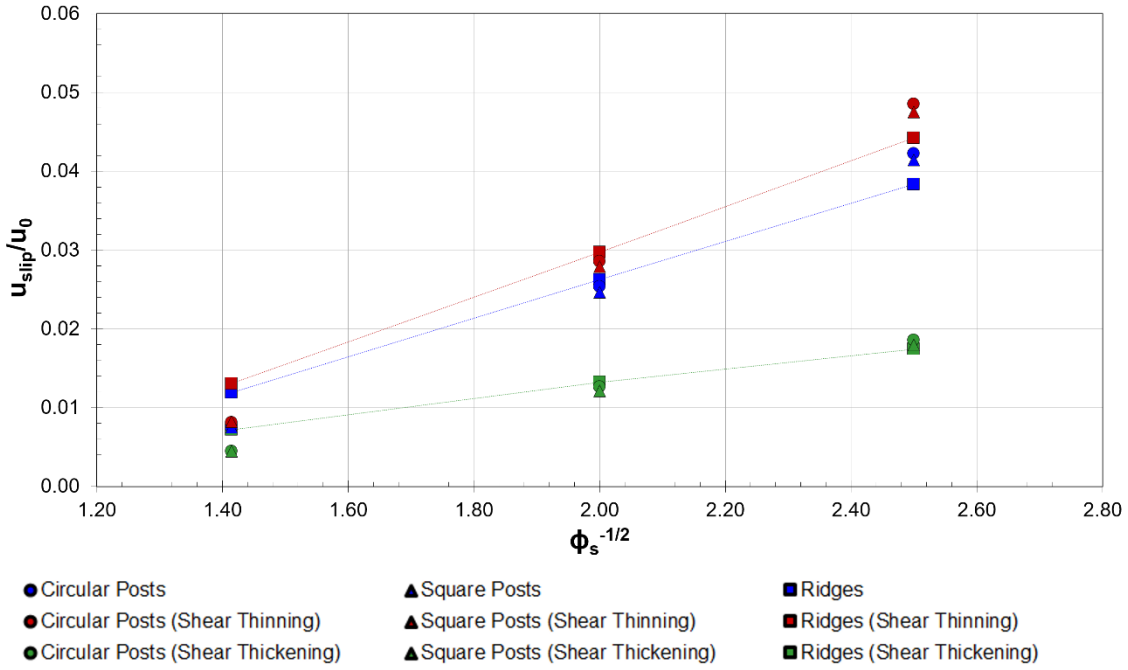


**Figure 3-6: Effect of roughness surface coverage on slip velocity for Newtonian, shear-thinning, and shear-thickening fluids with constant densities in laminar flow ($\mathbf{U_0 = 0.019\ m/s}$).**

**Figure 3-6** illustrates the relationship between slip velocity and surface solid fraction for **Case A** with a shearing wall velocity equal to $\mathbf{U_0 = 0.019\ m/s}$. **Figure 3-7** illustrates the relationship between drag reduction and surface solid fraction for **Case A** with a shearing wall velocity equal to $\mathbf{U_0 = 0.019\ m/s}$. The ridge-shaped roughness results in a reduction of drag that is 16% higher than that achieved with circular posts and almost 20% higher than that for square posts.

### *3.5.2. Effect of Viscosity*

As is summarized in **Table 3-3** and shown graphically in **Figure 3-7**, the viscosity of the fluid has a pronounced effect on slip length, as well as the scaling law constants $\mathbf{A}$ and $\mathbf{B}$ used In **Equation 3-2**. Both the shear-thinning and shear-

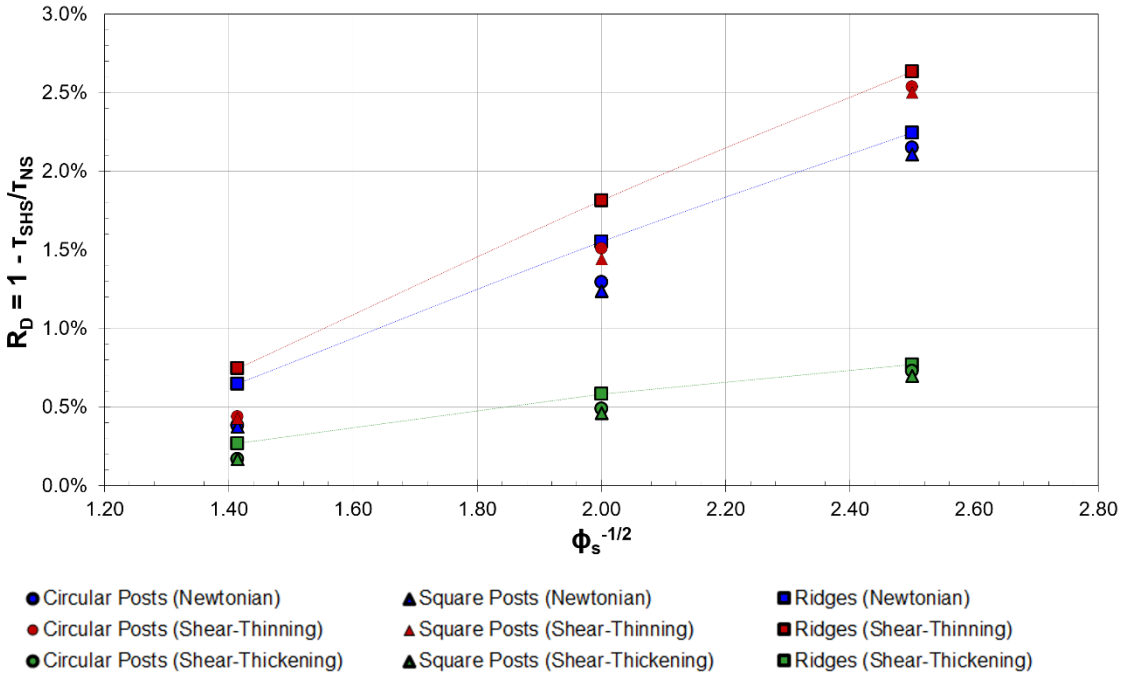


**Figure 3-7: Effect of roughness surface coverage on drag reduction for Newtonian, shear-thinning, and shear-thickening fluids with constant densities in laminar flow ($U_0 = 0.019\ m/s$).**

thickening fluids exhibit an increasing effective slip length with decreasing solid fraction, although the slip lengths for the shear-thinning and Newtonian fluids are significantly higher than those for the shear-thickening fluid. In fact, the highest effective slip length for the shear-thickening fluid modeled in this study is between 60%-70% lower than the highest effective slip lengths obtained for the Newtonian and shear-thinning fluids.

Viscosity also appears to result in substantial differences in the predicted slip velocity for the various surface topologies considered for **Cases A**, **B**, and **C** (**Figure 3-8**). The maximum drag reduction (**Figure 3-9**) achieved is approximately 3.3% and is observed for the flow of the shear-thinning fluid over the circular posts that cover 16% of the bottom surface area. This value is almost 60% higher than the drag reduction in the flow of a Newtonian fluid an d more

than 100% higher than that achieved in the flow of a shear-thickening fluid of the same surface.

### *3.5.3. Effect of Shear Rate*

The effective slip length for Couette flow of a Newtonian fluid should be independent of the shear rate at the low velocities used here (Martini et al., 2008). Numerical predictions show a negligible ($< \mathbf{2}\%$) decrease in the effective slip length for this type of flow.

Based on the definition of the slip length for Couette flow, the slip length would also be proportional to the ratio of the change in shear rate and slip velocity:

$$\frac{\boldsymbol{\ell}_{\mathbf{slip}}^{\mathbf{hi}}}{\boldsymbol{\ell}_{\mathbf{slip}}^{\mathbf{lo}}} \sim \frac{\dot{\boldsymbol{\gamma}}^{\mathbf{lo}}\mathbf{u}_{\mathbf{slip}}^{\mathbf{hi}}}{\dot{\boldsymbol{\gamma}}^{\mathbf{hi}}\mathbf{u}_{\mathbf{slip}}^{\mathbf{lo}}} \tag{3-11}$$

If a fairly intuitive assumption is made that states a change in shear rate would result in a proportional change in slip velocity, then a 10-fold increase in shear rate would be reasonably assumed to result in a 10-fold increase in the slip velocity, and the slip length would remain unchanged.

**Figure 3-10** plots of the influence of shear rate on the effective slip length for the Newtonian and non-Newtonian fluids (**Cases A**, **B**, and **C**). Because the fluid examined in **Case B** exhibits shear-thinning behavior, the difference observed between **Cases A** and **B** should become less noticeable with increasing shear. At low shear rates, there is an approximate 12% difference in the predicted effective slip length for water and the shear-thinning fluid, while at higher shear rates, the difference decreases to less than 2%.

**Table 3-3: Scaling law constants for Cases A, B, and C**

| System | Surface Topology | Ybert (2007) Scaling Law Constants $\frac{\ell_{slip}}{L} = \frac{A}{\sqrt{\Phi_{solid}}} - B$ | |
|---|---|---|---|
| | | **A** | **B** |
| **Case A** *(Newtonian)* | Ridges | 0.24 | 0.22 |
| | Circular posts | 0.31 | 0.37 |
| | Square posts | 0.30 | 0.36 |
| **Case B** *(Shear-Thinning)* | Ridges | 0.28 | 0.27 |
| | Circular posts | 0.36 | 0.44 |
| | Square posts | 0.35 | 0.43 |
| **Case C** *(Shear-Thickening)* | Ridges | 0.091 | 0.058 |
| | Circular posts | 0.12 | 0.13 |
| | Square posts | 0.12 | 0.13 |

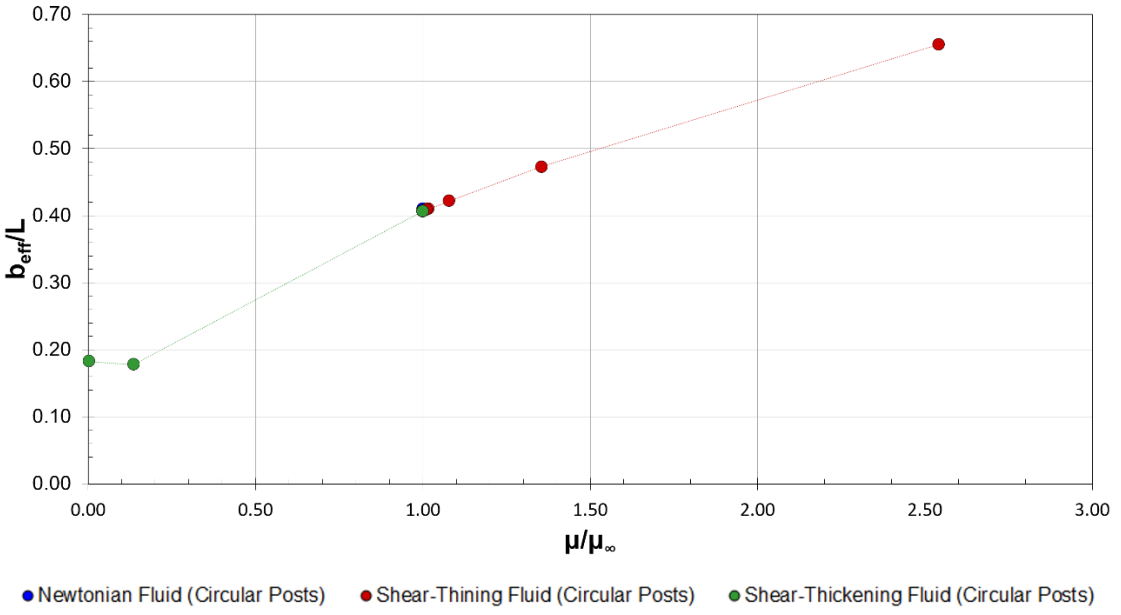


**Figure 3-8: Effect of viscosity on slip length for Newtonian, shear-thinning, and shear-thickening fluids with constant densities in flow over circular no-slip boundaries ($\phi_{solid} = 16\%$).**

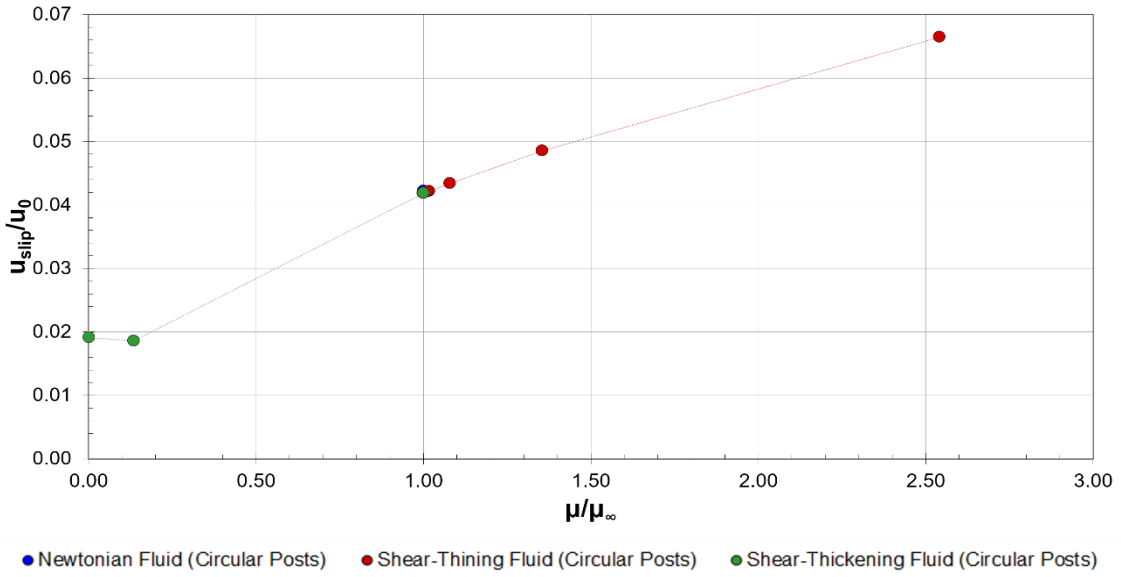


**Figure 3-9: Effect of viscosity of slip velocity for Newtonian, shear-thinning, and shear-thickening fluids with constant densities in flow over circular no-slip boundaries ($\phi_{solid} = 16\%$).**

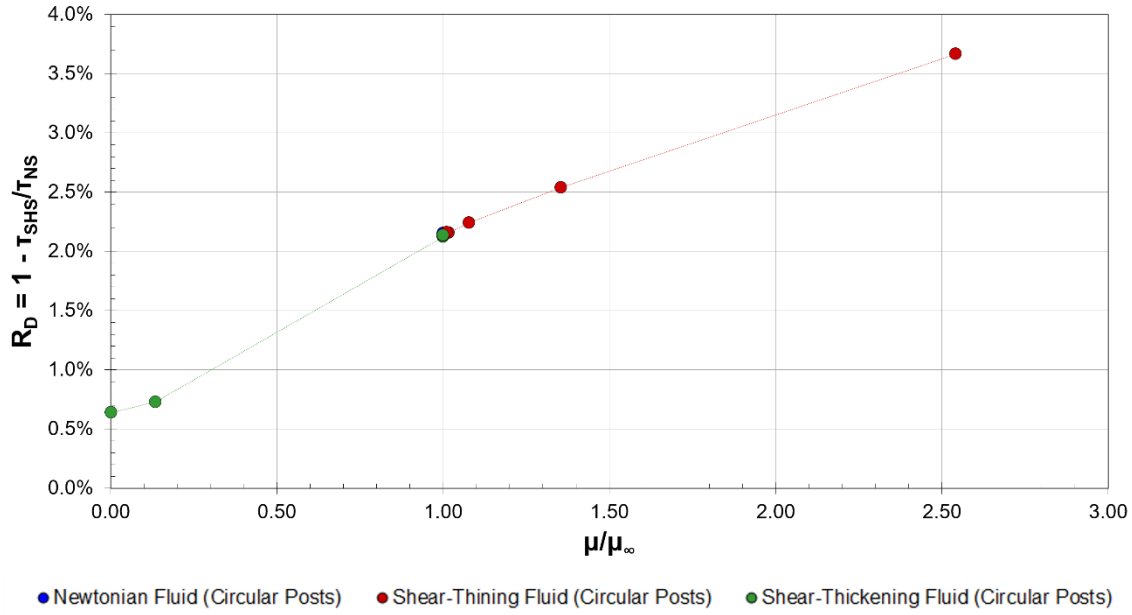


**Figure 3-10: Effect of viscosity drag reduction for Newtonian, shear-thinning, and shear-thickening fluids with constant densities in flow over circular no-slip boundaries ($\phi_{solid} = 16\%$).**

The shear-thickening fluid exhibits dramatically different behavior than the Newtonian and shear-thinning fluids with increasing shear rate. As may be seen in **Figure 3-11**, the slip velocity actually increases with increasing shear rate for the shear-thickening fluid at low to moderate shear rates.

The drag reduction achieved for **Cases A**, **B**, and **C** as a function of shear rate is displayed in **Figure 3-12**. At low to moderate shear, the drag reduction for the Newtonian (**Case A**) and shear-thinning fluids (**Case B**) decreases with increasing shear rate, while the drag reduction for the shear-thickening fluid (**Case C**) increases with increasing shear rate (**Figure 3-13**).

### 3.6. Summary

At high no-slip coverage ($\phi_{solid} \geq 50\%$), the effect of the shape of the roughness elements appears to be negligible. This behavior may be due to the

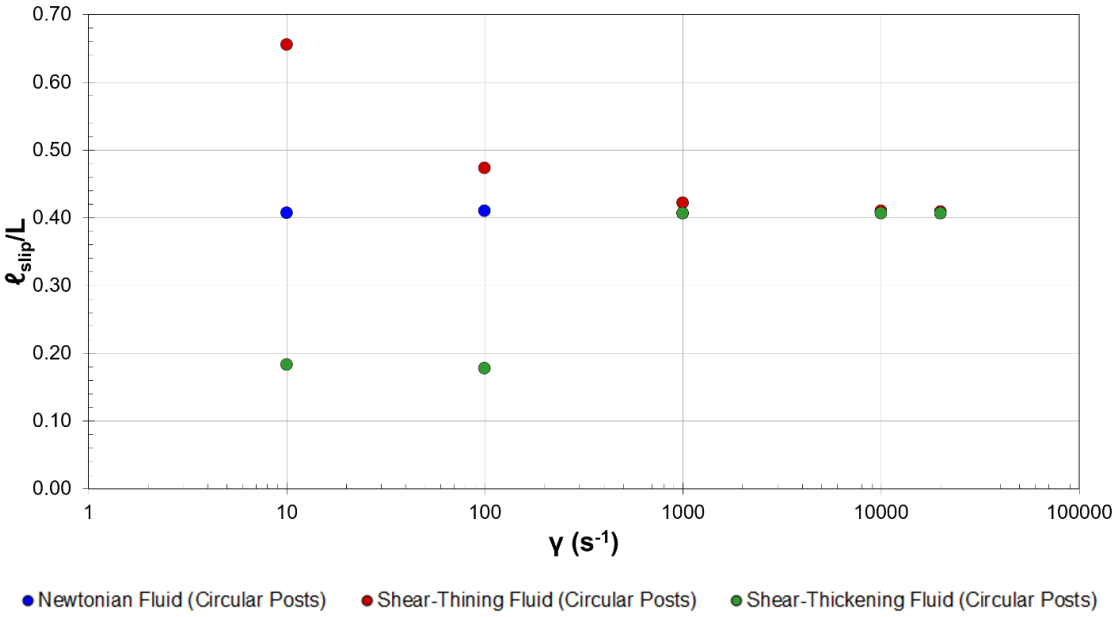


**Figure 3-11: Effect of shear on slip length for Newtonian, shear-thinning, and shear-thickening fluids with constant densities in flow over circular no-slip boundaries ($\boldsymbol{\phi_{solid} = 16\%}$).**

fact that a 50% solid coverage is the point at which the effects of the no-slip and the free-shear portions of the surface are effectively balanced and, thus, the effective slip length should be relatively independent of the surface roughness geometry. While not considered in this study, the effect of the free shear area for solid coverage much greater than 50% may be dwarfed by the effect of the no-slip area until the effective slip length would be equal to 0 when $\boldsymbol{\phi_{solid}^{-1/2} = 1.0}$.

The viscosity of the fluid flowing over the modeled SHS appears to have a significant effect on the effective slip length, slip velocity, and drag reduction. The effective slip lengths, velocities, and drag reduction for the non-Newtonian fluids appear to follow a qualitative trend similar to that of the viscosity. This behavior is consistent with the behavior of the models describing the dependence of the non-Newtonian viscosities on shear rate (see **Figure 3-1**). A 45% difference in

the predicted values of slip lengths for Newtonian and shear-thinning fluids and an 80% difference in the predicted values of slip lengths for Newtonian and shear-thickening fluids, is observed at the lowest shear rate considered ($10\ s^{-1}$). This difference is found to decrease with increasing shear. At $20{,}000\ s^{-1}$, the differences in the predicted slip lengths between the fluids are less than 4%. Thus, the difference in the obtainable slip for flow involving both Newtonian and non-Newtonian fluids at large shear rates is likely negligible. The effect of non-Newtonian rheological behavior, however, can be appreciable at low shear rates and may result in significantly different effective slip lengths, slip velocities, and maximum drag reduction.

As is expected (and validated by numerical predictions), the slip length should be independent of shear rate for laminar Couette flow of a Newtonian fluid. The shear-thinning and shear-thickening fluids considered in this study do show dependence, however, of the effective slip length on the shear rate at low to moderate shear (less than 500 $s^{-1}$).

The use of SHSs with non-Newtonian fluids has not previously been studied extensively. This study explores, in depth, achievable slip and drag reduction in SH systems in laminar, non-Newtonian (as well as Newtonian) flow. The findings of this study may be relevant in the development of biomedical and microfluidic devices and could result in improved models for the prediction of drag reduction in flow over these surfaces.

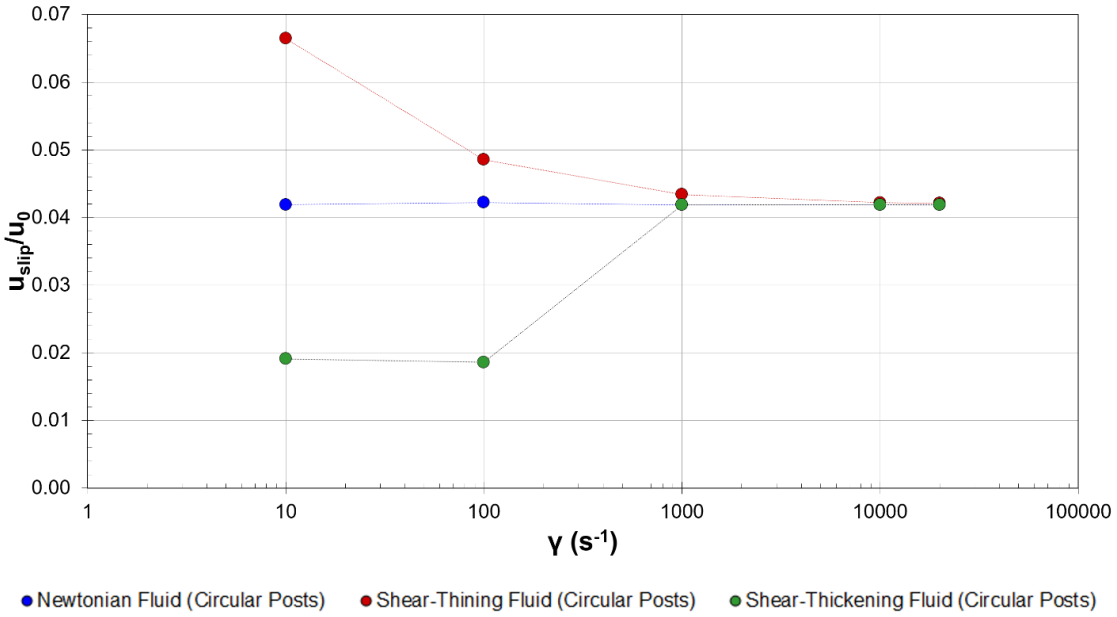


**Figure 3-12: Effect of shear on slip velocity for Newtonian, shear-thinning, and shear-thickening fluids with constant densities in flow over circular no-slip boundaries ($\phi_{solid} = 16\%$).**

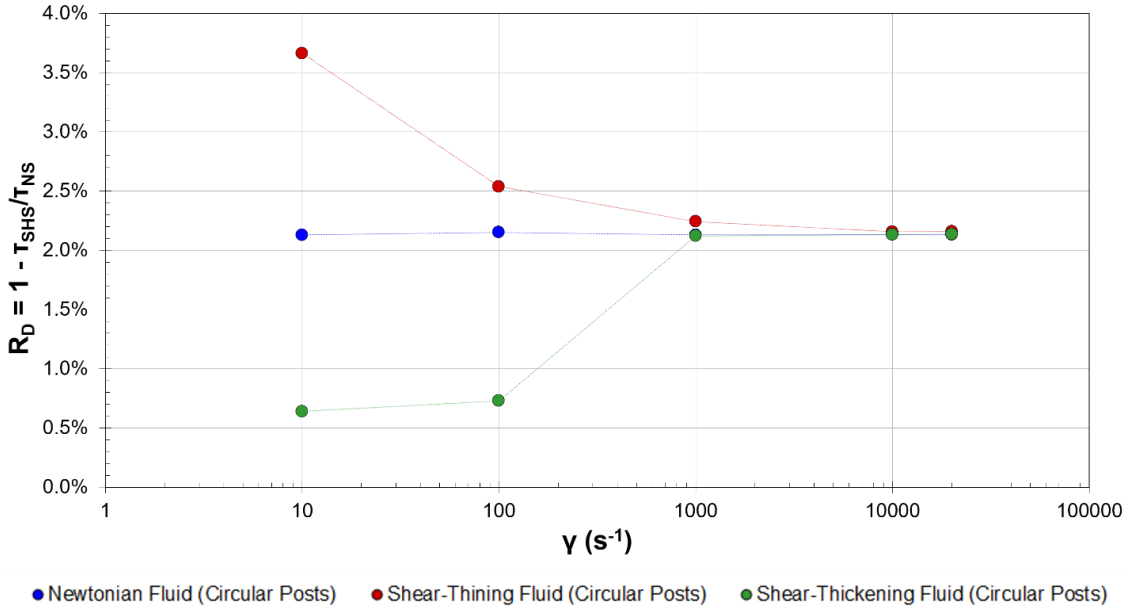


**Figure 3-13: Effect of shear on drag reduction for Newtonian, shear-thinning, and shear-thickening fluids with constant densities in flow over circular no-slip boundaries ($\phi_{solid} = 16\%$).**

## 3.8. Nomenclature

Roman Characters

| | |
|---|---|
| $\mathbf{A}, \mathbf{B}$ | Ybert et al. (2007) scaling law constants |
| $\mathbf{H}$ | Chanel height |
| $\mathbf{f_{NS}}$ | No-slip friction coefficient |
| $\mathbf{f_{SHS}}$ | Free-shear friction coefficient |
| $\mathbf{k}, \mathbf{n}$ | Material constant ($\mathbf{k = 0.001\ kg \cdot s^{n-2}/m}$, $\mathbf{n = 3.0}$) |
| $\boldsymbol{\ell_{slip}}$ | Effective slip length |
| $\mathbf{L}$ | Distance between centers of roughness elements |
| $\dot{\mathbf{m}}$ | Mass flow rate |
| $\mathbf{R_D}$ | Drag reduction |
| $\mathbf{\bar{U}_{NS}}$ | Average velocity in a no-slip channel |
| $\mathbf{U_0}$ | Shearing wall velocity |
| $\mathbf{U_{slip}}$ | Slip velocity |

Greek Characters

| | |
|---|---|
| $\boldsymbol{\partial p/\partial x}$ | Stream-wise pressure gradient |
| $\dot{\boldsymbol{\gamma}}$ | Shear rate |
| $\boldsymbol{\lambda}$ | Carreau model constant ($\boldsymbol{\lambda = 3.31\ s}$) |
| $\boldsymbol{\mu}$ | Fluid viscosity |
| $\boldsymbol{\mu_0}$ | Carreau model lower viscosity limit |
| $\boldsymbol{\mu_\infty}$ | Carreau model upper viscosity limit |
| $\boldsymbol{\mu_{max}}$ | Power law model maximum viscosity |

| | |
|---|---|
| $\boldsymbol{\mu_{min}}$ | Power law model minimum viscosity |
| $\boldsymbol{\rho}$ | Fluid density |
| $\boldsymbol{\tau_{w,NS}}$ | No-slip wall shear stress |
| $\boldsymbol{\tau_{w,SHS}}$ | Free-shear wall shear stress |
| $\boldsymbol{\phi_{solid}}$ | Solid (wetted) fraction |

## 3.9. References


Asmolov, Evgeny S., and Olga I. Vinogradova. "Effective slip boundary conditions for arbitrary one-dimensional surfaces." *Journal of Fluid Mechanics* 706 (2012): 108-117.

Belyaev, Aleksey V., and Olga I. Vinogradova. "Effective slip in pressure-driven flow past super-hydrophobic stripes." *Journal of Fluid Mechanics* 652 (2010): 489-499.

Belyaev, Aleksey V., and Olga I. Vinogradova. "Hydrodynamic interaction with super-hydrophobic surfaces." *Soft Matter* 6, no. 18 (2010): 4563-4570.

Bird, R. Byron, Warren E. Stewart, and Edwin N. Lightfoot. *Transport Phenomena.* New York: John Wiley & Sons, 2002.

Birjandi, F. Ch, and J. Sargolzaei. "Super-non-wettable surfaces: A review." *Colloids and Surfaces A: Physicochemical and Engineering Aspects* 448 (2014): 93-106.

Bittoun, Eyal, and Abraham Marmur. "The role of multiscale roughness in the lotus effect: is it essential for super-hydrophobicity?." *Langmuir* 28, no. 39 (2012): 13933-13942.

Brown, Eric, and Heinrich M. Jaeger. "Dynamic jamming point for shear thickening suspensions." *Physical Review Letters* 103, no. 8 (2009): 086001.

Busse, Angela, Neil D. Sandham, Glen McHale, and Michael I. Newton. "Change in drag, apparent slip and optimum air layer thickness for laminar flow over an idealised superhydrophobic surface." *Journal of Fluid Mechanics* 727 (2013): 488-508.

Choi, Chang-Hwan, and Chang-Jin Kim. "Large slip of aqueous liquid flow over a nanoengineered superhydrophobic surface." *Physical Review Letters* 96, no. 6 (2006): 066001.

Colace, Thomas V., Garth W. Tormoen, Owen JT McCarty, and Scott L. Diamond. "Microfluidics and coagulation biology." *Annual Review of Biomedical Engineering* 15 (2013): 283.

Davis, Anthony MJ, and Eric Lauga. "Hydrodynamic friction of fakir-like superhydrophobic surfaces." *Journal of Fluid Mechanics* 661 (2010): 402-411.

Davis, Anthony MJ, and Eric Lauga. "The friction of a mesh-like super-hydrophobic surface." *Physics of Fluids (1994-present)* 21, no. 11 (2009): 113101.

Feuillebois, François, Martin Z. Bazant, and Olga I. Vinogradova. "Effective slip over superhydrophobic surfaces in thin channels." *Physical Review Letters* 102, no. 2 (2009): 026001.

Fukagata, Koji, Nobuhide Kasagi, and Petros Koumoutsakos. "A theoretical prediction of friction drag reduction in turbulent flow by superhydrophobic surfaces." *Physics of Fluids (1994-present)* 18, no. 5 (2006): 051703.

Galdi, Giovanni P., Rolf Rannacher, Anne M. Robertson, and Stefan Turek. "Hemodynamical flows." *Delhi Book Store* (2008).

Gilbert, Richard J., Hyesung Park, Marco Rasponi, Alberto Redaelli, Barry Gellman, Kurt A. Dasse, and Todd Thorsen. "Computational and functional evaluation of a microfluidic blood flow device." *ASAIO Journal* 53, no. 4 (2007): 447-455.

Ho, Tuan Anh, Dimitrios V. Papavassiliou, Lloyd L. Lee, and Alberto Striolo. "Liquid water can slip on a hydrophilic surface." *Proceedings of the National Academy of Sciences* 108, no. 39 (2011): 16170-16175.

Johnston, Barbara M., Peter R. Johnston, Stuart Corney, and David Kilpatrick. "Non-Newtonian blood flow in human right coronary arteries: steady state simulations." *Journal of Biomechanics* 37, no. 5 (2004): 709-720.

Lauga, Eric, and Howard A. Stone. "Effective slip in pressure-driven Stokes flow." *Journal of Fluid Mechanics* 489 (2003): 55-77.

Lee, Choongyeop, and Chang-Hwan Choi. "Structured surfaces for a giant liquid slip." *Physical Review Letters* 101, no. 6 (2008): 064501.

Lee, Thomas, Eric Charrault, and Chiara Neto. "Interfacial slip on rough, patterned and soft surfaces: A review of experiments and simulations." *Advances in Colloid and Interface Science* 210 (2014): 21-38.

Martell, Michael B., J. Blair Perot, and Jonathan P. Rothstein. "Direct numerical simulations of turbulent flows over superhydrophobic surfaces." *Journal of Fluid Mechanics* 620 (2009): 31-41.

Martini, Ashlie, Hua-Yi Hsu, Neelesh A. Patankar, and Seth Lichter. "Slip at high shear rates." *Physical Review Letters* 100, no. 20 (2008): 206001.

Neinhuis, C., and W. Barthlott. "Characterization and distribution of water-repellent, self-cleaning plant surfaces." *Annals of Botany* 79, no. 6 (1997): 667-677.

Ng, Chiu-On, and C. Y. Wang. "Apparent slip arising from Stokes shear flow over a bidimensional patterned surface." *Microfluidics and Nanofluidics* 8, no. 3 (2010): 361-371.

Ou, Jia, Blair Perot, and Jonathan P. Rothstein. "Laminar drag reduction in microchannels using ultrahydrophobic surfaces." *Physics of Fluids (1994-present)* 16, no. 12 (2004): 4635-4643.

Philip, John R. "Flows satisfying mixed no-slip and no-shear conditions." *Journal of Applied Mathematics and Physics ZAMP* 23, No 3 (1972): 353-372.

Priezjev, Nikolai V., and Sandra M. Troian. "Influence of periodic wall roughness on the slip behaviour at liquid/solid interfaces: molecular-scale simulations versus continuum predictions." *Journal of Fluid Mechanics* 554 (2006): 25-46.

Quéré, David. "Wetting and roughness." *Annu. Rev. Mater. Res.* 38 (2008): 71-99.

Rothstein, Jonathan P. "Slip on superhydrophobic surfaces." *Annual Review of Fluid Mechanics* 42 (2010): 89-109.

Shirtcliffe, N. J., and P. Roach. "Superhydrophobicity for Antifouling Microfluidic Surfaces." In *Microfluidic Diagnostics*, pp. 269-281. Humana Press, 2013.

Shirtcliffe, N. J., R. Toon, and P. Roach. "Surface Treatments for Microfluidic Biocompatibility." In *Microfluidic Diagnostics*, pp. 241-268. Humana Press, 2013.

Sochi, Taha. "Slip at fluid-solid interface." *Polymer Reviews* 51, no. 4 (2011): 309-340.

Srinivasan, Siddarth, Wonjae Choi, Kyoo-Chul Park, Shreerang S. Chhatre, Robert E. Cohen, and Gareth H. McKinley. "Drag reduction for viscous laminar flow on spray-coated non-wetting surfaces." *Soft Matter* 9, no. 24 (2013): 5691-5702.

Stroock, A. D., and G. M. Whitesides. "Flexible methods for microfluidics." *Phys. Today* 54 (2001): 42-48.

Tanner, Roger I. *Engineering Rheology*. Oxford University Press, 2000.

Tian, Wei-Cheng, and Erin Finehout, eds. *Microfluidics for Biological Applications*. Vol. 16. Springer Science & Business Media, 2009.

Vinogradova, Olga I., and Aleksey V. Belyaev. "Wetting, roughness and flow boundary conditions." *Journal of Physics: Condensed Matter* 23, no. 18 (2011): 184104.

Voronov, Roman S., Dimitrios V. Papavassiliou, and Lloyd L. Lee. "Review of fluid slip over superhydrophobic surfaces and its dependence on the contact angle." *Industrial & Engineering Chemistry Research* 47, no. 8 (2008): 2455-2477.

Watanabe, Keizo, Yanuar Udagawa, and Hiroshi Udagawa. "Drag reduction of Newtonian fluid in a circular pipe with a highly water-repellent wall." *Journal of Fluid Mechanics* 381 (1999): 225-238.

Ybert, Christophe, Catherine Barentin, Cecile Cottin-Bizonne, Pierre Joseph, and Lyderic Bocquet. "Achieving large slip with superhydrophobic surfaces: Scaling laws for generic geometries." *Physics of Fluids (1994-present)* 19, no. 12 (2007): 123601.

# Chapter 4: *A Priori* Models for Effective Slip

## 4.1. Introduction

Slip at fluid-fluid and fluid-solid interfaces is a subject of interest for many engineering applications, ranging from porous materials to biomedical devices to separation processes. As introduced in **Chapter 1.4** and discussed in **Chapters 2** and **3**, superhydrophobic surfaces (SHSs) are among the many systems in which slip at a fluid-fluid interface may be observed.

Remarkable effort has been made to include the effects of surface topology, as well as various flow and physical properties, in models describing fluid slip. In most studies, the air-water interface is assumed to be flat and the Cassie state of the SHS is modeled as a smooth surface with alternating free-shear and no-slip boundary conditions representing gas/liquid regions and solid/liquid regions, respectively (Lauga and Stone, 2003; Ybert et al., 2007; Feuillebois, Bazant, and Vinogradova, 2009; Belyaev and Vinogradova, 2010. Nonetheless, the mathematical description of flow over these surfaces is still incomplete and, as a consequence, optimization of these surfaces would benefit significantly from the development of a more robust model.

## 4.2. Background

### *4.2.1. Slip and Drag Reduction*

According to Navier's slip model, the slip length may be defined as (Lee, Choi, and Kim, 2008; Voronov, Papavassiliou, and Lee, 2008; Rothstein, 2009):

$$\ell_{\mathbf{slip}} = \frac{\mathbf{U_{slip}}}{\dot{\boldsymbol{\gamma}}} \qquad \textbf{(4-1)}$$

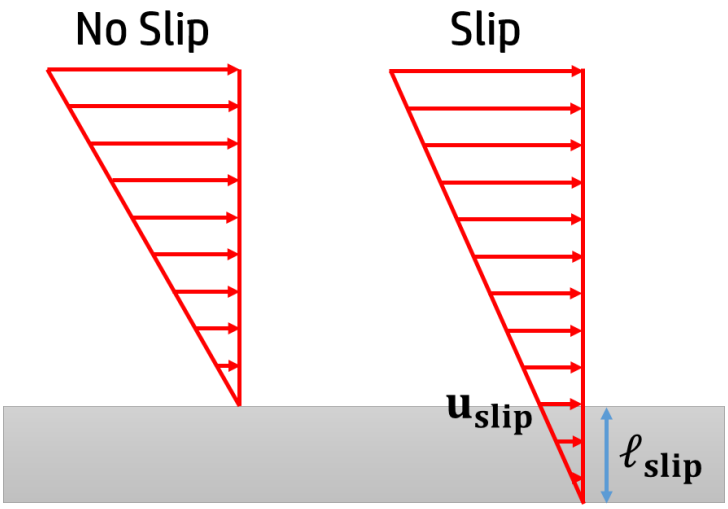


**Figure 4-1: Schematic of no-slip and slip at solid-liquid interface.**

where $\boldsymbol{\ell_{slip}}$ is the slip length, $\mathbf{U_{slip}}$ is the slip velocity at the wall, and $\dot{\boldsymbol{\gamma}} \equiv \left[\vec{\nabla}\,\vec{\mathbf{U}}\right]_{yx}$ is the velocity gradient normal to the wall.

While the slip length may be sufficient to classify many types of systems involving mixed slip boundaries, the slip velocity is arguably a more practical choice as a variable to characterize such systems since it incorporates two units, and is thus sufficient for measuring kinematic phenomena (Barenblatt, 2003). This observation, when combined with the fact that the shape of the velocity distribution should be independent of time, implies that the velocity has a similarity solution (Batchelor, 2000). Furthermore, for systems involving laminar plane-Couette flow (shown in **Figure 4-1**), the drag reduction ($\mathbf{R_D}$) scales with the ratio of the slip velocity and the shearing wall velocity ($\mathbf{U_0}$):

$$\mathbf{R_D} \propto \frac{\mathbf{U_{slip}}}{\mathbf{U_0}} \qquad \textbf{(4-2)}$$

Thus, the slip velocity more completely characterizes systems involving mixed slip boundaries for drag reduction purposes and is applicable to a wider range of flows than the slip length.

### *4.2.2. Similarity Solutions*

Dimensional analysis and similitude are important concepts in many areas of science and engineering, including turbulent flow analysis, thermodynamics, heat and mass transfer, mechanics, and biology, among many others (Barenblatt, 1996; Sonin 2001; Barenblatt, 2003). This approach to problem solving is based on the generalized homogeneity of the physical laws governing most systems and takes advantage of similarity in the spatial distribution of characteristics of motion (Barenblatt and Zel'dovich, 1972). A well-known procedure based on this approach is the Buckingham method, which uses the Buckingham pi theorem to generate dimensionless groups of variables by defining important scales between key dimensions of systems (Welty et al., 2008). As a result, the governing differential equations for the system are transformed from partial to ordinary and the total number of unknown variables in the equations is reduced (Barenblatt, 1996; Batchelor, 2000).

Analogous to dimensional analysis, similarity solutions are used to scale velocities within a system by non-dimensionalizing the coordinates of the system rather than parameters, as in dimensional analysis (White, 2006). In fluid mechanics, similarity solutions are used in a number of contexts, such as to describe flow near a stagnation point, flow near a solid surface, and flow in turbulent jets (Bird, Stewart, and Lightfoot, 2002; White, 2006; Welty et al., 2008).

The concept of similitude has been explored by numerous investigators using both mathematical and physical arguments (Sedov, 1993; Sachdev, 2000; White, 2006; Welty et al., 2008). Similarity solutions can be used to describe the physical behavior of a system under specific conditions, as well as to describe intermediate asymptotic behavior for a wider range of problems, although such solutions are universally limited to certain geometries and boundary conditions (Sachdev, 2000; White, 2006).

According to the Π-theorem, a dimensional function of $\mathbf{n} = \mathbf{k} + \mathbf{m}$ dimensional governing parameters can be expressed as a dimensionless function of $\mathbf{m}$ parameters. By defining important scales between key dimensions of systems, the governing differential equations are transformed from partial to ordinary and the total number of unknown variables in the equations is reduced (Barenblatt, 1996; Batchelor, 2000). Self-similarity is also useful when developing approximations for solutions to more complicated problems and can offer insight into the characteristic properties of many types of systems.

### 4.3. Methodology and Validation

The Cassie state of the SHS is modeled as a smooth surface with alternating free-shear and no-slip boundary conditions representing gas/liquid regions and solid/liquid regions, respectively.

Several boundary shapes are considered in this study: rectangles, circles, and squares, as illustrated in **Figure 4-2**. The systems, shown in **Figure 4-2** for the rectangular no-slip/free-shear boundaries, consist of two infinite parallel

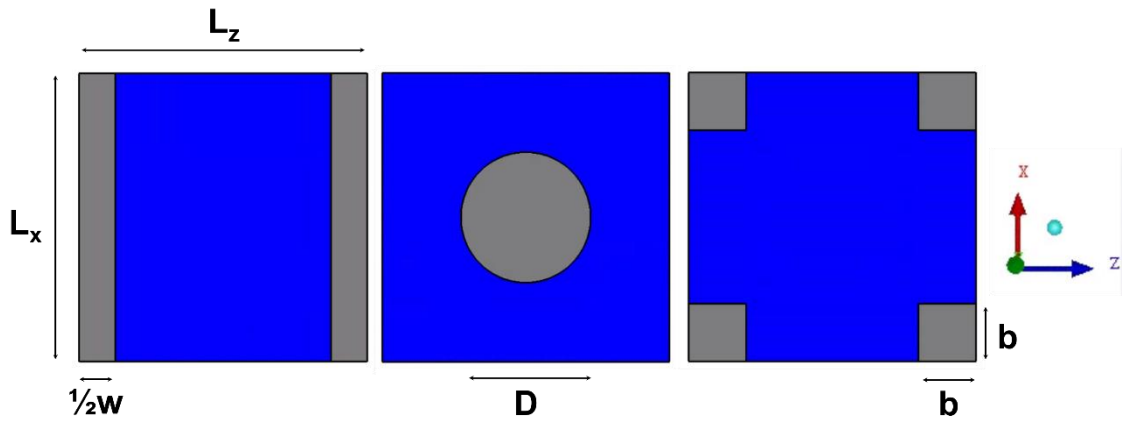


**Figure 4-2: Free-shear and no-slip boundary shapes and dimensions.**

***Gray coloring indicates areas with no-slip boundary conditions; blue coloring indicates areas with free-shear boundary conditions.***

plates separated at a distance ($\mathbf{H}$). The top wall is moved in the positive $x-$direction at a constant shearing velocity.

The simplest case considered is for the system with rectangular shaped boundaries. The bottom wall is stationary, with periodically repeating rectangular no-slip boundaries of length ($\mathbf{L_x}$) and width ($\mathbf{w}$). Between these no-slip boundaries are free-shear boundaries of length($\mathbf{L_x}$) and width($\mathbf{L_z - w}$). A similar set-up is used with the circular and square boundaries, with periodically repeating square and circular no-slip boundaries of dimensions, ($\mathbf{2b}$) and ($\mathbf{D}$), respectively.

A microchannel with dimensions of $10\ \mu m \times 190\ \mu m \times 10 \mu m$ in the $x-$, $y-$, and $z-$ directions, respectively, is modelled as periodic in the span- and stream-wise directions. All meshes are created using the ANSYS® ICEM CFD™ (version 14.0) meshing software. The grid is generated using three-dimensional blocking with node spacing no greater than 0.125 μm in the $x-$ and $z-$ directions. The error in velocity solutions obtained using this spacing, which

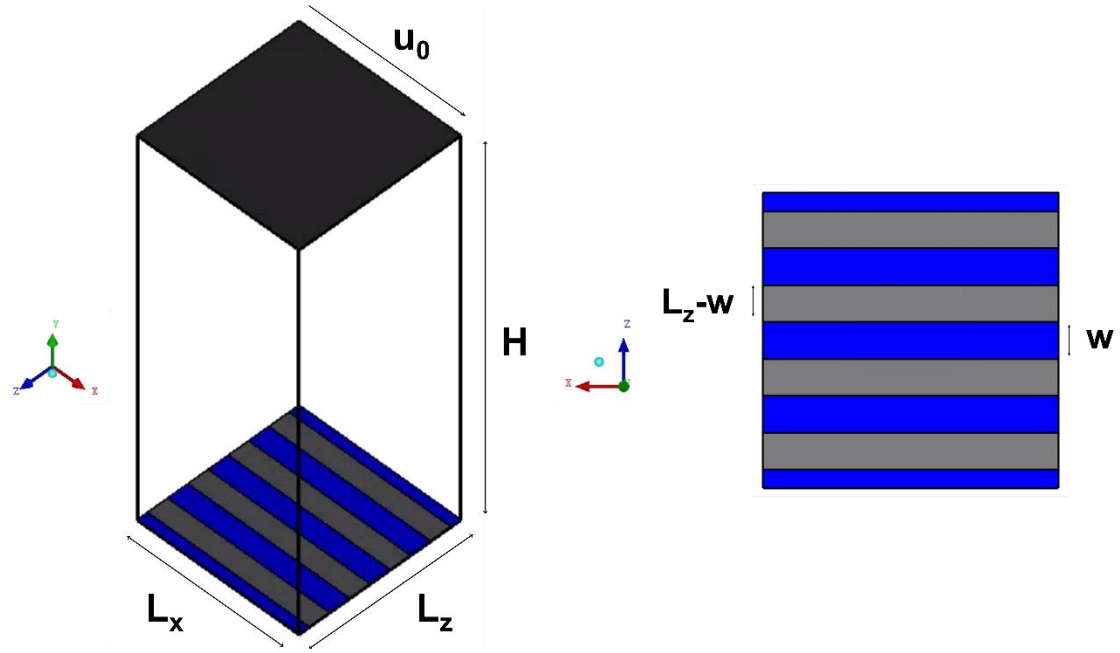


**Figure 4-3: Modeled channel geometry, boundary conditions, and dimensions.**

***Gray coloring indicates areas with no-slip boundary conditions; blue coloring indicates areas with free-shear boundary conditions.***

consists of approximately 350,000 nodes, is less than 4% when compared with those obtained using a mesh of nearly 500,000 nodes. ANSYS® FLUENT® (version 14.0) is used to simulate the flow of the fluid over the roughness elements of interest in the microchannel.

A second order-upwind discretization scheme is used. Residuals for the continuity and momentum equations are required to be reduced by at least four orders of magnitude, while the value for the velocity magnitude on the wall modeled with the free shear boundary condition is monitored for convergence, which is determined to be reached when the slip velocity changes by less than 0.5% over 100 iterations. In general, convergence criteria of $1x10^{-8}$ for the

continuity and momentum residuals are determined to be sufficient to reach a converged value for the velocity gradients.

## 4.4. Development of Equations for Velocity

The development of the model for the equivalent slip velocity requires an equation to describe the velocity as a function of $z$ (span-wise direction) on a plane tangent to the wall with the mixed no-slip/free shear boundary conditions.

### *4.4.1. Flow over Rectangular Mixed Slip Boundaries*

For span- and stream-wise periodic laminar flow along rectangular no-slip/free shear-boundaries, it is assumed that there is no $y-$ or $z-$ velocity. In this case, the Navier-Stokes equations (**Equation 1.2-8**) reduce to:

$$\vec{\nabla}^2\vec{U} = 0 \tag{4-6}$$

The boundary conditions for this system would be:

$$\bar{\bar{\tau}} \to 0 \text{ as } z/(L_z - w) \to 0 \tag{4-7}$$

$$\vec{U} = 0 \text{ at } z/(L_z - w) = \pm\frac{1}{2} \tag{4-8}$$

$$\vec{U} \to U_m \text{ as } z/(L_z - w) \to 0 \tag{4-9}$$

$$\vec{U} \to U_0 \text{ as } y/H \to 1 \tag{4-10}$$

where $\bar{\bar{\tau}}$ is the shear stress and $U_m$ is the centerline (i.e. maximum) velocity.

The final form of the instantaneous velocity equation for flow along rectangular no-slip/free-shear boundaries would then be:

$$\frac{\vec{U}}{U_m} = 1 - 4\left(\frac{z}{L_z - w}\right)^2 \tag{4-11}$$

Next, the average velocity ($\bar{U}_{xz}$) along the xz-plane must be estimated according to:

$$\bar{U}_{xz} = \frac{\iint \vec{U} dx dz}{\iint \vec{U} x dz} \quad \textbf{(4-12)}$$

Integrating for $x_0/L_x = 0, x_f/L_x = 1, z_0/(L_z - w) = -\frac{1}{2}$, $z_f/(L_z - w) = \frac{1}{2}$ yields:

$$\frac{\bar{U}_{xz}}{U_m} = \frac{2}{3}\left(\frac{L_z - w}{L_z}\right) \quad \textbf{(4-12)}$$

*4.4.2. Flow over Circular and Square Mixed Slip Boundaries*

The most straightforward approach to approximating an for the velocity profile along no slip circular and square shaped boundary conditions is to find the components of the velocity vector using the stream function ($\psi$), shown in **Equation 4-13**, for Falkner-Skan wedge flow (White, 2006):

$$\psi = C r^2 \sin 2\theta \quad \textbf{(4-13)}$$

where $C$ is a constant.

Since $U_r = \left[\vec{\nabla}\psi\right]_\theta$ and $U_\theta = -\left[\vec{\nabla}\psi\right]_r$

$$\frac{\bar{U}_{r\theta}}{U_m} = \frac{8}{3L^3}\left(r_f^3 - r_0^3\right)(\theta_f - \theta_0) \quad \textbf{(4-14)}$$

where $r_0/L_z = R/L_z, r_f/L_z = 1/2, \theta_0 = 0, \theta_f = \pi/2$.

While solutions for complex potential flow around multiple cylinders do exist, further consideration of the streamline plot for flow around a cylinder suggests that the velocity profile for a periodically repeating no-slip boundary condition can be estimated by limiting the boundaries of integration to $R/L_z \leq r/L_z \leq 1/2$ and $0 \leq \theta \leq \pi/2$, which corresponds to the area enclosed by the dotted lines in **Figure 4-4.**

The average velocity for a surface with square posts would be identical to **Equation 4-14** with the following bounds: $r_0/L_z = b/L_z, r_f/L_z = 1/2, \theta_0 =$

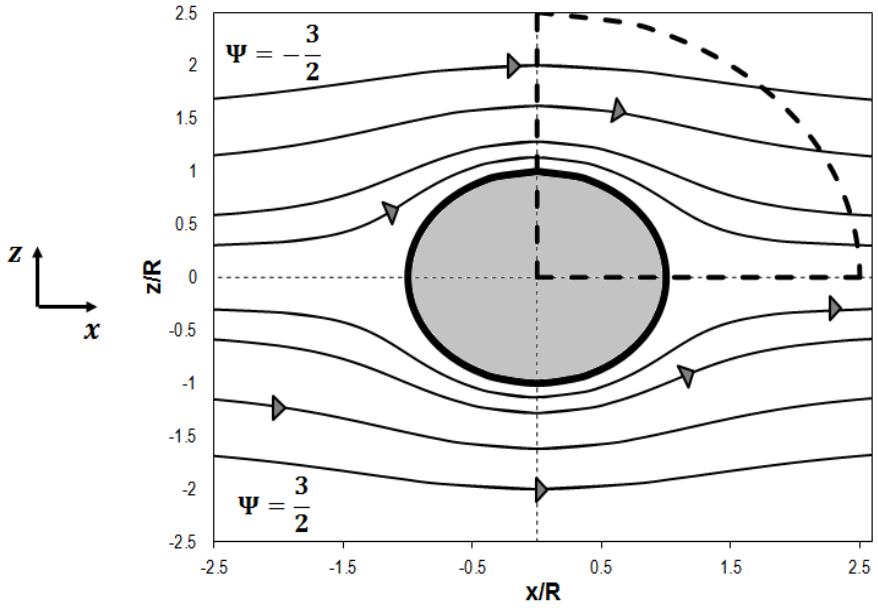


**Figure 4-4: Streamlines for flow over a circular no-slip boundary. The area enclosed by the dashed curves corresponds to the area over which the velocities are integrated.**

$\mathbf{0}, \boldsymbol{\theta_f} = \boldsymbol{\pi/2}$. To avoid lengthy equations and simplify calculations, the components of velocity for flow over posts are evaluated over $\mathbf{0} \leq \boldsymbol{\theta} \leq \frac{\boldsymbol{\pi}}{\mathbf{2}}$ and $\mathbf{0} \leq \mathbf{r/L_z} \leq \mathbf{1/2}$ rather than over $\mathbf{0} \leq \boldsymbol{\theta} \leq \boldsymbol{\pi/4}$ and $\mathbf{0} \leq \mathbf{r/L_z} \leq \mathbf{1/2}\,\mathbf{tan}\,\boldsymbol{\theta}$ and $\boldsymbol{\pi/4} < \boldsymbol{\theta} \leq \boldsymbol{\pi/2}$ and $\mathbf{1/2}\,\mathbf{tan}\,\boldsymbol{\theta} \leq \mathbf{r/L_z} \leq \mathbf{1/2}$.

## 4.4. Results and Discussion

### *4.4.2. Solutions of Similarity*

For the system shown in **Figure 4-3**, suppose the following relationship can be defined for the velocity along any $\mathbf{y}-, \mathbf{z}-$ plane by:

$$\widetilde{\mathbf{U}}(\mathbf{y}, \boldsymbol{\xi}) \equiv \frac{\vec{\mathbf{U}}}{\mathbf{U_m}} \qquad \textbf{(4-15)}$$

where $\boldsymbol{\xi} \equiv \mathbf{z}/\boldsymbol{\delta}(\mathbf{y})$ and $\boldsymbol{\delta}(\mathbf{y})$ is a characteristic length scale. The variable $\widetilde{\mathbf{U}}(\mathbf{y}, \boldsymbol{\xi})$ would then be a function of $\mathbf{y}$ and the scaled variable $\boldsymbol{\xi}$ and will be referred to as the *equivalent slip velocity*.

If the equivalent slip velocity can be defined such that it is independent of $\mathbf{y}$ then $\vec{\mathbf{U}}$ at may be classified as self-similar and can be described in terms of functions of $\mathbf{U_m}$ and $\widetilde{\mathbf{U}}(\mathbf{y}, \boldsymbol{\xi})$ (Pope 2000).

Using this knowledge, a relationship between the equivalent slip velocity and the average velocity given in **Equation 4-12** would be described by:

$$\frac{\bar{\mathbf{U}}}{\mathbf{U_0}} = \frac{\mathbf{1}}{\widetilde{\mathbf{U}}}\left(\frac{\bar{\mathbf{U}}}{\mathbf{U_m}}\right) \tag{4-16}$$

Observing that the equivalent slip velocity for laminar, Couette flow of a Newtonian fluid would be a function of the geometry of the system alone, an equation for this variable should be a function of the system's characteristic length scales. For the system with rectangular free-shear/no-slip boundaries shown in **Figure 4-3**, the key variables would be the span-wise length of the no-slip boundary ($\mathbf{L_z}$), the span-wise length of the free-shear boundary ($\mathbf{L_z - w}$), and the distance between the top and bottom plates ($\mathbf{H}$).

Thus, a suitable form for the equivalent slip velocity for flow over rectangular free-shear/no-slip boundaries ($\widetilde{\mathbf{U}}_\mathbf{R}$) could be:

$$\widetilde{\mathbf{U}}_\mathbf{R} = \frac{\mathbf{2}}{\mathbf{3}}\left(\frac{\mathbf{L_z - w}}{\mathbf{L_z}}\right)\left[\frac{\mathbf{1}}{\mathbf{4}}\left(\frac{\mathbf{L_z}}{\mathbf{L_z - w}} + \frac{\mathbf{1}}{\mathbf{2}}\left(\frac{\mathbf{w}}{\mathbf{L_z}}\right)\right)\right]\left[\mathbf{1} + \mathbf{3}\left(\frac{\mathbf{H}}{\mathbf{L_z - w}}\right)\right] \tag{4-17}$$

Using similar logic, the equivalent slip velocities for flow over circular and square shaped boundaries may be defined as functions of the equivalent slip velocity for the rectangular boundaries. Then the equivalent slip velocity for flow over circular posts ($\widetilde{\mathbf{U}}_\mathbf{C}$) may be defined as:

$$\widetilde{\mathbf{U}}_\mathbf{C} = \left(\frac{\boldsymbol{\pi}\mathbf{R}}{\mathbf{L_z}}\right)\widetilde{\mathbf{U}}_\mathbf{R} \tag{4-18}$$

Similarly, the equivalent slip velocity for flow over square posts ($\widetilde{\mathbf{U}}_{\mathbf{S}}$) may be described by:

$$\widetilde{\mathbf{U}}_{\mathbf{S}} = \left(\frac{\mathbf{4b}}{\mathbf{L_z}}\right)\widetilde{\mathbf{U}}_{\mathbf{R}} \qquad \textbf{(4-19)}$$

The equivalent slip velocity for a non-Newtonian fluid ($\widetilde{\mathbf{U}}_{\mathbf{NN}}$) as may be related to that for a Newtonian fluid ($\widetilde{\mathbf{U}}_{\mathbf{N}}$) for flow over all of the boundary shapes considered in this study. By simply relating the viscosity of the non-Newtonian ($\boldsymbol{\mu}_{\mathbf{NN}}$) fluid to that of the Newtonian fluid ($\boldsymbol{\mu}_{\mathbf{N}}$) according to:

$$\widetilde{\mathbf{U}}_{\mathbf{NN}} = \left(\frac{\boldsymbol{\mu}_{\mathbf{NN}}}{\boldsymbol{\mu}_{\mathbf{N}}}\right)\widetilde{\mathbf{U}}_{\mathbf{N}} \qquad \textbf{(4-20)}$$

*7.4.3. Model Validation*

The effective slip lengths predicted using the proposed slip velocity model for rectangular no-slip/free-shear boundary conditions differ from those predicted by Philip's model in **Equation 3-1** by an average of less than 8%. This difference can be accounted for by recognizing that Philip's model was developed to describe flow over a *single* rectangular no-slip boundary, while the mod els presented in this study describe stream- and span-wise periodic flow.

Slip velocities for flow over rectangular no-slip boundaries, as predicted by the models presented in **Equations 4-17** and **4-20**, differ from numerical predictions by an average of 3.5% for both Newtonian (**Figure 4-5**) and non-Newtonian fluids (**Figure 4-6** and **Figure 4-7**).

The models presented in this chapter assume the velocity profile on the free shear boundary of the SHS has a maximum (i.e. $\left[\vec{\boldsymbol{\nabla}}\,\vec{\mathbf{U}}\right]_{\mathbf{zx}} = \mathbf{0}$) at the location located halfway between each roughness element. As shown in **Figure 7-8** for

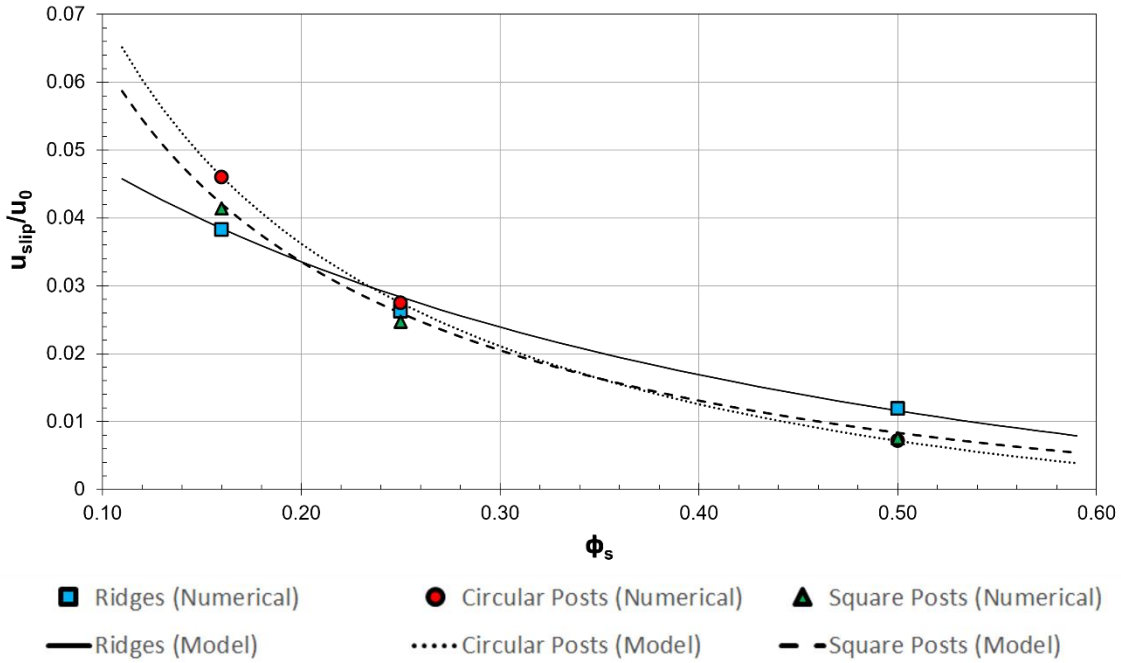


**Figure 4-5: Comparison of numerical and model results for the dependence of slip velocity on no-slip surface coverage for Newtonian fluid in laminar flow ($U_0 = 0.019$ m/s).**

16% solid fraction, the centerline velocity is observed to remain a maximum for all surface coverages up to 50% no slip surface area. Numerical estimates for the velocity profile along a surface with circular and square no-slip boundaries also confirm this assumption.

The velocity gradient with respect to z-position is assumed to be symmetrical about each no-slip region. **Figure 4-9** is an illustration of the contours of velocity for flow on surfaces with 16% no slip surface area. The contour plots confirm the symmetry of velocity around the no-slip boundary.

### 4.5. Summary and Conclusions

The possibility of using superhydrophobic surfaces to reduce drag in both laminar and turbulent flows has captured the interest of fluid flow researchers in

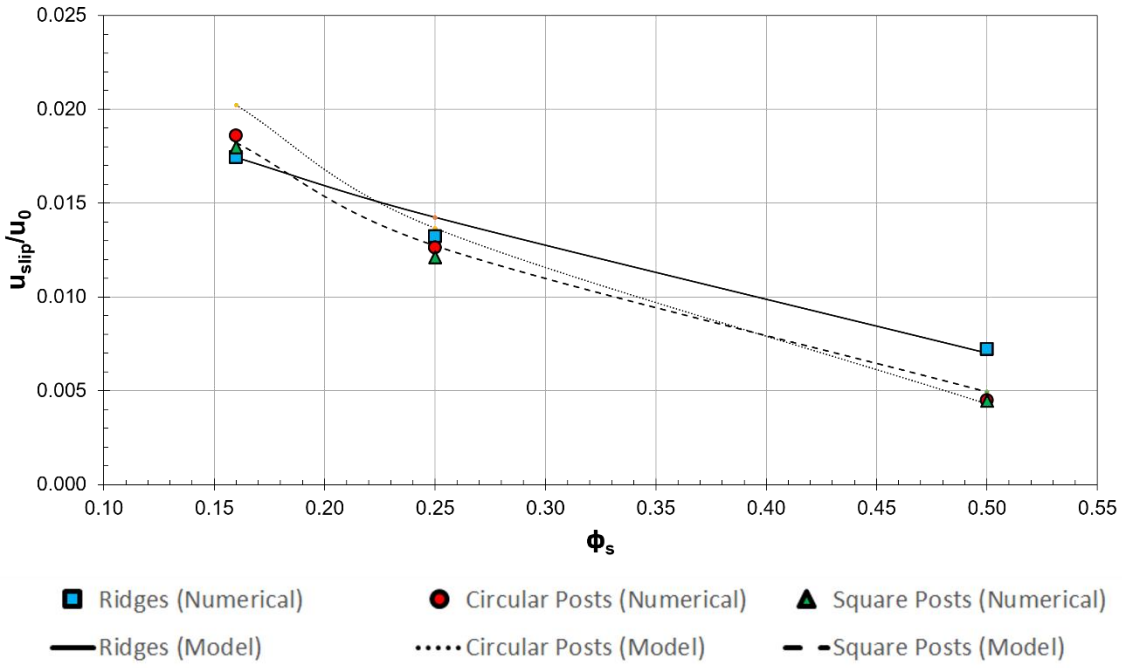


**Figure 4-6: Comparison of numerical and model results for the dependence of slip velocity on no-slip surface coverage for shear-thickening fluid in laminar flow ($\mathbf{U_0 = 0.019\ m/s}$).**

recent years. Although many investigators have proposed models for predicitng the slip length ($\boldsymbol{\ell_{slip}}$), drag reduction over a surface with mixed no-slip/free-shear boundary conditions is directly proportional to the ratio of the slip velocity ($\mathbf{U_{slip}}$) to the shearing wall velocity ($\mathbf{U_0}$). Thus, *a priori* prediction of the slip velocity would greatly facilitate the development of superhydrophobic surfaces for drag reduction applications. While many researchers have proposed models to describe the slip length for a SH system, the slip velocity is shown to more completely characterize flow over mixed slip boundaries for drag reduction purposes.

The slip velocity at the mixed-slip wall can be related to the shearing wall velocity by defining an equivalent slip velocity ($\widetilde{\mathbf{U}}$) for the system. Using self-similarity theory, the equivalent slip velocity can then be expressed as a function

of the geometry of the system and can predict the slip velocity for flow over a surface consisting of periodically repeating no-slip/free-shear boundaries in the shape of rectangles for a solid fraction of $\mathbf{16\% \leq \phi_{solid} \leq 50\%}$. Furthermore, the equivalent slip velocity for flow over rectangular boundaries can be related to the equivalent slip velocity for flow over surfaces with square and circular no-slip boundaries using characteristic length ratios. The self-similarity approach can also be used to describe non-Newtonian flow using viscosity ratios.

Previously proposed models are either entirely empirical and lacked obvious physical signifance or are dependent on a relatively ambiguous solid fraction. On the other hand, with the models and methods outlined in this study, the slip velocity and drag reduction can be estimated *a priori* using characteristic length and viscous scales related to the system. These estimates can then be used for a variety of purposes, such as to aid experimental design, to provide initialization and/or boundary conditions for numerical studies, and to optimize surface topologies.

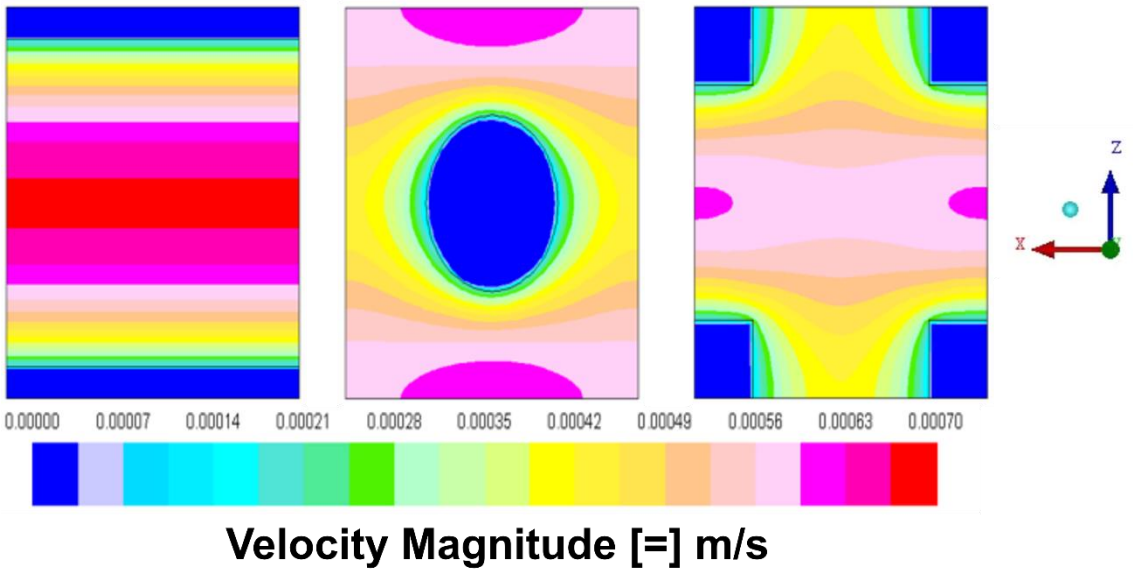


**Figure 4-7: Contours of velocity along mixed-slip surface.**

## 4.6. Nomenclature

Roman Characters

| | |
|---|---|
| $\mathbf{b}$ | Square post half-width |
| $\mathbf{D}$ | Circular post diameter |
| $\mathbf{H}$ | Distance separating top and bottom walls |
| $\boldsymbol{\ell}_{\mathbf{slip}}$ | Slip length |
| $\mathbf{L_x}, \mathbf{L_z}$ | Stream- and span-wise distance between center of roughness elements |
| $\mathbf{L_z - w}$ | Free-shear ridge width |
| $\mathbf{p}$ | Pressure |
| $\mathbf{R}$ | Circular post radius |
| $\mathbf{R_D}$ | Drag reduction |
| $\mathbf{U_0}$ | Shearing wall velocity |
| $\mathbf{U_m}$ | Maximum (centerline) velocity along $\mathrm{x} - z$ plane |
| $\mathbf{U_{slip}}$ | Slip velocity |
| $\mathbf{U_x}, \mathbf{U_y}, \mathbf{U_z}$ | $\mathrm{x} -$, $\mathrm{y} -$, $\mathrm{z} -$ velocity (respectively) |
| $\widetilde{\mathbf{U}}$ | Equivalent slip length |
| $\overline{\mathbf{U}}_{\mathbf{xz}}$ | Average velocity along an $\mathrm{x} - \mathrm{z}$ plane |
| $\mathbf{w}$ | No-slip ridge width |

Greek Characters

| | |
|---|---|
| $\dot{\boldsymbol{\gamma}}$ | Shear rate |
| $\boldsymbol{\delta}$ | Characteristic length scale |
| $\boldsymbol{\mu}$ | Fluid viscosity |
| $\boldsymbol{\xi}$ | Similarity scaling variable |

| | |
|---|---|
| $\boldsymbol{\rho}$ | Fluid density |
| $\boldsymbol{\phi_{solid}}$ | Solid (wetted) fraction of surface |

## 4.7. References


Barenblatt, G. I., and Ya B. Zel'Dovich. "Self-similar solutions as intermediate asymptotics." *Annual Review of Fluid Mechanics* 4, no. 1 (1972): 285-312.

Belyaev, Aleksey V., and Olga I. Vinogradova. "Hydrodynamic interaction with super-hydrophobic surfaces." *Soft Matter* 6, no. 18 (2010): 4563-4570.

Bird, R. Byron, Warren E. Stewart, and Edwin N. Lightfoot. *Transport phenomena.* New York: John Wiley & Sons, 2002.

Busse, Angela, Neil D. Sandham, Glen McHale, and Michael I. Newton. "Change in drag, apparent slip and optimum air layer thickness for laminar flow over an idealised superhydrophobic surface." *Journal of Fluid Mechanics* 727 (2013): 488-508.

Feuillebois, François, Martin Z. Bazant, and Olga I. Vinogradova. "Effective slip over superhydrophobic surfaces in thin channels." *Physical review letters* 102, no. 2 (2009): 026001.

Lauga, Eric, and Howard A. Stone. "Effective slip in pressure-driven Stokes flow." *Journal of Fluid Mechanics* 489 (2003): 55-77.

Lee, Choongyeop, and Chang-Hwan Choi. "Structured surfaces for a giant liquid slip." *Physical review letters* 101, no. 6 (2008): 064501.

Ou, Jia, Blair Perot, and Jonathan P. Rothstein. "Laminar drag reduction in microchannels using ultrahydrophobic surfaces." *Physics of Fluids (1994-present)* 16, no. 12 (2004): 4635-4643.

Philip, John R. "Flows satisfying mixed no-slip and no-shear conditions." *Journal of Applied Mathematics and Physics ZAMP* 23, No 3 (1972): 353-372.

Pope, Stephen B. *Turbulent flows*. Cambridge university press, 2000.

Quéré, David. "Wetting and roughness." *Annu. Rev. Mater. Res.* 38 (2008): 71-99.

Rothstein, Jonathan P. "Slip on superhydrophobic surfaces." *Annual Review of Fluid Mechanics* 42 (2010): 89-109.

Sedov, Leonid Ivanovich. *Similarity and dimensional methods in mechanics*. CRC press, 1993.

Sachdev, P. L. *Self-similarity and beyond: exact solutions of nonlinear problems*. CRC Press, 2000.

Voronov, Roman S., Dimitrios V. Papavassiliou, and Lloyd L. Lee. "Review of fluid slip over superhydrophobic surfaces and its dependence on the contact angle." *Industrial & Engineering Chemistry Research* 47, no. 8 (2008): 2455-2477.

Welty, James R., Charles E. Wicks, Gregory Rorrer, and Robert E. Wilson.*Fundamentals of momentum, heat, and mass transfer*. John Wiley & Sons, 2008.

White, Frank M., and Isla Corfield. *Viscous fluid flow*. Vol. 3. New York: McGraw-Hill, 2006.

Ybert, Christophe, Catherine Barentin, Cecile Cottin-Bizonne, Pierre Joseph, and Lyderic Bocquet. "Achieving large slip with superhydrophobic surfaces: Scaling laws for generic geometries." *Physics of Fluids (1994-present)* 19, no. 12 (2007): 123601.

# Chapter 5: Flow and Damage Models in a Centrifugal Pump

## 5.1. Introduction

Between 4.7 and 5.8 million Americans are affected by heart failure and an estimated 660,000 new cases are diagnosed every year for people over the age of 45 (Thunberg et al., 2010; Fraser et al., 2011; Carpenter et al., 2013). With only 3,000 suitable organ donors available worldwide each year and limitations associated with medications, many of those diagnosed with HF are forced to face an alarming reality: one in five people with HF die within 1 year, less than 60% survive beyond five years, and almost 15% die while waiting for a donor organ (Fraser et al., 2011; Hess et al., 2013). With an increasing prevalence of HF worldwide, the need for short- and long-term circulatory support is becoming more pressing. One such solution may be found in the ventricular assist device, which may be used as a bridge to recovery, as a bridge to transplantation, or as a permanent destination therapy (Behbahani et al., 2009; Wilson et al., 2009).

In an effort to facilitate and standardize the use of computational fluid dynamics for the design and optimization of blood-contacting devices, the United States Food and Drug Administration (FDA) launched a Critical Path Initiative (CPI) project to study two standard flow models for medical devices using CFD. The first study was initiated in 2008 to evaluate CFD as a biomedical research tool using a simple nozzle model. The second study is currently ongoing and is intended to assess numerical predictions and limitations in characterizing flow and predicting blood damage in a centrifugal blood pump (US Food and Drug

Administration; Stewart et al., 2012; Malinauska, Saha, and Sheldon, 2015). To validate the numerical results, the FDA will provide hemolysis measurements using porcine blood at an operating temperature of 25$^{o}$C in the experimental setup shown in **Figure 5-1**.

The design of blood pumps, which provide life-saving circulatory support in patients with heart failure, requires remarkable precision and attention to detail in order to replicate the functionality of the native heart without complications. In addition to being reliable and affordable, these devices must also be able to deliver adequate hydraulic performance and provide sufficient pumping support without causing significant damage to the blood (Behbahani et al., 2009; Fraser et al., 2011). CFD is a powerful tool for evaluating and optimizing these life-saving devices since the results of these simulations can significantly reduce the cost associated with laboratory testing and the development of device prototypes and can facilitate safe, effective, and rapid development of medical devices for the increasing number of patients with cardiovascular disease (Fraser et al., 2011).

In the present work, we present results of simulations of the flow field through the pump at different flow conditions and pump rotation rates. Emphasis is placed on testing different rheological models for blood, and on determining the effects that the application of these models has on the prediction of shear stresses and pressure drop through the pump. Hemolysis estimates are also presented by utilizing a power law model in both the Eulerian and the Lagrangian

framework. Comparisons between predictions when using a laminar versus a turbulence flow model are also made.

## 5.2. Considerations for Modeling Flow in Blood Pumps

Accurate prediction of blood flow through blood pumps and medical devices using computational fluid dynamics requires familiarity with the governing physics of each system and can greatly depend on the models chosen to describe the rheology and properties of the fluid. The accuracy of blood damage index estimates is also highly dependent on the models used to characterize trauma to blood components from flow. In many cases, however, the process of modelling complicated systems can be streamlined by identifying the physical phenomena most likely to significantly impact the system, specifying appropriate models to describe the dynamics of these phenomena, and neglecting or simplifying less influential factors. As a consequence, identifying the key physics necessary to adequately characterize these systems is one of the most important and laborious steps involved in the process of evaluating and developing medical devices using computational fluid dynamics.

### *5.2.1. Rheological Behavior of Blood*

Blood is shear-thinning and thixotropic, with an apparent viscosity that can increase by more than an order of magnitude at low shear rates (US Food and Drug Administration; Taskin et al., 2010; Malinauska, Saha, and Sheldon, 2015). Despite these non-Newtonian characteristics, the use of a Newtonian model is reasonable in many cases, since the viscosity of human blood is effectively

shear-independent at shear rates above 100 $s^{-1}$ (Fournier, 2007; Behbahani et al., 2009; Taskin et al. 2010; Fraser et al., 2011).

The viscosity of blood also depends on hematocrit (Coglianese et al., 2012). Although heart failure is prevalent in individuals with abnormally high hematocrit (>49% in men, >45% in women), the disease can also affect those with low and normal hematocrit levels (45%-48% in men, 41%-44% in women) **(7)**. Hematocrit is of particular interest since anemia was recently reported to be a factor in early prediction of the need for a ventricular assist device (VAD) in patients with advanced heart failure (Fujino et al., 2014).

In the present work, we examine the importance of including the non-Newtonian behavior of blood when modeling flow through the blood pump. Three rheological cases are considered:

(1) A Newtonian viscosity model with $\boldsymbol{\mu = 0.0035\ Pa \cdot s}$

(2) A non-Newtonian viscosity model described by the Carreau equation (**Equation 5-1**).

(3) A non-Newtonian viscosity model described by a Casson constitutive equation (**Equation 5-2)**.

In all cases the blood density is assumed to be constant with $\boldsymbol{\rho = 1035\ kg/m^3}$. Laminar flow simulations are carried out with all three rheological equations, while the Newtonian and Casson viscosity models are also used in turbulent flow simulations.

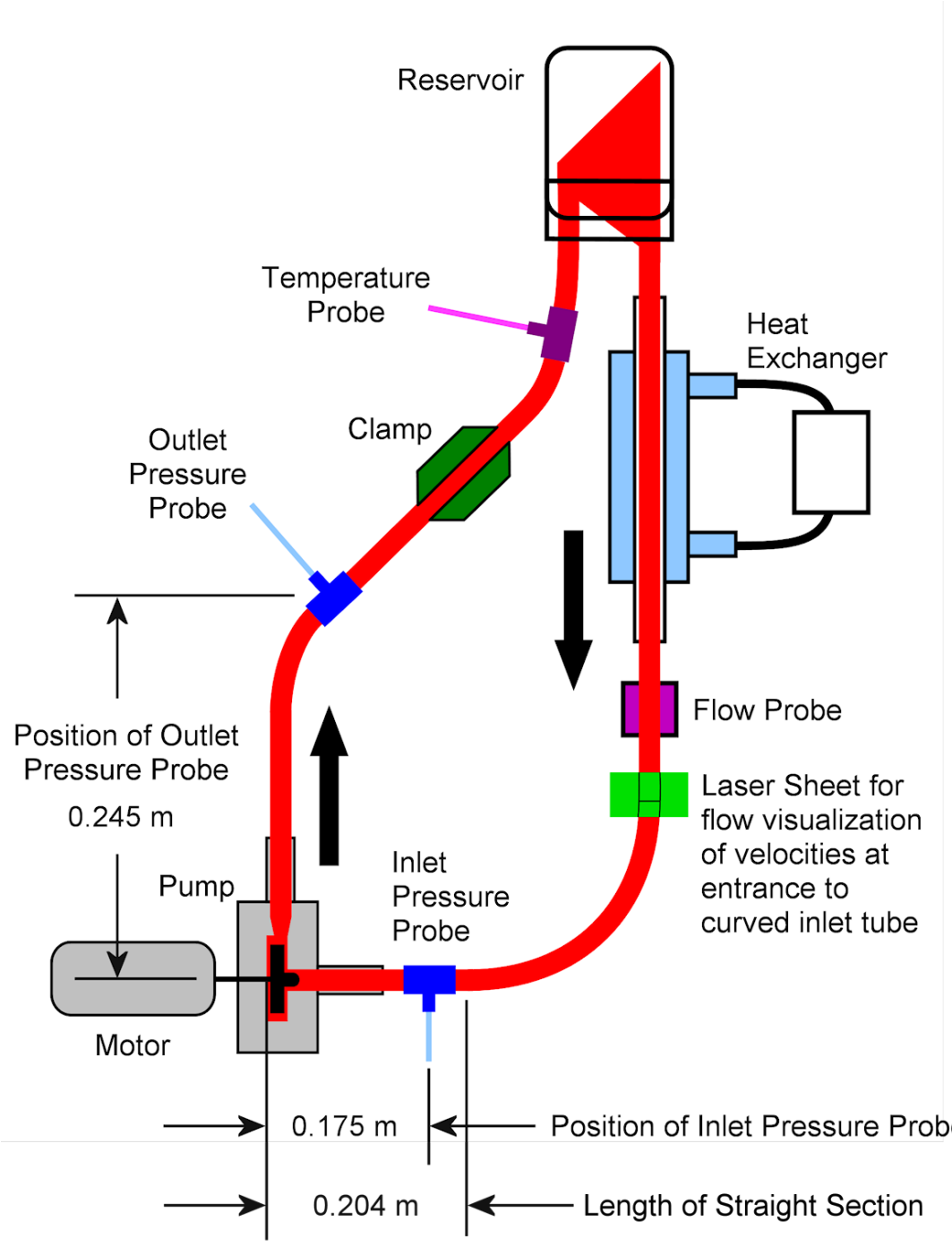


**Figure 5-1: Schematic diagram of the experimental setup for the FDA's blood damage experiments.**

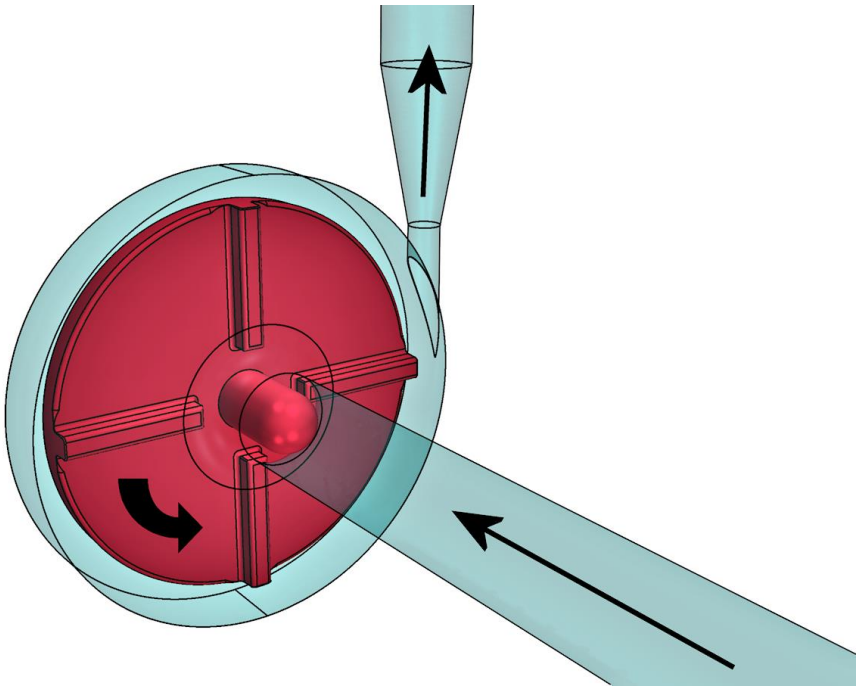

**Figure 5-2: Illustration of the FDA's simplified centrifugal blood pump model.**

The Carreau equation describes the shear thinning character of blood as a function of shear rate ($\dot{\gamma}$) using a power law relationship with upper ($\mu_0$) and lower ($\mu_\infty$) limits of viscosity, and it has the following form:

$$\frac{\mu - \mu_\infty}{\mu_0 - \mu_\infty} = [1 + (\lambda\dot{\gamma})^2]^{(n-1)/2} \qquad \textbf{(5-1)}$$

where $\mu$ is the apparent viscosity and the material constants are $\mu_0 = 57\ \text{mPa} \cdot \text{s}$, $\mu_\infty = 3.5\ \text{mPa} \cdot \text{s}$, $\lambda = 3.313\ \text{s}$, and $n = 0.3568$ (Jiang, 2014). The Carreau model for viscosity is a convenient choice for modeling the rheological behavior of blood since it is included in many commercial computational fluid dynamics codes.

The Casson equation, shown below, is often used to describe the shear stress-shear rate relationship for blood:

$$\sqrt{\boldsymbol{\tau}} = \sqrt{\boldsymbol{\tau_y}} + \sqrt{\boldsymbol{\mu\dot{\gamma}}} \qquad \textbf{(5-2)}$$

Where $\boldsymbol{\tau}$ is the shear stress and $\boldsymbol{\tau_y}$ is the yield stress and $\boldsymbol{\mu}$ is constant (Coglianese et al., 2012; Apostolidis and Beris, 2014). Apostolidis and Beris (2014) recently proposed a model to describe the dependence of the viscosity on hematocrit ($\mathbf{Hct}$) and temperature, according to the following equation:

$$\boldsymbol{\mu = n_p\left(1 + 2.0703 \times Hct + 3.7222 \times Hct^2\right) \times \exp\left[-7.0276\left(1 - \frac{T_0}{T}\right)\right]} \qquad \textbf{(5-3)}$$

where $\mathbf{n_p = 1.67 \times 10^{-5}\ Pa \cdot s}$ is the plasma viscosity, $\mathbf{T_0 = 296.16\ K}$ is the reference temperature, and $\mathbf{T}$ is the absolute temperature of the blood in degrees Kelvin.

To represent the distribution of hematocrit levels in patients with heart failure, three hematocrit levels are considered in this study: 25%, 36%, and 55%. The particular value of 36% corresponds to specifications for the FDA experiments. All runs presented are conducted at the reference temperature of 23°C, with the exception of **Case L1**, which is also modeled at 37°C to describe flow conditions for an intracorporeal device more accurately.

### *5.2.2. Flow Regime*

Because blood pumps and VADs operate in the transitional to low Reynolds number turbulence range, flow may be modeled as either laminar or turbulent. Use of a model for turbulence is not always justifiable in these devices, since equations that model turbulence are in general valid for fully developed and stationary turbulent flow; consequently, many researchers have opted to use laminar models and have obtained solutions that are able to predict pressure rises within blood pumps with reasonable accuracy. While the use of a turbulence

model may be associated with relatively large computational requirements, the use of one may be necessary to fully describe certain effects observed in VADs (Taskin et al., 2010; Zhang et al., 2013). Since few studies have explored the differences in flow field predictions between laminar and turbulent flow through these devices, the importance of capturing the physics of turbulence for the calculation of pressure drop is unclear. However, hemolysis is known to be affected by turbulence, as found experimentally either because of local pressure fluctuations that affect the cells, or because of eddies that dissipate turbulent kinetic energy and cause cell trauma (Kameneva et al., 2004; Ozturk, O'Rear, and Papavassiliou, 2015).

In this study, the flow of blood through the pump shown in **Figure 5-2** is modeled either as laminar or as turbulent. For cases in which the flow is treated as turbulent, the Shear-Stress Transport *k*-ω (**SST *k*-ω**) model is used. By blending two of the most popular and robust turbulence models (the standard *k*-epsilon and the standard *k*-omega), the **SST *k*-ω** model is less sensitive to free-stream turbulence properties and large, adverse pressure gradients than traditional models and results in more accurate flow field predictions in low-Reynolds number turbulence (Menter, 1994; Fluent Inc.®, 2001). This model has previously been used with some success to predict turbulent flow in a variety of complex systems, including in an axial blood flow pump with turbulence near the impeller tip, as examined by Su et al. (2011).

### *5.2.3. Formulations for Hemolysis Estimates*

Blood damage in pumps and VADs is primarily caused by the leaking of hemoglobin from red blood cells but can also be caused by rupture when the cells are exposed to shear rates greater than 42,000 $s^{-1}$ (Behbahani et al., 2009). Hemolysis is often quantified using a damage index such as the model proposed by Blackshear et al. (1965) and developed by Giersiepen et al. (1990):

$$\mathbf{D} = \frac{\Delta \mathbf{Hb}}{\mathbf{Hb}} = \mathbf{C}\mathbf{t}^{\boldsymbol{\alpha}}\boldsymbol{\tau}^{\boldsymbol{\beta}} \qquad \textbf{(5-4)}$$

where $\Delta\mathbf{Hb}/\mathbf{Hb}$ is the ratio of plasma-free hemoglobin to the total hemoglobin in the fluid, $\boldsymbol{\tau}$ is the shear stress to which a red blood cell is exposed for a certain time ($\mathbf{t}$) and $\mathbf{C}, \boldsymbol{\alpha}$ and $\boldsymbol{\beta}$ are constants typically determined from Couette laminar flow experiments. Based on the simulation results of Taskin et al. (2012), the constants used in **Equation 5-4** are chosen to be: $\mathbf{C} = \mathbf{1.800} \times \mathbf{10^{-6}}, \boldsymbol{\alpha} = \mathbf{0.7650}$, $\boldsymbol{\beta} = \mathbf{1.9910}$. While these constants were developed under laminar flow conditions, they are valid for shear stresses up to 700 Pa and exposure times less than 0.700 sec, which far exceed the ranges considered in this study (Taskin, 2012). This damage model is used to calculate the damage index by either a Eulerian or a Lagrangian formulation under both laminar and turbulent flow conditions.

The data obtained using the second stage CPI system in **Figure 5-1** will come from experiments with porcine blood. It should be noted that the species of the blood source can result in considerable differences in the constants used in hemolysis estimates. However, Ding et al. (2015) explored the variance in shear-induced hemolysis estimates between blood donor species and found that

the constants obtained for porcine blood did not differ significantly from those for human blood.

In this study, estimates for hemolysis are calculated using two approaches. In the Eulerian approach, the damage index is obtained by integration of fluid stresses over the volume of the entire computational domain ($\mathbf{V}$) according to (Garon and Farinas, 2004; Taskin et al., 2012):

$$\mathbf{D} = \left(\frac{\mathbf{1}}{\mathbf{Q}}\int \boldsymbol{\sigma}\mathbf{dV}\right)^{\boldsymbol{\alpha}} \tag{5-5}$$

where $\mathbf{Q}$ is the volumetric flow rate and $\boldsymbol{\sigma}$ is the rate of hemolysis production per unit time, defined as (Garon and Farinas, 2004):

$$\boldsymbol{\sigma} = \mathbf{C}^{1/\alpha}\boldsymbol{\tau}^{\beta/\alpha} \tag{5-6}$$

where $\boldsymbol{\tau}$ is the viscous stress.

In the Lagrangian approach, a discretized damage index is integrated over particle pathlines through the unit and then averaged using data collected for fluid particles introduced simultaneously into the flow. For a constant time step ($\Delta\mathbf{t}$) the linearized damage index is calculated as (Fraser et al., 2011):

$$\mathbf{D_{n+1}} = \mathbf{D_n} + (\mathbf{1} - \mathbf{D_n})\mathbf{C}\boldsymbol{\tau}_{\mathbf{n+1}}^{\boldsymbol{\beta}}\Delta\mathbf{t}_{\mathbf{n+1}}^{\boldsymbol{\alpha}} \tag{5-7}$$

where $\mathbf{D_n}$ is the damage index at time step $\mathbf{n}$, $\mathbf{D_{n+1}}$ is the damage index at time step $\mathbf{n} + \mathbf{1}$, and all other variables are as defined previously (Fraser et al., 2011).

### 5.3. Methodology

The geometry for the simplified centrifugal blood pump model shown in **Figure 5-2** was created using computer-aided design as part of the FDA's CPI CFD and Blood Damage project (US Food and Drug Administration). The

experimental setup of the pump (**Figure 5-1**) indicates that the fluid exits the device in the direction opposite the gravitational force. Gravity is included in the numerical calculations to account for these effects. Experimentally, flow through the pump may transition between laminar and turbulent and is time-dependent due to the movement of the rotor. Flow regime transitions are not captured in this study, but the flow is modeled as unsteady for both laminar and turbulent flow conditions.

The flow domain is meshed in ANSYS® ICEM CFD™ (version 14.0) using the robust Octree method and is optimized based on the orthogonal quality of the mesh. An entrance region is included in the system model to ensure the velocity profile at the flow probe does not exhibit entry effects. The resulting grid consists of approximately 2 million cells and 700,000 nodes. Solutions are obtained using ANSYS® Fluent® (version 14.0) with second order upwind spatial discretization and first order temporal discretization.

A sliding mesh approach is used with 200 time steps per rotation and a time step size on the order of $0.1\ \mathrm{msec}$. A maximum of 30 iterations per time step is allowed for the solution to reach the minimum convergence criteria of $10^{-4}$ for all residuals.

Flow field solutions are allowed to develop for at least $1000\ \mathrm{msec}$ (i.e., 50 complete rotations) before data sampling and particle injection are initiated. For the Lagrangian damage estimates, particles are tracked through the flow domain using the Discrete Phase Model available in ANSYS® Fluent®. The use of this

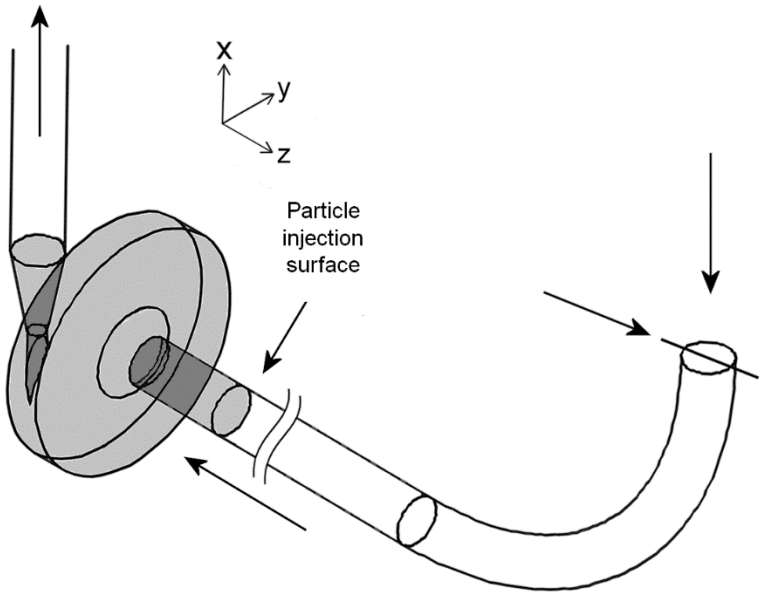


**Figure 5-3: Region of interest for Lagrangian damage index estimates.**

***The gray shading indicates the region in which injected particles are considered "active" and data are collected. The arrows indicate the direction of the flow.***

model accounts for the presence of a discrete second phase in the transport equations (Fluent Inc.®, 2001).

528 massless particles, which do not interact with other particles of the continuous phase, are released simultaneously from the particle injection surface, as indicated in **Figure 5-3**. Once injected, each particle is considered "active" as long as the particle is located within the shaded region of **Figure 5-3**. Any particle outside the specified region is considered "escaped" from the system and is excluded from further damage analysis. Data collection is complete once all particles have exited the shaded region. In the cases with a turbulent flow model, the dispersion of particles due to turbulence is predicted using a stochastic tracking model. By including instantaneous velocity fluctuations in the

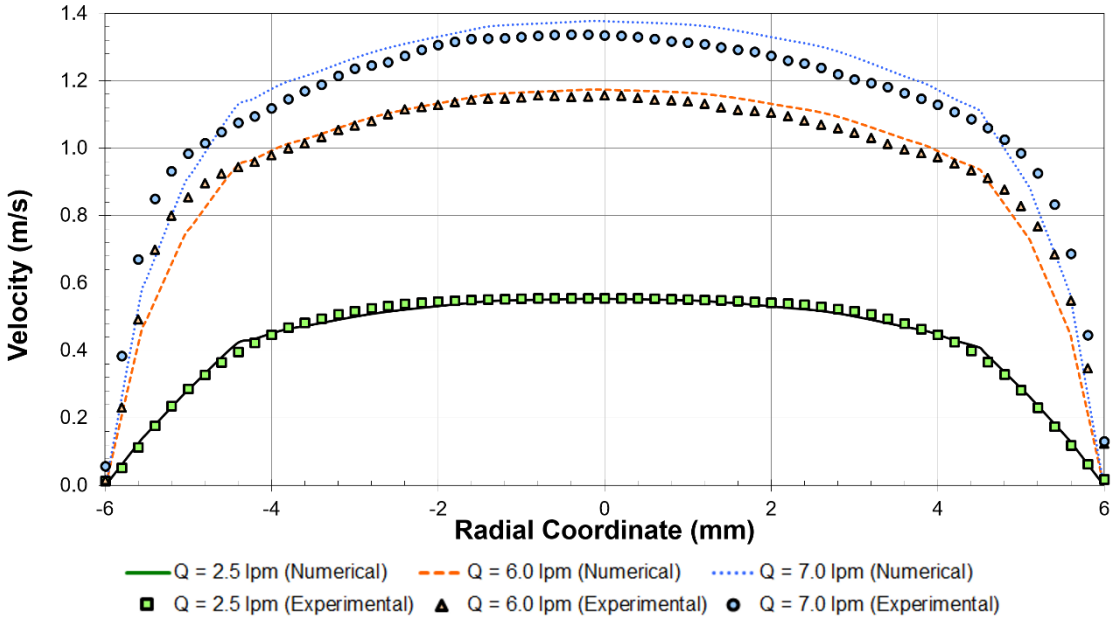


**Figure 5-4: Validation of numerical velocity profile predictions in the FDA blood pump model.**

***Experimental results are mean velocity measurements obtained using PIV. Numerical results are obtained using the SST k-ω model for turbulence.***

particle trajectory predictions, this model effectively accounts for the effects of turbulence on particle dispersion (Fluent Inc.®, 2001).

The FDA has declared intent to release detailed laboratory measurements that can be used to validate the findings of this study. Experimental velocity profiles, obtained using particle image velocimetry at the location labeled "flow probe" in **Figure 5-1**, are currently available for numerical solution validation. It should be noted, however, that the pump geometry, gap widths, and operating conditions are similar to the CentriMag centrifugal pump, which has been studied in depth by Taskin et al. (2010) and Fraser et al. (2011).

In **Figure 5-4**, we compare the mean experimental velocity profiles with the corresponding numerical predictions for velocity obtained using turbulent flow

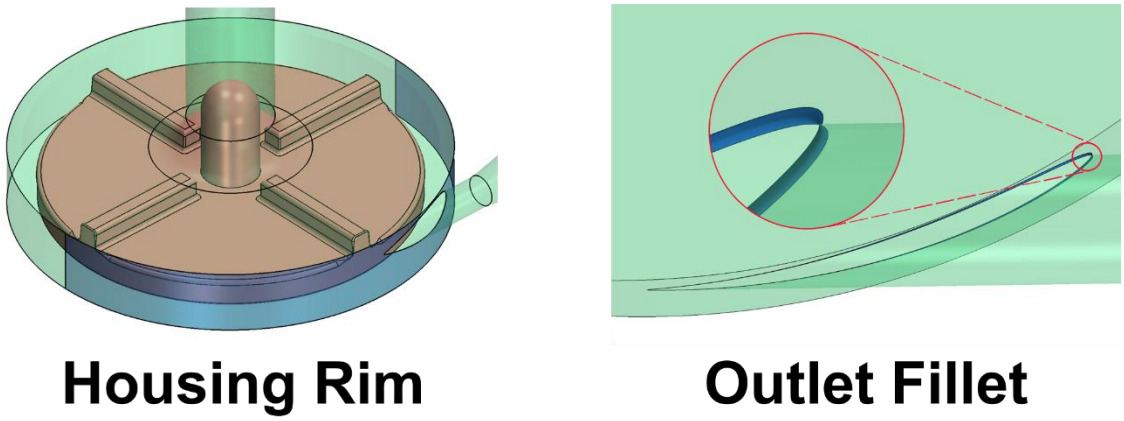


**Figure 5-5: Locations for surface-averaged wall shear stress estimates.**

and Newtonian rheological models. On average, numerical velocity estimates differ from mean experimental values by approximately 10%-15%. Experimental results are for porcine blood at 25°C, 36% hematocrit, and 11.5 g/dL total hemoglobin concentration (US Food and Drug Administration).

Data are sampled every 5 time steps, approximately equal to $0.5\ \mathrm{msec}$. The time- and spatially-averaged pressures at the pump inlet and outlet, along with the average and maximum wall shear stresses over the housing rim and outlet fillet of the pump (**Figure 5-5**) and the volume- averaged instantaneous shear stress in the fluid in the rotor region are collected for each data sampling.

### 5.4. Results and Discussion

**Table 5-1** is a summary of the conditions considered in this study, which include three flow rates, two rotational speeds, and two turbulence intensities. **Cases L1.1** through **L1.6** and **L2** are modelled as both laminar and turbulent. For **Cases L1.1** through **L1.6**, the rheological behavior of the fluid is modelled using the Carreau and Casson models for viscosity, as well as a Newtonian model. For all other cases, the flow is modeled as turbulent and Newtonian.

**Table 5-1: Summary of simulated cases and associated model parameters and operating conditions.**

| Case | $Re_{flow\ probe}$ | Viscosity Model | Hematocrit | Temperature $T\ [=]°C$ | Flow Model | Flow Rate $Q\ [=]\ lpm$ | Rotational Speed $\omega\ [=]\ rpm$ |
|---|---|---|---|---|---|---|---|
| L1.1 | 1565 | Casson | 25% | 23 | Laminar | 2.5 | 2500 |
| L1.2 | 2149 | Casson | 25% | 37 | | | |
| L1.3 | 1197 | Carreau | 36% | 23 | | | |
| L1.4 | 1307 | Newtonian | 36% | 23 | | | |
| L1.5 | 839 | Casson | 55% | 23 | | | |
| L1.6 | 1152 | Casson | 55% | 37 | | | |
| T1.1 | 1565 | Casson | 25% | 23 | Turbulent | 2.5 | 2500 |
| T1.2 | 1307 | Newtonian | 36% | | | | |
| T1.3 | 839 | Casson | 55% | | Laminar | 2.5 | 3500 |
| L2 | 1307 | Newtonian | 36% | 23 | Turbulent | 2.5 | 3500 |
| T2 | 1307 | Newtonian | 36% | 23 | | | |
| T3 | 3138 | Newtonian | 36% | 23 | Turbulent | 6.0 | 2500 |
| T4 | 3661 | Newtonian | 36% | 23 | Turbulent | 7.0 | 3500 |

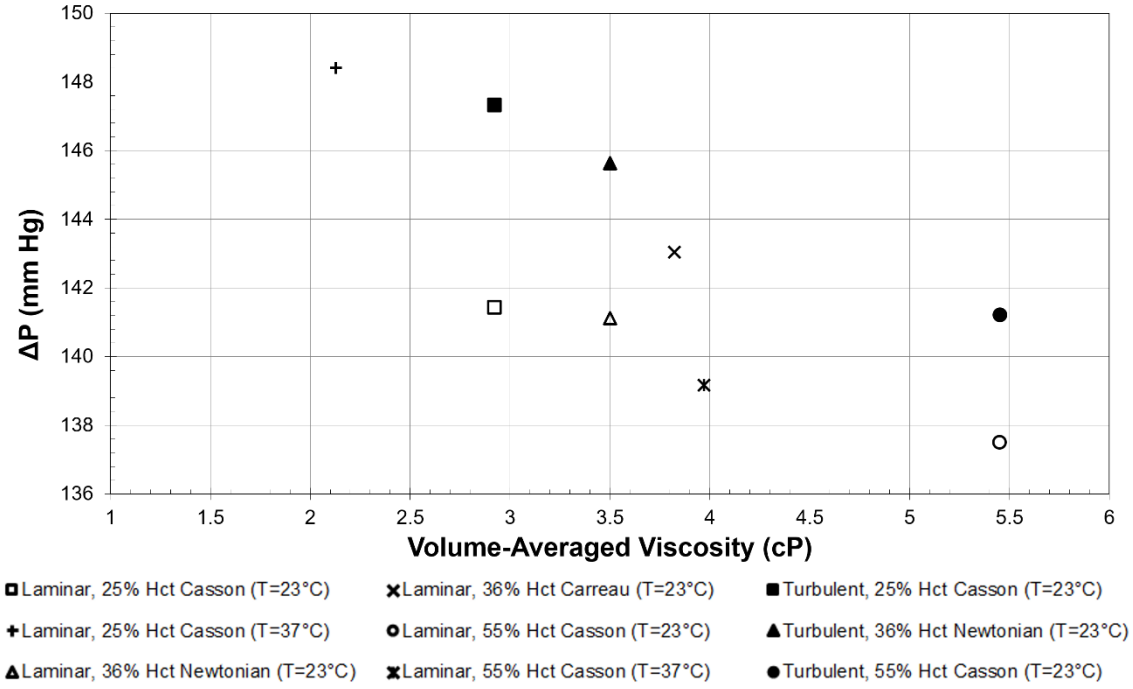


**Figure 5-6: Variance in pressure head predictions with viscosity for non-Newtonian rheological models in laminar and turbulent flow (Cases L1 and T1).**

Results from all cases are averaged over one complete rotation (i.e., the last 200 time steps) of the pump.

### *5.4.1. Effect of Hematocrit*

Laminar flow

At an operating temperature of 23°C, the volume-averaged viscosity of the fluid with 25% hematocrit is calculated to be 16% lower than the viscosity of the fluid with 36% hematocrit (**Cases L1.1** and **L1.4**). The laminar pressure head prediction (**Figure 5-6**) for the lower viscosity fluid is less than 1% higher than that for the fluid with a higher viscosity and, thus, should be considered negligible. On the other hand, changes in wall shear stresses are found to be more appreciable, with the lower viscosity fluid resulting in approximately 12% lower estimates for wall shear stresses along both the housing rim and outlet fillet

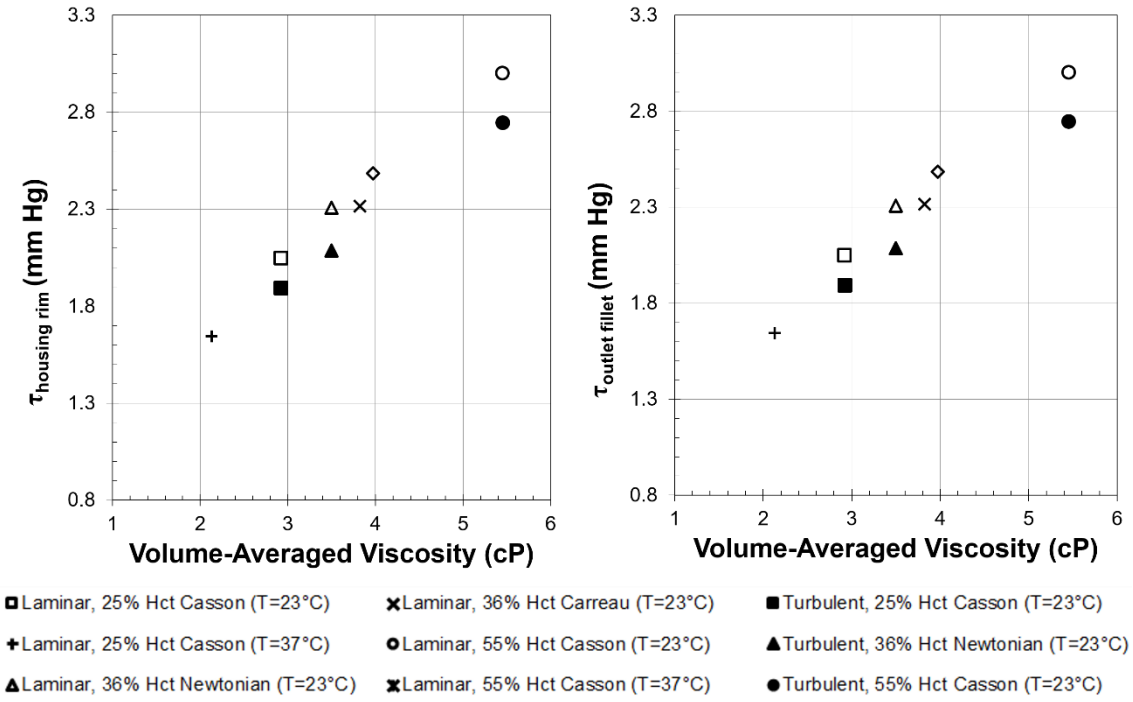


**Figure 5-7: Variance in wall shear stress estimates with viscosity for non-Newtonian rheological models in laminar and turbulent flow (Cases L1 and T1).**

(**Figure 5-7 and 5-8**). The predicted 18% decrease in the instantaneous shear stress estimate for the lower viscosity fluid is also in agreement with empirical results.

The viscosity of the 55% hematocrit fluid at an operating temperature of 23°C is almost 56% higher than the 36% hematocrit fluid at the same temperature (**Cases. L1.4** and **L1.5**). For laminar flow, this substantial increase in viscosity results in less than a 3% decrease in the pressure head estimate. Predictions for the wall shear stresses along the housing rim and outlet fillet (**Figure 5-8)** are approximately 28% and 30% larger for the higher viscosity fluid, while the instantaneous shear stress for the same fluid is almost 45% larger than that predicted for the fluid with 36% hematocrit.

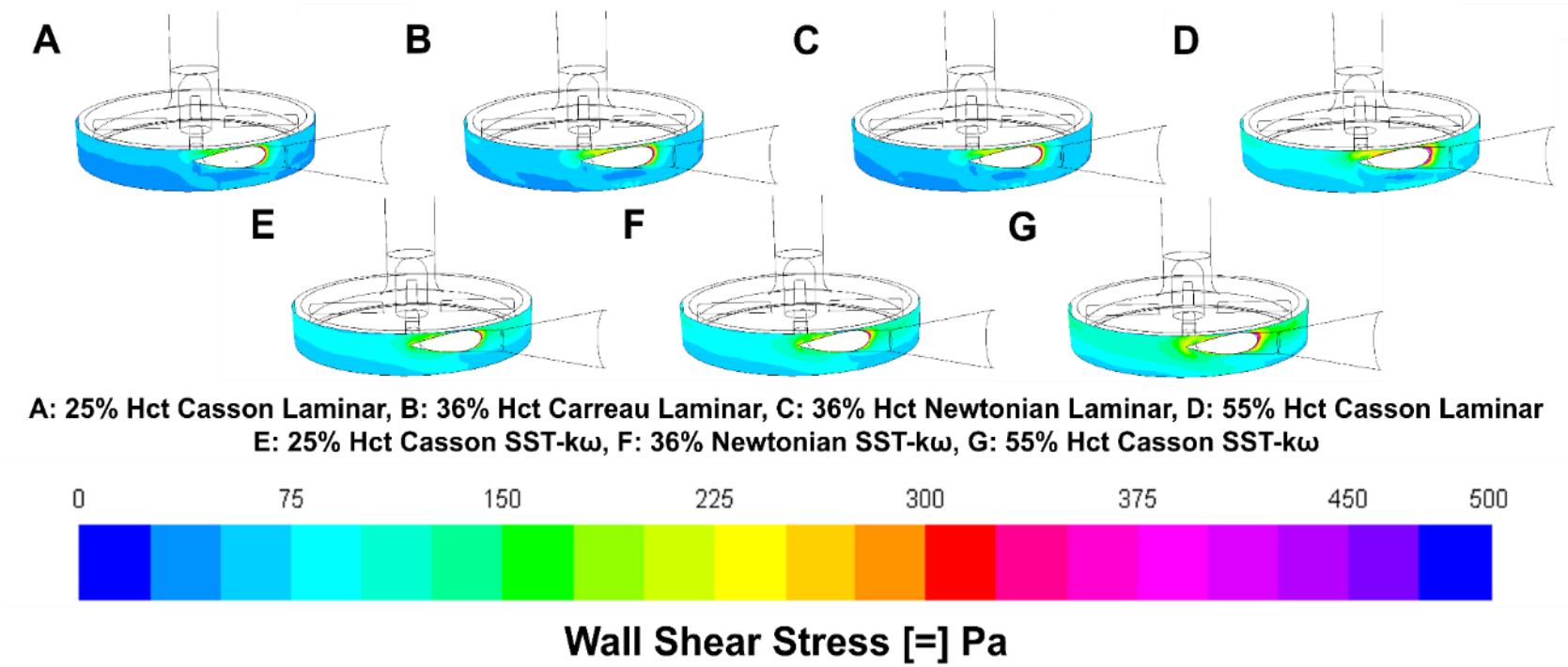


**Figure 5-8: Contours of wall shear stress along housing rim of blood pump.**

Turbulent Flow

As with the laminar flow predictions, the numerical estimate for pressure head for the 25% hematocrit fluid in turbulent flow at an operating temperature of 23°C is found to increase by a negligible 1% from that for 36% hematocrit in the same conditions (**Cases T.1-1** and **T.1-2**). Shear stresses on the housing rim and outlet fillet (**Figure 5-7 and 5-8**) are observed to be 6% and 10% lower in the low viscosity fluid under these same conditions, with the instantaneous shear stress in the same fluid less than 3% smaller than that predicted for the 36% hematocrit fluid.

Comparison of the 55% hematocrit fluid with the fluid with 36% hematocrit (**Cases T.1-1** and **T.1-3)** yields an estimated 3% smaller pressure head (**Figure 5-6**) for the fluid with the larger hematocrit level. The wall shear stress along the housing rim in the larger viscosity fluid is predicted to be almost 23% larger than that for the fluid with 36% hematocrit, while the stress on the outlet fillet is estimated to be 31% larger (**Figure 5-7**). An estimated 5% increase in predictions for the instantaneous shear stress is also observed when the hematocrit content of the fluid is increased from 36% to 55%.

In general, accounting for hematocrit appears to reduce differences in stress predictions and pressure drops between the laminar and turbulent flow models, at high hematocrit. Thus, modeling the effects of both hematocrit and turbulence could result in predictions with minimal differences. One possible explanation for this observation is that turbulence may have a more dominating effect in fluids with low hematocrit (i.e., less viscous fluids) and less of an effect

in more viscous flow. This conclusion is fairly intuitive since turbulence would be dampened in the presence of a higher viscosity fluid. The Reynolds number for that flow would also be lower.

### *5.4.2. Effect of Shear-Thinning Blood Rheology*

The Carreau model for the shear-thinning behavior of the fluid predicts an average viscosity that is slightly more than 10% larger than that for the Newtonian fluid in laminar flow at an operating temperature of 23°C (**Cases L1.3** and **L1.4**). The resulting pressure head prediction (**Figure 5-6**) associated with the shear-thinning fluid is less than 2% higher than that for the Newtonian fluid. Differences in estimates for the wall shear stresses along the housing rim and outlet fillet (**Figures 5-7** and **5-8**) are also small, with a predicted increase of approximately 2% and 1%, respectively. Differences in the instantaneous shear stress between the two fluids are even more insignificant, as the stress in the non-Newtonian fluid is estimated to be less than 0.1% larger than that in the Newtonian fluid.

The small variance in pressure head predictions with large changes in viscosity, coupled with the larger variances in wall shear stress estimates, can be explained by examining the governing equations of fluid flow. Pressures in the flow domain are described by the Poisson equation, which does not have a direct dependence on viscosity. On the other hand, shear stress, as described by Newton's law, scales with viscosity. Thus, pressure head predictions would not be expected to change dramatically, while shear stress estimates would be relatively sensitive to viscosity changes.

### *5.4.3. Effect of Temperature*

When the operating temperature of the device is increased from 23°C to 37°C, the viscosity of the fluid with 25% hematocrit (**Cases L1.1** and **L1.2**) decreases by approximately 27%. The pressure head prediction (**Figure 5-6**) associated with the lower viscosity fluid is observed to increase by less than 5%. Although this result may not agree with practical observations, since pressure at a pump outlet would decrease with blood viscosity due to vascular resistance, the observed increase is within the estimated error range of the numerical calculations and cannot be concluded to be significant (Ahn et al., 2011). The higher operating temperature does, however, result in more appreciable changes in the housing rim and outlet fillet wall shear stress predictions (**Figure 5-8**), which are estimated to decrease by approximately 16% and 20%, respectively. Similarly, the instantaneous shear stress in the lower viscosity fluid is almost 26% lower than that in the higher viscosity fluid.

The fluid with 55% hematocrit (**Cases L1.5** and **L1.6**) also has a 27% decrease in viscosity when the operating temperature is increased from 23°C to 37°C. The corresponding estimate for pressure head (**Figure 5-6**) in the lower viscosity fluid is approximately 7% lower than that for the higher viscosity fluid. Housing rim and outlet fillet wall shear stresses (**Figure 5-8**) are estimated to be 15% and 17% lower at the higher operating temperature, while the instantaneous shear stress in the lower viscosity fluid is predicted to be almost 25% lower.

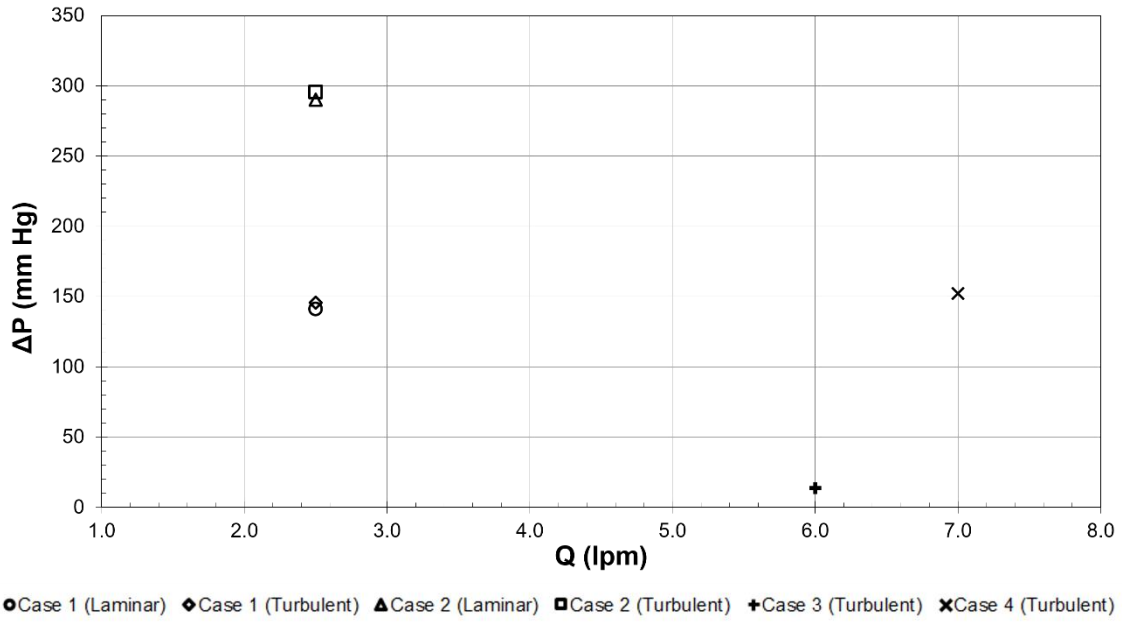


**Figure 5-9: Variance in pressure head predictions with flow rate for laminar and SST k-ω models (Cases L1, L2, T1, T2, T3, and T4).**

These findings suggest observations for blood damage from the device itself ex vivo will be greater than when implanted.

As with shear-thinning behavior, temperature is observed to have a more substantial effect on wall shear stresses and instantaneous fluid stresses than on pressure head predictions. A similar argument regarding Newton's law of viscosity also provides a useful explanation for these observations.

### *5.4.4. Effect of Turbulence*

Modeling the Newtonian fluid with 36% hematocrit as turbulent at a flowrate of 2.5 lpm, with a rotor speed of 2500 rpm and an operating temperature of 23°C, results in approximately 3% increase in pressure head (**Figure 5-9**) when compared to that obtained for laminar flow in the same conditions (**Cases L1.4** and **T1.2**). Wall shear stress estimates for the housing rim also increase by slightly more than 6%, although outlet fillet shear stress predictions decrease by

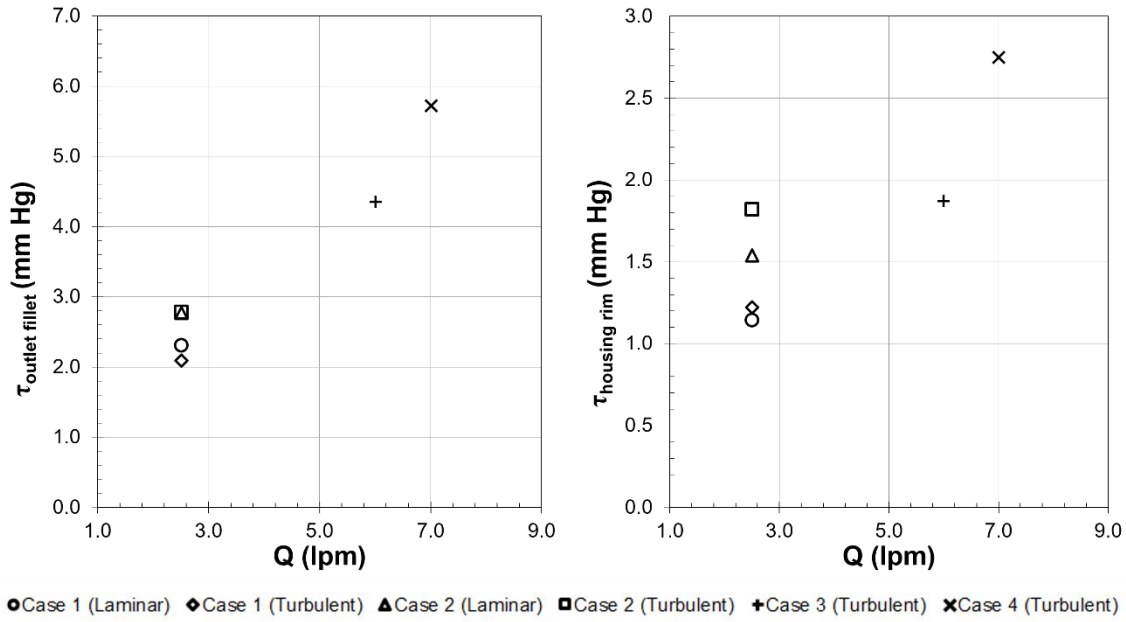


**Figure 5-10: Variance in wall shear stress estimates with flow rate for laminar and SST k-ω models (Cases L1, L2, T1, T2, T3, and T4).**

almost 10% (**Figure 5-7** and **5-10**). Furthermore, the instantaneous shear stress of the fluid is estimated to be 40% lower in turbulent flow than in laminar, when the flow rate is the same.

The same comparison between laminar and turbulence models for the 36% hematocrit Newtonian fluid at a flow rate of 2.5 lpm, a rotor speed of 2500 rpm, and an operating temperature of 23°C yields similar results. The pressure head prediction (**Figure 5-9**) for the turbulent flow is approximately 2% higher for the fluid in turbulent flow, but housing rim and outlet shear stress estimates (**Figure 5-7 and 5-10**) show a larger range of variance, with almost 18% and less than 1% increase, respectively, associated with the use of a model for turbulence. Instantaneous shear stress predictions, however, are observed to be more than 40% larger for the laminar model.

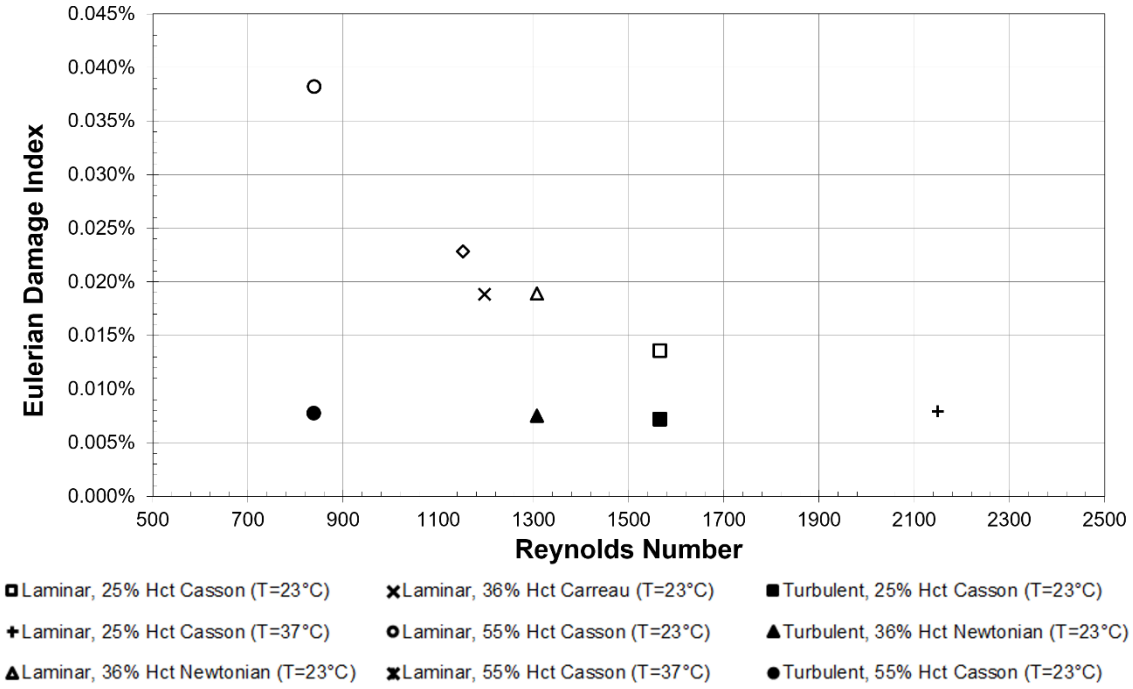


**Figure 5-11: Variance in Eulerian damage with Reynolds number for non-Newtonian rheological models in laminar and turbulent flow (Cases L1 and T1).**

The presence of turbulence results in relatively little variance in pressure head predictions between the laminar and turbulent flow models. Because the use of models for turbulence is associated with increased computational cost, this observation would seemingly indicate that the flow could be modeled as laminar. Pressure solutions obtained using the laminar model, however, are often numerically unstable and take more iterations to converge than those predicted using the SST *k*-ω model.

### *5.4.5. Damage Index Estimates*

A remarkable amount of effort has been placed on the development of hemolysis models (Taskin et al., 2010; Arora, Behr, and Pasquali, 2006; Garon and Farinas, 2004). Several stress- and strain-based models for hemolysis have been proposed as an alternative to the Giersiepen power law in **Equation 5-4**,

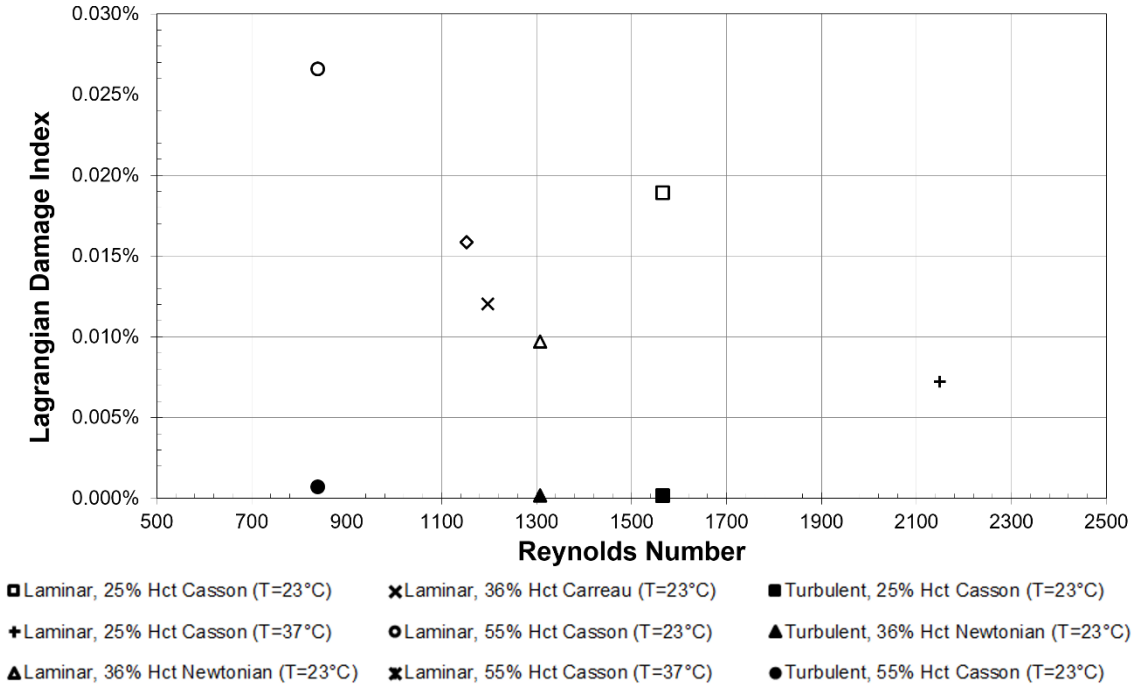


**Figure 5-12: Variance in Lagrangian damage with Reynolds number for non-Newtonian rheological models in laminar and turbulent flow (Cases L1 and T1).**

which has largely been shown to overestimate true hemolysis levels (Fraser et al., 2011). Nonetheless, the power law model remains one of the more popular approaches for damage estimates.

Blood damage indices differ by as much as 200% between the Eulerian (**Figure 5-11**) and Lagrangian (**Figure 5-12**) formulations. However, it is seen that the damage index decreases with increasing temperature while it increases with the hematocrit. This observation can be interpreted when one considers the fluid viscosity changes with hematocrit and temperature. In general, when the viscosity is higher, the stresses are higher, and the power law model predicts higher damage index in both the Lagrangian and the Eulerian frameworks. In addition, the Newtonian model for blood results in lower hemolysis estimates than

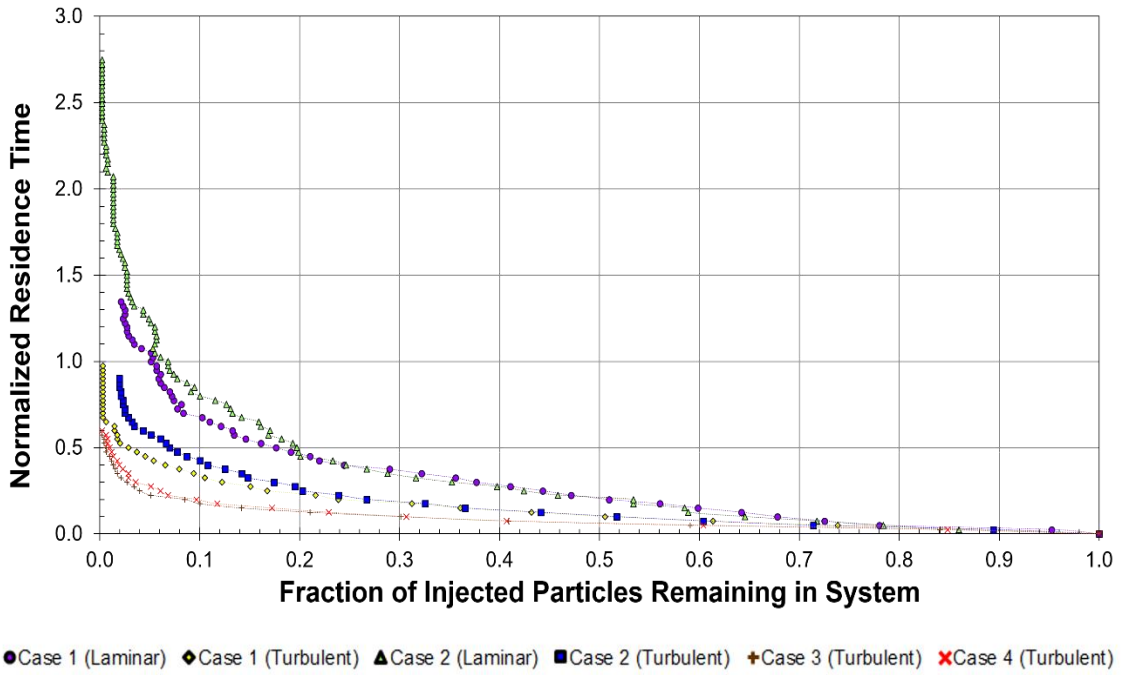


**Figure 5-13: Residence times for laminar and turbulent flow models for laminar and SST k-ω models (Cases L1, L2, T1, T2, T3, and T4).**

the Carreau rheological model. The distributions of the cell residence times in the pump (**Figure 5-13**) for laminar flow models indicate that laminar models result in residence times that are short. Turbulence models predict residence times that are about half the time predicted with laminar models under the same conditions. The variance and lack of precision in damage predictions observed in this study has also been reported by Taskin et al. (2012) for a similar blood pump model and is generally attributed to error related to the power-law model in **Equation 5-4**. The observed imprecision associated with hemolysis estimates indicates a serious need for development and improvement of damage index estimation approaches and may in itself suggest the need to consider the effects of turbulence. In general, turbulent flow is thought to result in greater damage to cells. However, the Eulerian power law index for laminar flow simulations was

greater than that for turbulent flow simulations (see **Figure 5-11**; **L1.1** compared to **T1.1** and **L.2** compared to **T.2**).

### 5.5. Summary and Conclusions

The shear-thinning behavior of blood is shown to have a minor effect on key comparison metrics when compared to the effects of hematocrit. Changes in viscosity due to hematocrit levels result in negligible changes in pressure head predictions, although more appreciable differences are observed in wall shear stress estimates. The amplified effect of viscosity due to changes in hematocrit is consistent with the governing equations for the system considered. These observations seemingly indicate that hematocrit content may be an important property of blood that should be included in numerical models. Shear-thinning properties, however, may be neglected without significant loss in accuracy.

The effect of temperature on numerical estimates for various hematocrit contents does not appear to be significant on predicted pressure heads, despite the large associated changes in viscosity. On the other hand, changes in temperature do appear to have an appreciable effect on estimated wall stresses, most notably those for the instantaneous shear stress in the fluid. While temperature may have some impact on numerical predictions, hematocrit is observed to result in even more substantial differences in estimates. Nonetheless, the use of a modified-Casson model, such as that proposed by Apostolidis and Beris (2014) and used in this study, since it can capture the effects of both hematocrit and temperature is highly recommended.

Numerical estimates for pressure head are observed to have negligible variance between laminar and turbulent flow models. While an increased computational cost is associated with the use of a turbulence model, the use of a laminar model is noted to result in numerical instabilities. As a consequence, the use of a turbulence model to represent flow within the blood pump is recommended, even in low and transitional Reynolds-number flow regimes.

Predictions for pressure drop and shear stress at the wall obtained when accounting for hematocrit and the presence of turbulence are generally lower than those obtained for either when modeled separately. This result may be explained by a shift in the dominating physical phenomena associated with the low and high viscosity fluids. For low hematocrit levels, turbulence may have a more pronounced effect on the flow field than is observed for fluids with high hematocrit content. The effects of turbulence, however, would then be expected to be dampened in a higher viscosity fluid, which is observed in numerical predictions for the key comparison metrics considered. Thus, by including both hematocrit and turbulence in CFD simulations, the overall error in comparison metric estimates could be reduced.

As is reported by Taskin et al. (2012), and confirmed in this study, hemolysis estimates using the power-law model and Eulerian and Lagrangian formulations do not yield the same predictions for hemolysis, so one would need to take experimental measurements to determine which approach is more accurate. The lack of precision associated with the CFD blood damage index predictions can be attributed to the use of the power-law model, which was

developed for a Couette flow system under constant shear stress and is, thus, arguably unsuitable for systems such as that considered in this study. Furthermore, due to the lack of consistency and reliability associated with these methods of hemolysis estimation, CFD would benefit greatly from improved damage index formulations and approaches.

## 5.6. Nomenclature

Roman Characters

| | |
|---|---|
| $\mathbf{C}$ | Damage index constant ($\mathbf{C = 1.800 \times 10^{-6}}$) |
| $\mathbf{D}$ | Damage index |
| $\mathbf{D_{n,}}$, $\mathbf{D_{n+1}}$ | Damage index at time step $\mathbf{n}$, $\mathbf{n+1}$ |
| $\frac{\mathbf{\Delta Hb}}{\mathbf{Hb}}$ | Ratio of plasma-free hemoglobin to total hemoglobin |
| $\mathbf{n}$ | Carreau model constant ($\mathbf{n = 0.3568}$) |
| $\mathbf{n_p}$ | Plasma viscosity |
| $\mathbf{t}$ | Time |
| $\mathbf{T}$ | Temperature |
| $\mathbf{T_o}$ | Reference temperature |
| $\mathbf{Q}$ | Volumetric flow rate |
| $\mathbf{V}$ | Computational volume |

Greek Characters

| | |
|---|---|
| $\boldsymbol{\alpha, \beta}$ | Damage index constants ($\boldsymbol{\alpha = 0.7650,\ \beta = 1.9910}$.) |
| $\dot{\boldsymbol{\gamma}}$ | Shear rate |
| $\boldsymbol{\lambda}$ | Carreau model constant ($\boldsymbol{\lambda = 3.313\ s}$,) |
| $\boldsymbol{\mu}$ | Fluid viscosity |
| $\boldsymbol{\mu_0}$ | Carreau model lower viscosity limit |
| $\boldsymbol{\mu_\infty}$ | Carreau model upper viscosity limt |
| $\boldsymbol{\rho}$ | Fluid density |
| $\boldsymbol{\sigma}$ | Rate of hemolysis production per unit time |

| | |
|---|---|
| $\boldsymbol{\tau}$ | Shear stress |
| $\boldsymbol{\tau_y}$ | Yield stress |

## 5.7. References


Ahn, Chi Bum, Kuk Hui Son, Jung Joo Lee, Jaesoon Choi, Seung Joon Song, Jae Seung Jung, Sung Ho Lee, Ho Sung Son, and Kyung Sun. "The effect of fluid viscosity on the hemodynamic energy changes during operation of the pulsatile ventricular assist device." *Artificial organs* 35, no. 11 (2011): 1123-1126.

ANSYS® Fluent® Theory Guide (2001).

Apostolidis, Alex J., and Antony N. Beris. "Modeling of the blood rheology in steady-state shear flows." *Journal of Rheology (1978-present)* 58, no. 3 (2014): 607-633.

Behbahani, M., M. Behr, M. Hormes, U. Steinseifer, D. Arora, O. Coronado, and M. Pasquali. "A review of computational fluid dynamics analysis of blood pumps." *European Journal of Applied Mathematics* 20, no. 04 (2009): 363-397.
Blackshear Jr, Perry L., Frank D. Dorman, and Joseph H. Steinbach. "Some mechanical effects that influence hemolysis." *ASAIO Journal* 11, no. 1 (1965): 112-117.

Carpenter, Brian A., Christian J. Gonzalez, Staci L. Jessen, Erica J. Moore, Amber N. Thrapp, Brad R. Weeks, and Fred J. Clubb. "A brief review of ventricular assist devices and a recommended protocol for pathology evaluations." *Cardiovascular Pathology* 22, no. 5 (2013): 408-415.

Coglianese, Erin E., Muhammad M. Qureshi, Ramachandran S. Vasan, Thomas J. Wang, and Lynn L. Moore. "Usefulness of the blood hematocrit level to predict development of heart failure in a community." *The American journal of cardiology* 109, no. 2 (2012): 241-245.

Ding, Jun, Shuqiong Niu, Zengsheng Chen, Tao Zhang, Bartley P. Griffith, and Zhongjun J. Wu. "Shear-Induced Hemolysis: Species Differences." *Artificial organs* (2015).

Fournier, Ronald L. *Basic transport phenomena in biomedical engineering*. CRC Press, 2007.

Fraser, Katharine H., M. Ertan Taskin, Bartley P. Griffith, and Zhongjun J. Wu. "The use of computational fluid dynamics in the development of ventricular assist devices." *Medical engineering & physics* 33, no. 3 (2011): 263-280.

Fujino, Takeo, Koichiro Kinugawa, Masaru Hatano, Teruhiko Imamura, Hironori Muraoka, Shun Minatsuki, Toshiro Inaba et al. "Low Blood Pressure, Low Serum Cholesterol and Anemia Predict Early Necessity of Ventricular Assist Device Implantation in Patients With Advanced Heart Failure at the Time of Referral From Non-Ventricular Assist Device Institutes." *Circulation Journal* 78, no. 12 (2014): 2882-2889.

Garon, André, and Marie-Isabelle Farinas. "Fast Three-dimensional Numerical Hemolysis Approximation." *Artificial Organs* 28, no. 11 (2004): 1016-1025.

Giersiepen, M., L. J. Wurzinger, R. Opitz, and H. Reul. "Estimation of shear stress-related blood damage in heart valve prostheses--in vitro comparison of 25 aortic valves." *The International journal of artificial organs* 13, no. 5 (1990): 300-306.

Goubergrits, Leonid, and Klaus Affeld. "Numerical estimation of blood damage in artificial organs." *Artificial organs* 28, no. 5 (2004): 499-507.

Hess, Michael L., Richard H. Cooke, Amit Varma, and Keyur B. Shah. "Right ventricular dysfunction: lessons learned from mechanical circulatory assist devices." *The American journal of the medical sciences* 347, no. 1 (2014): 80-83.

Jiang, C. (2014, October 15). *Fluent - 3D Bifurcating Artery.* (C. University, Ed.) Retrieved 03 30, 2015, from Cornell University Confluence: confluence.cornell.edu.

Kameneva, Marina V., Greg W. Burgreen, Kunisha Kono, Brandon Repko, James F. Antaki, and Mitsuo Umezu. "Effects of turbulent stresses upon mechanical hemolysis: experimental and computational analysis." *ASAIO journal* 50, no. 5 (2004): 418-423.

Malinauskas, Richard A., Anindita Saha, and Murray I. Sheldon. "Working With the Food and Drug Administration's Center for Devices to Advance Regulatory Science and Medical Device Innovation." *Artificial organs* 39, no. 4 (2015): 293-299.

Menter, Florian R. "Two-equation eddy-viscosity turbulence models for engineering applications." *AIAA journal* 32, no. 8 (1994): 1598-1605.

Ozturk, Mesude, Edgar A. O'Rear, and Dimitrios V. Papavassiliou. "Hemolysis Related to Turbulent Eddy Size Distributions Using Comparisons of Experiments to Computations." *Artificial organs* (2015).

Song, Xinwei, Houston G. Wood, Steven W. Day, and Don B. Olsen. "Studies of turbulence models in a computational fluid dynamics model of a blood pump."*Artificial organs* 27, no. 10 (2003): 935-937.

Stewart, Sandy FC, Eric G. Paterson, Greg W. Burgreen, Prasanna Hariharan, Matthew Giarra, Varun Reddy, Steven W. Day et al. "Assessment of CFD performance in simulations of an idealized medical device: results of FDA's first computational interlaboratory study." *Cardiovascular Engineering and Technology* 3, no. 2 (2012): 139-160.

Su, Boyang, Leok Poh Chua, and Xikun Wang. "Validation of an axial flow blood pump: computational fluid dynamics results using particle image velocimetry." *Artificial organs* 36, no. 4 (2012): 359-367.

Taskin, M. Ertan, Katharine H. Fraser, Tao Zhang, Barry Gellman, Andi Fleischli, Kurt A. Dasse, Bartley P. Griffith, and Zhongjun J. Wu. "Computational characterization of flow and hemolytic performance of the UltraMag blood pump for circulatory support." *Artificial organs* 34, no. 12 (2010): 1099-1113.

Taskin, M. Ertan, Katharine H. Fraser, Tao Zhang, Changfu Wu, Bartley P. Griffith, and Zhongjun J. Wu. "Evaluation of Eulerian and Lagrangian models for hemolysis estimation." *ASAIO journal* 58, no. 4 (2012): 363-372.

Thunberg, Christopher A., Brantley Dollar Gaitan, Francisco A. Arabia, Daniel J. Cole, and Alina M. Grigore. "Ventricular assist devices today and tomorrow."*Journal of cardiothoracic and vascular anesthesia* 24, no. 4 (2010): 656-680.

US Food and Drug Administration. Computational fluid dynamics: an FDA Critical Path Initiative project. Available at: https://fdacfd.nci.nih.gov.

Wilson, Sean R., Michael M. Givertz, Garrick C. Stewart, and Gilbert H. Mudge. "Ventricular assist devices: the challenges of outpatient management." *Journal of the American College of Cardiology* 54, no. 18 (2009): 1647-1659.

White, Frank M., and Isla Corfield. *Viscous fluid flow*. Vol. 3. New York: McGraw-Hill, 2006.

Zhang, Jiafeng, Pei Zhang, Katharine H. Fraser, Bartley P. Griffith, and Zhongjun J. Wu. "Comparison and experimental validation of fluid dynamic numerical models for a clinical ventricular assist device." *Artificial organs* 37, no. 4 (2013): 380-389.

# Chapter 6: Summary and Recommendations

Computational fluid dynamics is used to model micro-channels with rough, 3-dimensional, superhydrophobic walls using free-shear and no-slip boundary conditions (**Chapter 2**) and resulted in the conclusions:

- The results of which show the hydraulic diameter is a useful indicator of achievable drag reduction over hydrophobicity-inducing roughness.
- Further investigation into the significance of the dimensionless hydraulic diameter on drag reduction for all Reynolds numbers in the laminar flow regime. Such a study could result in a definitive critical value above which drag reduction may be achieved, and could lead to a set of criteria for determining the behavior of fluid flow over SHSs.

An investigation into the effects of roughness of varying shape on drag reduction for flow over these surfaces (**Chapter 3**) indicated that:

- Ridges and circular posts result in the great drag reduction in laminar flow.
- The consideration of roughness elements in shapes other than ridges, circular posts, and square posts could offer insight into the mechanism of drag reduction over superhydrophobic surfaces.
- The validity of modeling the meniscus formed at the air-water interface as flat, though widely utilized, should also be challenged by utilizing

multi-phase models in which the behavior of the air between the micro-roughness elements is also simulated.

Drag reduction is also shown to be achievable in non-Newtonian flow over these surfaces (**Chapter 3**):

- The shear-thinning fluid model achieve the largest drag reduction compared to the Newtonian and shear-thickening fluids.
- A study exploring a wide range of viscosities and viscosity models would allow these surfaces to be developed for use in a wider range of applications and would be beneficial in the development of an optimal superhydrophobic surface.

The results discussed in **Chapters 2** and **3** were used to develop a model to predict slip velocity for flow over these surfaces (**Chapter 4**):

- This model was expanded to predict the slip velocity in non-Newtonian fluids using only a ratio of viscosities.
- The proposed model indicates that an analytical solution for the slip velocity may exist.
- A more rigorous mathematical analysis using similarity theory could lead to the development of an equation to predict drag reduction in a wider range of flow than was considered in this study.

Flow through a centrifugal blood pump was modeled and the effects of hematocrit, non-Newtonian rheological behavior, temperature, and turbulence were quantified and presented (**Chapter 5**) with the following conclusions.:

- The use of computational fluid dynamics would benefit significantly from the development of a more reliable blood damage model.
- A study exploring a wide range of viscosities and viscosity models would allow these surfaces to be developed for use in a wider range of applications and would be beneficial
- The results of this study should be validated with experimental data and used to formulate a new approach to estimating hemolysis in blood-contacting devices.